

Measurement of the response of the central ATLAS calorimeter to pions with energy in the range 3-250 GeV. Calibration of the hadronic calorimeter photomultipliers using a laser system.

R. Febbraro

▶ **To cite this version:**

R. Febbraro. Measurement of the response of the central ATLAS calorimeter to pions with energy in the range 3-250 GeV. Calibration of the hadronic calorimeter photomultipliers using a laser system.. High Energy Physics - Experiment [hep-ex]. Université Blaise Pascal - Clermont-Ferrand II, 2009. English. NNT : . tel-00461206

HAL Id: tel-00461206
https://theses.hal.science/tel-00461206

Submitted on 3 Mar 2010

HAL is a multi-disciplinary open access archive for the deposit and dissemination of scientific research documents, whether they are published or not. The documents may come from teaching and research institutions in France or abroad, or from public or private research centers.

L'archive ouverte pluridisciplinaire **HAL**, est destinée au dépôt et à la diffusion de documents scientifiques de niveau recherche, publiés ou non, émanant des établissements d'enseignement et de recherche français ou étrangers, des laboratoires publics ou privés.

NUMERO D'ORDRE: D.U. 1693
EDSF: 628

UNIVERSITE BLAISE PASCAL
(U.F.R. SCIENCES ET TECHNOLOGIES)

ECOLE DOCTORALE DES SCIENCES FONDAMENTALES

THESE

PRESENTEE POUR OBTENIR LE GRADE DE

DOCTEUR D'UNIVERSITE
(SPECIALITE: PHYSIQUE DES PARTICULES)

PAR

Renato FEBBRARO
D.E.A.

Measurement of the response of the central ATLAS calorimeter to pions with energy in the range 3-250 GeV. Calibration of the hadronic calorimeter photomultipliers using a laser system.

Soutenue plubliquement le 10 décembre 2009, devant la commission d'examen.

President:	M.	P. Henrard
Examinateurs:	M.	C. Santoni
	M.	D. Pallin
	M.	S. Nemecek
Rapporteurs:	M.	P. Fassnacht
	Mme	I.Vichou

Contents

Contents **2**

1 Theoretical overview **9**
1.1 The Standard Model . . . 9
1.1.1 Matter particles and gauge bosons . . . 9
1.1.2 Gauge symmetries . . . 12
1.2 Electroweak Theory . . . 13
1.2.1 Electroweak symmetry breaking . . . 14
1.2.2 Higgs Boson searches . . . 14
1.2.2.1 Higgs boson production modes . . . 15
1.2.2.2 Higgs decays modes . . . 17
1.3 Beyond the Standard Model . . . 19
1.3.1 Limitations of the Standard Model . . . 20

2 The LHC and the ATLAS detector **22**
2.1 The LHC project . . . 22
2.2 Definitions and conventions . . . 23
2.3 Physics Requirements . . . 25
2.4 The magnetic system . . . 26
2.5 The inner detector . . . 27
2.6 Calorimeter System . . . 29
2.7 The muon spectrometer . . . 31

3 ATLAS hadronic calorimeter **33**
3.1 Tilecal calorimeter . . . 33
3.2 Signal production . . . 35
3.3 Signal reconstruction . . . 35
3.3.1 HVmicro card . . . 37
3.3.2 HVopto card . . . 37
3.3.3 Divider card . . . 37
3.3.4 “3 in 1” card . . . 37
3.3.5 Digitizer card . . . 37
3.3.6 Interface card . . . 38
3.3.7 Adder card . . . 39
3.4 Filter algorithms . . . 39

3.4.1 Flat Filter . . . 39
3.4.2 Fit Filter . . . 39
3.4.3 Optimal filter . . . 40
3.5 Tilecal calibration systems . . . 40
3.5.1 Charge injection system . . . 40
3.5.2 Cesium calibration . . . 41
3.5.3 LASER Calibration . . . 42
3.5.4 Cells electromagnetic scale calibration . . . 44

4 The Tilecal LASER calibration system 46
4.1 The LASER setup . . . 46
4.1.1 The LASER box . . . 47
4.1.2 The distribution system . . . 49
4.2 LASER electronics . . . 51
4.3 LASER operating modes . . . 51
4.3.1 System intercalibration mode . . . 52
4.3.1.1 Pedestals . . . 52
4.3.1.2 Photodiodes response to an alpha source . . . 53
4.3.1.3 Diodes electronics linearity . . . 53
4.3.2 LASER mode . . . 53
4.4 LASER system commissioning . . . 54
4.4.1 Pedestals . . . 54
4.4.2 Photodiodes stability (response to the alpha source) . . . 54
4.4.3 Linearity of the photodiodes electronics . . . 58
4.5 Tilecal calibration and monitoring with the LASER system . . . 59
4.5.1 Monitoring . . . 60
4.5.2 Calibration . . . 60
4.5.2.1 Stability . . . 61
4.5.2.2 Linearity . . . 66
4.6 Conclusions . . . 74

5 ATLAS calorimeters response to high energy pions 77
5.1 H8 beam line . . . 77
5.1.1 Primary beam coming from the SPS accelerator . . . 77
5.1.2 Secondary high energy beam . . . 78
5.1.3 Tertiary high energy beam . . . 78
5.2 The ATLAS detector at 2004 combined test beam . . . 78
5.2.1 H8 beam line instrumentation . . . 78
5.2.2 The inner detector . . . 83
5.2.3 Calorimeters . . . 83
5.2.3.1 The electromagnetic calorimeter LAr . . . 83
5.2.3.2 Hadronic calorimeter Tilecal . . . 86
5.2.4 Muon spectrometer . . . 87
5.3 Rejection cuts . . . 87
5.3.1 Muon rejection . . . 88
5.3.2 Electron rejection . . . 88

5.3.3 Interactions upstream the calorimeters 89
5.3.4 Beam chambers cuts 90
5.4 Measure of the response and the resolution of the calorimeters 91
5.4.1 Measurement of the beam energy 92
5.4.2 Combined fractional response 92
5.4.3 Combined fractional resolution 96
5.4.4 Comparison between data and Monte Carlo 98

6 ATLAS calorimeters response to very low energy pions 103
6.1 The experimental set-up 103
6.2 The selection criteria 104
6.3 Pion sample contamination study 109
6.3.1 Electron contamination 109
6.3.2 Contamination due to pion decay 111
6.3.3 Contamination by halo muon. 113
6.4 Pion reconstruction and their response in the calorimeters . . . 114
6.4.1 Calorimeters energy scale 114
6.4.2 Electronic noise and pedestal uncertainty 115
6.4.3 Measurement of the beam energy 116
6.4.4 Pion reconstructed energy 116
6.4.5 Measurement of the energy response ratio and of the fractional resolution 119
6.4.6 Montecarlo comparison 121

Bibliography 135

Introduction en français

ATLAS est l'une des quatre expériences installées au CERN, dans le cadre du projet LHC (Large Hadron Collider). Le LHC fournira deux faisceaux de protons, entrant en collision au centre du détecteur ATLAS avec une énergie de 14 TeV dans le centre de masse. ATLAS est une expérience polyvalente se fixant comme objectif principal d'étudier la physique à l'échelle du TeV. À une telle échelle d'énergie, des arguments théoriques et expérimentaux indiquent que le potentiel de découverte de nouvelle physique est élevé. On pense notamment pouvoir mettre en évidence le champ scalaire de Higgs par la production directe de son boson associé (boson de Higgs). En outre, la haute luminosité disponible devrait permettre d'augmenter la précision sur la mesure des paramètres du modèle standard. Enfin la recherche de nouvelle physique au delà du modèle standard, comme par exemple la supersymétrie, constitue une importante partie du programme de physique de l'expérience ATLAS. C'est dans le contexte du calorimètre hadronique de l'expérience ATLAS que cette thèse a été effectuée. Le travail était basé sur deux axes principaux:

- la calibration des photomultiplicateurs (PM) du calorimètre hadronique d'ATLAS avec un système laser,
- l'étude en faisceau test de la réponse en énergie des calorimètres d'ATLAS à des pions chargés d'énergie comprise entre 9 et 250 GeV.

Le calorimètre à tuiles est un sandwich de plaques de fer et de tuiles scintillantes. La particule arrivant dans le calorimètre se désintègre en créant une gerbe de particules de plus basses énergies. Les particules chargées font scintiller les tuiles, et la lumière ainsi créée est transmise via des fibres optiques à des photo-multiplicateurs (PM). Les charges ainsi collectées sont numérisées puis transmises au système d'acquisition d'ATLAS. Les informations de chaque cellule du calorimètre sont alors mises en commun afin de remonter à l'énergie de la particule ayant initié la gerbe.

Dans ce contexte, il est nécessaire d'avoir une très bonne résolution en énergie pour pouvoir faire des analyses de physique précises. En d'autres termes, la différence entre l'énergie reconstruite et l'énergie réelle de la particule doit être la plus petite possible. C'est le travail de la calibration. Le calorimètre à tuiles est un système complexe, et son bon fonctionnement implique le suivi et le contrôle d'un grand nombre de paramètres (bruits, gains des PM,...), ces paramètres pouvant dépendre du temps, de la température. La connaissance de ces informations est critique pour ATLAS. En conséquence, de quoi tous

ces paramètres doivent être mesurés précisément et intégrés dans le code de reconstruction d'ATLAS.

Le LASER est un des systèmes de calibration du calorimètre à tuiles. Il fournit, avec deux autres systèmes (Césium et injection de charges), un étalonnage complet de la chaîne d'acquisition.

La lumière LASER est envoyée directement dans les PM par des fibres optiques. Comme l'intensité de la lumière envoyée est connue avec précision, il est possible d'en déduire le gain du PM en reconstruisant le signal obtenu. Le signal issu du PM est reconstruit de la même façon que le signal de physique. Le système laser, réalisé au LPC, permet d'effectuer des tests de stabilité et de linéarité du gain des différents PM du calorimètre hadronique.

Le groupe ATLAS de Clermont-Ferrand est à l'origine du développement de ce système. Ses contributions concernent, outre le LASER lui-même, toute son électronique de contrôle et l'ensemble du système de calibration interne. Afin de connaître la valeur de l'intensité lumineuse effectivement envoyée au calorimètre, il est en effet nécessaire de disposer d'un système de calibration indépendant.

Au cours de l'été 2004, le premier test en faisceau d'une tranche complète du détecteur ATLAS a été mis en place. La configuration des sous-détecteurs, l'électronique de traitement et le système de déclenchement mis en œuvre étaient proches de la configuration du détecteur ATLAS dans sa version finale.

La plupart des signatures de physique attendues dans l'expérience ATLAS mettent en jeu des jets dans l'état final. La reconstruction de l'énergie des jets constitue donc un enjeu fondamental. La collaboration s'est fixé comme objectif d'atteindre 1% de précision sur l'échelle en énergie absolue des jets. Une telle précision repose sur une bonne compréhension de la réponse des calorimètres d'ATLAS.

Cette étude débute avec une présentation du programme de physique de l'expérience ATLAS. Dans un deuxième chapitre le détecteur ATLAS est décrit. Ensuite, le calorimètre hadronique est présenté de façon détaillée. Dans le chapitre 4, les résultats de la validation du système LASER et de la calibration des PM du TileCal sont discutés. Les chapitres 5 et 6 sont consacrés à l'étude de la réponse du calorimètre aux pions des hautes énergies (de 20 à 250 GeV) et de basse énergie (énergies inferieures ou égales à 9 GeV).

Introduction

The present knowledge of the sub-atomic world deals with the systematization of the building blocks of matter in terms of families of quarks and leptons and the interpretation of fundamental interactions as carried by vector bosons. This Standard Model (SM) incorporates the Glashow-Weinberg-Salam theory of the electro-weak processes and Quantum Chromo Dynamics (QCD), while the gravitational interactions are not included. To each particle is associated an intrinsic property, the mass, except for photons and gluons, that are the intermediate bosons of electromagnetic and strong interactions respectively. Even if it is evident that macroscopic physics objects have a mass, the mechanisms with which elementary particles acquire their mass is nowadays not understood. In the Sixties a theory explicating the mechanism of mass generation was formulated. This theory, in the SM framework, predicts the existence of a massive boson, the Higgs boson, with an unpredicted mass value, but, on the basis of theoretical considerations, only with a constraint $m_H < 1$ TeV/c^2 . Past experiments at LEP and Tevatron gave only a lower limit on Higgs mass: $m_H > 114$ GeV/c^2 at 95% confidence level.

At this scope a proton-proton collider, the Large Hadron Collider (LHC), was designed. The Large Hadron Collider (LHC) is the machine that will provide the highest ever produced (by man) energy in the center of mass, reaching the value of $\sqrt{s}$=14 TeV for proton-proton collisions and giving the possibility to produce particles with mass up to few TeV. The main aim of the LHC experiments is the search for the Higgs boson, which is fundamental to verify the symmetry breaking mechanism in the electroweak sector of the Standard Model Theory and the simulation of the condition of the matter just after Bong Bang. In addition the LHC experiments will explore the existence and the predictions of possible supersymmetric models and will perform precision measurements of the heavy quarks. Four experiments are actually under commissioning phase on the LHC: ATLAS and CMS are two general purpose experiments, LHCb is mainly dedicated to CP symmetry violation studies and ALICE is going to exploit the heavy ions physics. The work presented in this thesis is carried on in the framework of the ATLAS experiment.

The work presented in this thesis is oriented into two axis:

1. the calibration of the photomultipliers of the ATLAS hadronic calorimeter (TileCal) with a LASER system,

2. the study of the response of the ATLAS calorimeters (LAR+TileCal) exposed to pions with energy between 3 and 250 GeV at 2004 combined test beam.

In the first chapter is presented a discussion about the Standard Model and the reasons why we are looking for an extension of it. In the second chapter a description of the ATLAS detector is given. Chapter three is dedicated to the description of TileCal. The structure of the apparatus and the different calibration systems used are explained.

In chapter 4 the LASER calibration system is described; after the description of the mechanical and electronical components, the results of the LASER system commissioning and of the TileCal photomulipliers calibration are presented.

Chapter five and six are dedicated to the study of the TileCal response to high energy pions (20-250 GeV) and low energy pions (3-10 GeV) respectively. The selection cuts, the values of the fractional energy response and resolution and their comparison with the Monte Carlo are presented.

Chapter 1

Theoretical overview

This chapter presents a basic overview where the current understanding of fundamental particles and their interactions are described.

1.1 The Standard Model

The Standard model (SM) of particle physics is a Quantum Field Theory (QFT) that at present is able to give us the best description of the fundamental particles and their interactions. In this theory we find structureless, elementary particles that constitute all the observed matter: the *quarks* and the *leptons*. The interactions between those particles are mediated by another kind of particles called *gauge bosons*. We can define the Standard Model as the theoretical framework used to calculate physical quantities, explain observed phenomena and make also predictions that need to be checked experimentally. During the past years this model realized great success in explaining and predicting results; it was tested with great precision in many experiments realized mainly at CERN, Fermilab, SLAC and DESY.

But despite the great success achieved, there is a consensus in the particle physics community that this isn't the final theory.

1.1.1 Matter particles and gauge bosons

As said before the Standard Model describes the characteristics of the fundamental constituents of matter and their interactions in terms of point like particles. A peculiar property of particles is their internal angular momentum called *spin*. So we can determine the nature and the properties of the particles looking at their angular momentum; following this procedure we can divide the particles into two categories: the *fermions* whose *spin* is $\frac{1}{2}\dot{\mathrm{h}}$ and the *bosons* whose *spin* is $1\dot{\mathrm{h}}$ (2h for the graviton). The *quarks* and the *leptons* are *fermions* and their interactions are described by the exchange of *gauge bosons*.

In table 1.1 are described the properties of the Standard Model particles. The *quarks* and *leptons* can be divided into families called generations, and

Flavor	Electric Charge (e)	Spin	Mass (GeV)	Baryon Number	L_e	L_μ	L_τ
Quarks							
u (up)	+2/3	1/2	0.0015–0.004	1/3	0	0	0
d (down)	−1/3	1/2	0.004–0.008	1/3	0	0	0
c (charm)	+2/3	1/2	1.15–1.35	1/3	0	0	0
s (strange)	−1/3	1/2	0.08–0.13	1/3	0	0	0
t (top)	+2/3	1/2	178	1/3	0	0	0
b (bottom)	−1/3	1/2	4.1–4.4	1/3	0	0	0
Leptons							
e (electron)	-1	1/2	0.511×10^{-3}	0	1	0	0
ν_e (electron neutrino)	0	1/2	$<3 \times 10^{-9}$	0	1	0	0
μ (muon)	-1	1/2	0.106	0	0	1	0
ν_μ (muon neutrino)	0	1/2	$<1.9 \times 10^{-4}$	0	0	1	0
τ (tau)	-1	1/2	1.78	0	0	0	1
ν_τ (tau neutrino)	0	1/2	$<1.8 \times 10^{-2}$	0	0	0	1
Gauge Bosons							
$W^\pm$ (charged weak)	± 1	1	80.403 ± 0.029	0	0	0	0
Z^0 (neutral weak)	0	1	91.1876 ± 0.0021	0	0	0	0
γ (photon)	0	1	0	0	0	0	0
g_i (i=1,...,8 gluons)	0	1	0	0	0	0	0
g (graviton)	0	2	0	0	0	0	0

Table 1.1: The fundamental particles of the Standard Model and some of their properties.

they are resumed in table 1.2 .

Looking at table 1.1 we define the Standard Model as a renormalizable gauge theory based on the simmetry

$$SU_T(2) \otimes U_Y(1) \otimes SU_C(3)$$

where T is the weak isospin, Y the hypercharge and C the color. The unified theory of electromagnetic and weak interactions relies on the symmetry $SU_T(2) \otimes U_Y(1)$ and physical processes are described in terms of γ, $Z^0$and $W^\pm$bosons exchange. Quantum Chromo Dynamics is a non abelian gauge theory based on a $SU_C(3)$ color symmetry which describes strongs (hadronic) interactions. The gauge bosons of the color field are 8 *colored glouns*.

Among the three quarks generations a mixing mechanism to reproduce observations on weak decays and to allow CP (Charge Parity) violation within the Standard Model exists and is parametrized by the Cabibbo-Kobayashu-Maskawa matrix (CKM)[1] defined by

$$\begin{pmatrix} d' \\ s' \\ b' \end{pmatrix} = V_{CKM} \begin{pmatrix} d \\ s \\ b \end{pmatrix} = \begin{pmatrix} V_{ud} & V_{us} & V_{ub} \\ V_{cd} & V_{cs} & V_{cb} \\ V_{td} & V_{ts} & V_{tb} \end{pmatrix} \begin{pmatrix} d \\ s \\ b \end{pmatrix} \qquad (1.1)$$

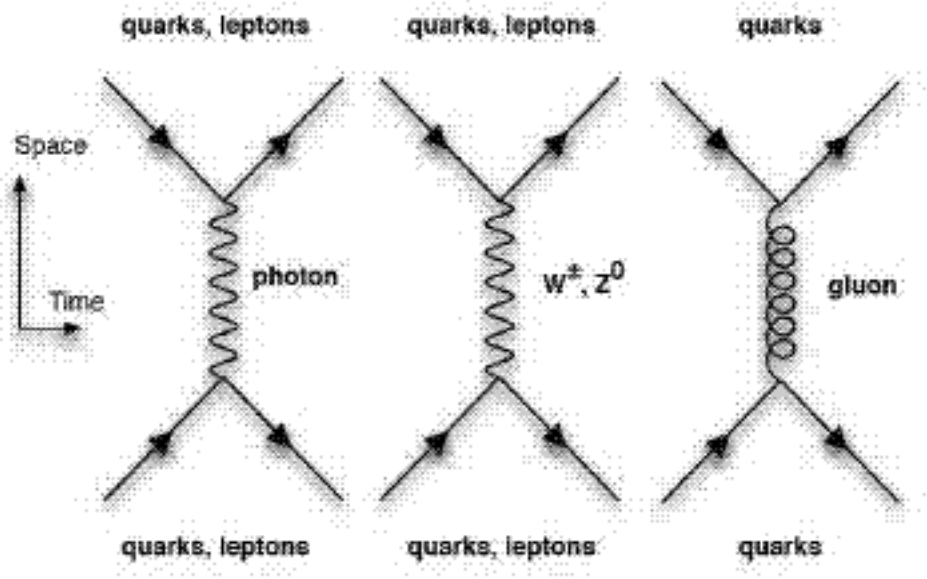


Figure 1.1: Feynmann diagrams showing the basic interaction between two fermions in the case of electromagnetic, weak or strong force.

and described in terms of three real parameters and one complex phase for a total of four free parameters. The Standard Model at present doesn't explain the origin of such a mixing.

Analysis on the Z decays width into hadrons, leptons and neutrinos performed at LEP, shows that if we assume lepton universality the family of neutrinos below the Z mass are exactly three.

Quarks do not exist as free particles, their combinations form the spectrum of particles called hadrons.

The three interactions are mediated, as said before, by different kinds of bosons, and in particular:

- $W^{\pm}$and Z^0mediate the weak force,
- The photon (γ) mediates the electromagnetic force,
- The gluons mediate the strong force.

In picture 1.1 you can find an example of force exchange between quarks and gluons through vector bosons.

1.1.2 Gauge symmetries

In section 1.1.1 we saw that in the Standard Model there are three different types of interactions: electromagnetic, weak and strong. We saw also that they are described in terms of a combination of three unitary gauge groups [2]:

$$SU(3) \otimes SU(2) \otimes U(1) \tag{1.2}$$

Where the group SU(3) represents the strong interaction, U(1) the electromagnetic interaction and $SU(2) \otimes U(1)$the unified electroweak interaction.

Those symmetries are of primary importance in particle physics. Consider that observables depend on the wave function squared, $|\psi|^2$. If the local guage invariance holds the transformation

$$\Psi \rightarrow \Psi' = e^{-i\chi(\overline{x},t)}\Psi \tag{1.3}$$

where $\chi(\overline{x},t)$is an arbitrary phase which depends on space and time coordinate, should leave the observables unchanged. From a physical point of view the choice of the phase should be not important because it cannot be measured. If successively we put Ψ and Ψ', into the Schrodinger equation for a matter particle

$$\frac{1}{2m}\nabla^2\Psi(\overline{x},t) = i\frac{\partial\Psi(\overline{x},t)}{\partial t} \tag{1.4}$$

the equation is clearly not invariant under the transformation coming from the equation 1.3. To assure the invariance of equation 1.4 we have to modify it. For an electrically charged particle the modified Schrodinger equation is

$$\frac{1}{2m}(-i\overrightarrow{\nabla} + e\overrightarrow{A})\Psi = (i\frac{\partial}{\partial t} + eV)\Psi \tag{1.5}$$

where e is the electric charge, V is the electric potential and $\overrightarrow{A}$ the potential vector. Now with this change, the Schrodinger equation is invariant under the transformations 1.3and

$$A \rightarrow A' = A + \frac{1}{e}\nabla\chi \tag{1.6}$$

$$V \rightarrow V' = V - \frac{1}{e}\frac{\partial\chi}{\partial t} \tag{1.7}$$

We have demonstrated that the local guage invariance of the theory, requires the presence of a field $A^\mu = (V, \vec{A})$. Further, since particles are viewed as an excitation of field the requirement of guage invariance leads to the presence of gauge bosons.

The equations written above are true only for massless scalar bosons, however massive bosons have been observed, $W^{\pm}$and Z^0. So physicist are looking for a mechanism that allows gauge bosons to acquire their mass. Right now the leading candidate is the Higgs mechanism that will be discussed later.

1.2 Electroweak Theory

The electroweak model is a gauge theory based on the *broken* symmetry of the group $SU(2)_L \otimes U(1)_Y$, where Y is the *weak hypercharge* related to the third component of the *weak isospin* $I_3$and to the electric charge through the formula,

$$Q = \frac{Y}{2} + I_3 \tag{1.8}$$

Fermions are introduced, in the theory, as *left-handed (L)* doublets and *right-handed (R)* singlets; this property comes from the helicity[1] of the fermion.

The relation between the coupling constants of the weak and electromagnetic interactions is

$$e = g \cdot \sin\theta_W \tag{1.9}$$

where e is the electric charge of the electron, g the coupling constant of the weak interaction and θ_W is the Weinberg's angle. A measure of this parameter can be obtained from:

- $\upsilon - e$ diffusion,
- electroweak interference in e^+e^-processes where a γ or a Z is exchanged,
- measure of the Z width,
- measure of the ratio between $W^\pm$ and Z masses.

From the combined analysis of those experiments the following results was quoted [3]:

$$\sin^2\theta_W = 0.213113 \pm 0.0005 \tag{1.10}$$

The W boson couples to quarks and leptons always with the same chiral status; this is also called *maximum parity violation.* The Z coupling depends also from the electric charge of the fermion involved, and if f is a generic fermion it can be expressed as:

$$g_Z(f) = \frac{g}{\cos\theta_W} \cdot (I_3 - z_f \cdot \sin^2\theta_W) \tag{1.11}$$

where $z_f$is the electric charge of the fermion expressed in units of the electric charge e.

In addition coupling constants for left-handed or right-handed fermions are not the same and they are resumed in table 1.2 and they can be written as

$$g_L = I_3 - z_f \cdot \sin^2\theta_W \tag{1.12}$$

[1] the helicity is defined as the component of spin along its direction of motion.

	ν_e, ν_μ, ν_τ	e, μ, τ	u, c, t	d', s', b'
g_L	$\frac{1}{2}$	$-\frac{1}{2} + \sin^2\theta_W$	$\frac{1}{2} - \frac{2}{3} \cdot \sin^2\theta_W$	$-\frac{1}{2} + \frac{1}{3} \cdot \sin^2\theta_W$
g_R	0	$\sin^2\theta_W$	$-\frac{2}{3} \cdot \sin^2\theta_W$	$\frac{1}{3} \cdot \sin^2\theta_W$

Table 1.2: Couplings between the Z boson and the fermions

$$g_R = -z_f \sin^2\theta_W \tag{1.13}$$

It is important to say that the mass eigenstates are not eigenstates of the weak interaction. They are parametrized by three mixing angles and one phase angle according to the Cabibbo, Kobayashi and Maskawa (CKM) formalism showed in matrix 1.1.

The numerical values in the matrix are [3]:

$$V_{CKM} = \begin{pmatrix} 0.9739 - 0.9751 & 0.221 - 0.227 & 0.0029 - 0.0045 \\ 0.221 - 0.227 & 0.9730 - 0.9740 & 0.039 - 0.044 \\ 0.0048 - 0.014 & 0.037 - 0.041 & 0.9990 - 0.9992 \end{pmatrix} \tag{1.14}$$

1.2.1 Electroweak symmetry breaking

The electroweak model is one of the best tested and verified theory in physics, nevertheless an incoherence is present. In fact, the symmetry in electroweak model requires all four bosons to be massless, but this assumption is clearly not verified by the experience where we observe very massive weak bosons.

In 1964 François Englert, Robert Brout and Peter Higgs proposed the hypothesis that the massless guage bosons of weak interactions acquire their mass interacting with a scalar field, the so called Higgs field, resulting in a single massless gauge boson (the photon) and three massive guage bosons [4, 5]. This is possible because the Higgs field has a potential function which allows degenerate vacuum solutions with a non zero vacuum expectation value.

The interaction between the particle and the Higgs field contributes to the particles energy respect to the vacuum, and this energy is equivalent to a mass. In the Standard Model only a doublet of scalar field is introduced. In the simplest model masses of quarks, leptons and bosons are all interpreted as the interaction with a unique scalar field. Particles that interacts strongly are the heaviest, while particle that interacts weakly are the lightest. Because of the fact that there is always a particle associated to a field, the theory predicts the existence of a spin 0 particle, called Higgs boson, that is the only particle not discovered in the Standard Model.

1.2.2 Higgs Boson searches

In section 1.2.1 we discussed about the prediction of the existence, in the Standard Model, of a scalar neutral boson that is the result of the spontaneous

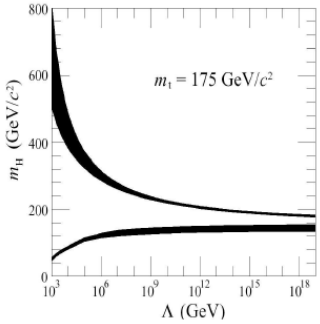


Figure 1.2: Theoretical limits on the Higgs mass as a function of the energy scale until the Standard Model is still valid. The black bands are the theoretical uncertainties.

electroweak symmetry breaking.

The Higgs boson coupling for leptons and quarks is proportional to $(g \cdot m_f)/2m_W$ where g is the coupling constant of the gauge theory $SU_L(2)$ and m_f the mass of the fermion.

The value of the Higgs mass comes from the Higgs potential parameters ν and λ present in the relation $m_H = \sqrt{2\nu^2\lambda}$. The parameter ν is the vacuum expectation value of the Higgs field and the theory says that it is equal to 246 GeV; but the theory is not able to predict the value for the parameter λ and as consequence neither the Higgs mass value. The only thing that is possible to do is to fix theoretical constraints to the Higgs mass as a function of energy scale at which the Standard Model is valid, as shown in picture 1.2.

In picture 1.2there is a very important information: if the Higgs boson exists and is mass is between $150GeV/c^2$and $180GeV/c^2$the Standard Model could be valid until the Planck mass scale at $10^{19}GeV/c^2$.

Lower limits on the Higgs boson mass can be determined by direct measure done at Tevatron and LEP. In picture 1.3 a global fit on LEP and Tevatron data with the Higgs mass treated as a free parameters gives as result $m_H = 84^{+34}_{-26}$. We have another value for the Higgs mass and it comes from LEP Higgs direct searches $m_H = 114.3GeV$ at 95% confidence level.

1.2.2.1 Higgs boson production modes

A Higgs boson may be created through the fusion of elementary constituents, by heavy fusion in the collision, or by radiation of massive virtual particles. The principal production modes of the Higgs at the LHC, summarized in picture 1.4, are [6]:

- Gluon fusion
- WW or ZZ fusion

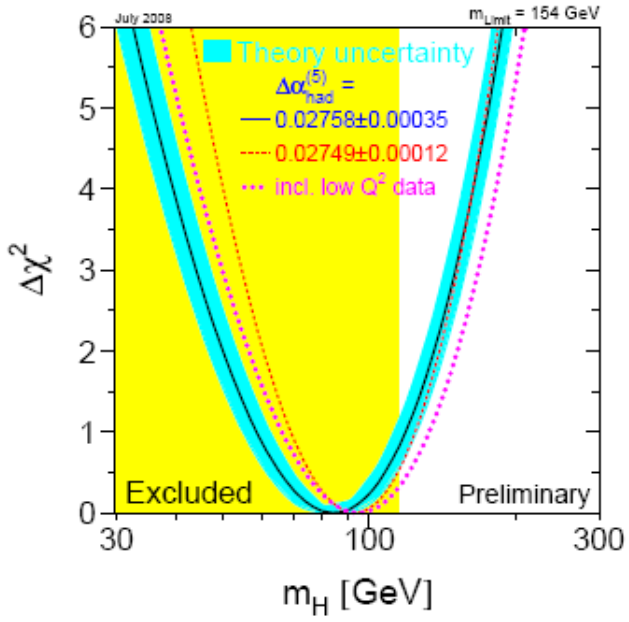


Figure 1.3: Global fit to the electroweak data with m_H as a free parameter. The band is theoretical error due to missing higher order corrections. The yellow band is the region excluded at 95% confidence level from direct searches on the Higgs mass.

- Higgs-strahlung W or Z
- Quark-antiquark fusion
- Higgs-strahlung from t or b quarks

The production is characterized by the presence of two quarks or a massive boson that radiates the Higgs.

At the LHC protons will collide with an energy in the center of mass of 14 TeV, at this energy the principal production process is , as you can se from picture 1.5, is the gluon-gluon fusion in which the Higgs boson is the direct product process (picture 1.4plot A).

The Higgs boson doesn't not couple directly with gluon, but through a t or a b quark loop, because the Higgs-quark coupling is directly proportional to the mass of the quark. As the Higgs mass increases, this coupling became smaller respect to the processes of production via WW or ZZ fusion. The channels in which the Higgs is in a final state with a W or a Z allow an effective experimental signature, because of intermediate vector boson identification. But those processes have the problem of a very small cross section, so they must be identified in a high background environment. The Higgs boson production

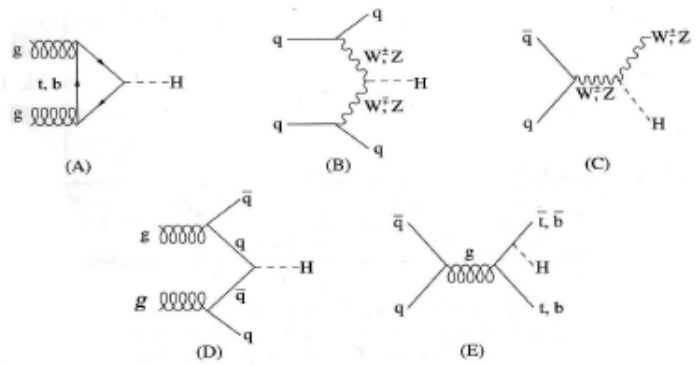


Figure 1.4: Feynmann diagrams of the principal Higgs production modes

cross section is resumed in picture 1.5, following the CTEQ4 parametrization of the proton structure function [7].

1.2.2.2 Higgs decays modes

The coupling of the Higgs boson with other particles is directly proportional to the mass of the particle itself, so the principal decay channels will be those in which they are massive particles, when the decay is kinematically allowed. The decays depend in particular from the mass of the Higgs. For the argument explained in section 1.2.2 we expect to find the Higgs in a region of mass between $115GeV/c^2$and $1TeV/^2$. In this interval the most important channels are:

- $H \to b\bar{b}$ at $80GeV/c^2 \leq m_H \leq 100GeV/c^2$
- $H \to \gamma\gamma$ and $H \to \tau\tau$ at $110GeV/c^2 \leq m_H \leq 150GeV/c^2$
- $H \to ZZ^* \to 4l^{\pm}$at $130GeV/c^2 \leq m_H \leq 2m_z$
- $H \to ZZ \to 4l^{\pm}, 2l^{\pm}2\nu$ at $m_H \geq 2m_Z$
- $H \to WW \to l\nu 2jet$ at $m_H$until $1TeV/c^2$

In picture 1.6 the branching ratios for the different Higgs channels decays are resumed. It is important to notice that for higher values of the Higgs mass the dominant decay channels are into WW and into ZZ.

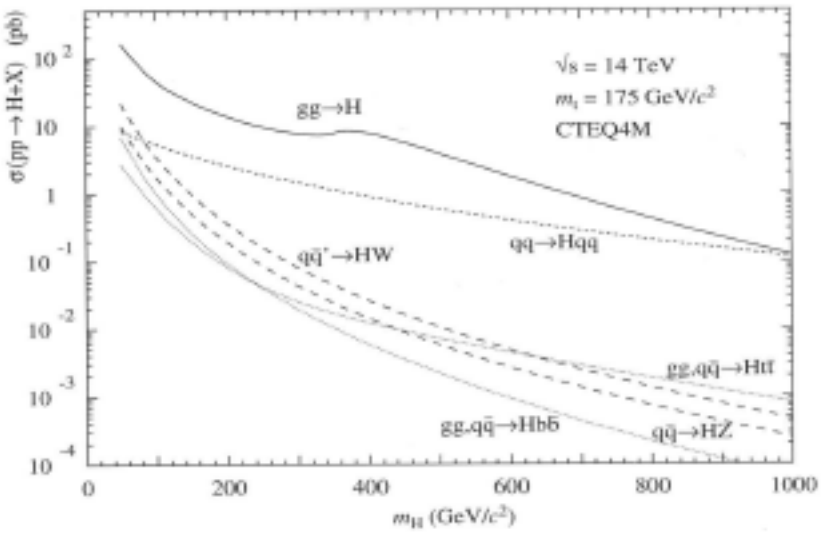


Figure 1.5: Higgs boson production cross section

Particles coming from Higgs decay have short mean lifetime, because of the fact that they are heavy, so only decay products can be detected and the main experimental signatures can be divided into four categories:

- charged tracks (electrons and muons),
- jets (quarks and hadrons),
- slim jets (from τ decay),
- electromagnetic showers (electrons and photons),
- missing transverse energy (neutrinos).

As we have seen the Higgs decay modes depends strongly on the Higgs mass. It is for that reason that different strategies depending on the mass region have been appointed:

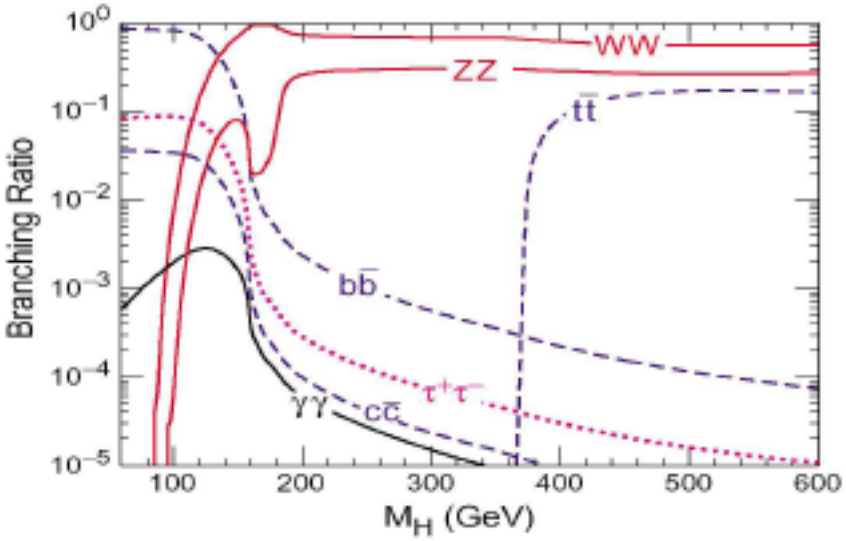


Figure 1.6: Branching ratios of the Higgs boson

- In the *low mass region* the channel $H \to b\bar{b}$ has a branching ratio close to 1 but the signal-background tatio is very small due to the QCD background, so the channel $H \to \gamma\gamma$ will be favorised in the search because despite the small branching ratio the ratio signal background make this channel interesting.
- In the intermediate mass region the most powerful channels are $H \to ZZ^* \to 4l$ or $H \to WW^* \to l\nu l\nu$.
- In the high mass region the discovery should be easy in the channel $H \to ZZ \to 4l$. In particular the signal could be extracted from the background requiring a high invariant mass for two lepton pairs.

To determine the importance of a channel is useful to define a variable called *statistical significance* defined as $N_S/\sqrt{N_B}$, where N_S and N_B are the number of events for the signal and for the background. In figure 1.7 it is shown as function of the Higgs mass for the different decay modes[6] and after four year of data taking.

1.3 Beyond the Standard Model

As said before there are several indications to believe that Standard Model is not the final theory and that there is a more fundamental theory left to be discovered. Only experiments in the coming years will say which is the right

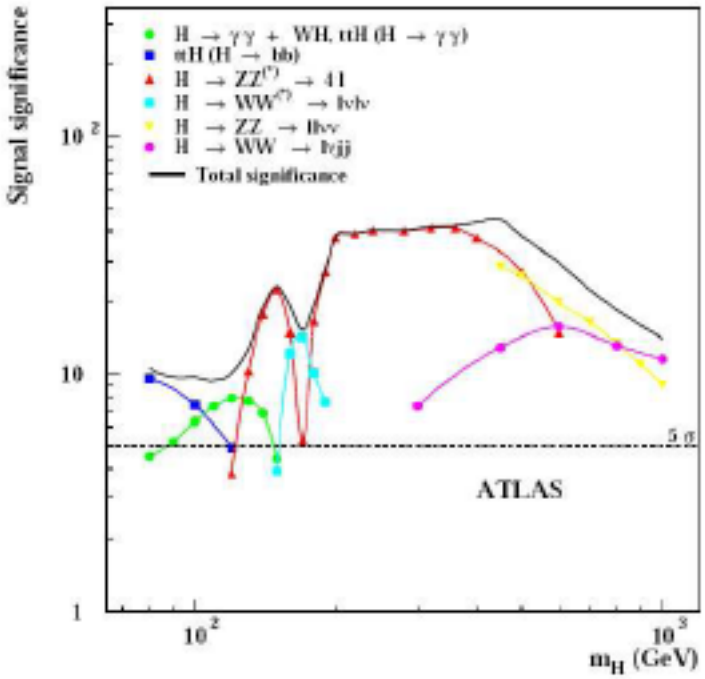


Figure 1.7: Statistical significance for the discovery of a Standard Model Higgs boson in different channels after for years of data taking.

one between the several proposed. In this section I will only explain few reasons to believe in an extension.

1.3.1 Limitations of the Standard Model

The first reason for introducing an extension of the Standard Model comes from the inclusion of Higgs boson in the Standard Model. In fact this procedure leads to some unphysical results like perturbative calculations of the mass of the Higgs boson squared have quadratic divergences or the infinite terms that appear in the sum.

A second reason arises from the fact that several theoretical unifications of forces have already occurred. Electricity and magnetism were once thought of as unrelated, as were the electromagnetic and weak forces. Thus, many theorists expect that a theory that unifies all of the forces should be the final theory. The Standard Model separates the unified electroweak forces from the strong force, and does not include gravity.

These coupling strengths have a dependence on the interaction energy; more precisely, they depend on the momentum transfer Q between two particles involved in an interaction. Figure1.8 shows the values of the coupling strengths

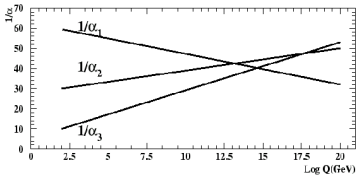


Figure 1.8: Evolution of the coupling strengths as a function of energy in the Standard Model, where α_1 corresponds to U(1) (electromagnetic force), α_2 corresponds to SU(2) (electroweak force), and α_3 corresponds to SU(3) (strong force).

as a function of Q. Theoretical calculations in the Standard Model predict that the coupling strengths are closer at high energies than at lower energies. The experimental data taken so far agree. However, the coupling strengths will not meet exactly without the existence of some new physics which affects their dependence on the energy.

Chapter 2

The LHC and the ATLAS detector

2.1 The LHC project

The *Large Hadron Collider [8]* that has been installed at CERN in the existing LEP(Large Electron Positron Collider) tunnel. It has been designed for a center of mass energy of 14 TeV in the case of proton-proton collisions and of 1125 TeV in case of collisions between Pb ions.

Protons are preaccelerated by the CERN accelerator system, shown in figure2.2 composed by:

- a LINAC in charge of the protons injection,
- a Protosyncrothron(PS) that will accelerate particles until 26 GeV,
- a Super-Protosyncrothron(SPS) that will accelerate particles until 450 GeV before the injection in the LHC.

The LHC will provide a rich physics potential, ranging from the search for new physics phenomena to more precise measurements of Standard Model parameters. Furthermore, nucleus-nucleus collisions at the LHC provide an unprecedented opportunity to study the properties of strongly interacting matter at extreme energy density. The two proton beams will travel in the opposite direction along two rings (the radius of each ring is about 4.2 Km) crossing each other in eight points. In four of these intersections there are the following detectors:

- ATLAS, A Toroidal LHC ApparatuS,
- CMS, Compact Muon Solenoid,
- ALICE, A Large Ion Collider Experiment,
- LHCb, Large Hadron Collider bphysics.

The two proton beams will pass through oppositely directed field of 8.38 Tesla. These fields are generated by superconducting magnets operating at 1.9 K. The

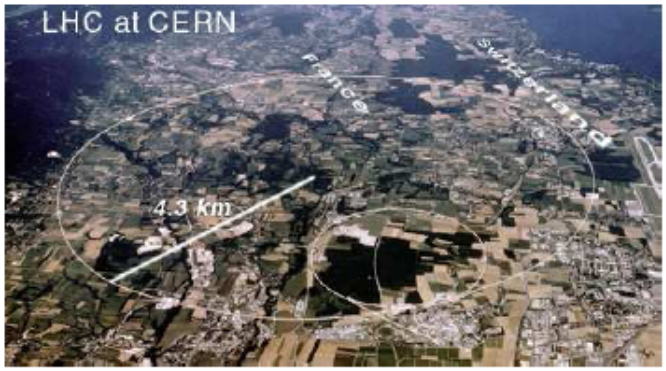


Figure 2.1: The Large Hadron Collider

protons will come in roughly cylindrical bunches, few centimeters long and few microns in radius. The distance between bunches is 7.5 m, in time 25 ns.In the high luminosity phase ($10^{34} cm^{-2} s^{-1}$), the two beams will be made of 2808 bunches of about 10^{11} protons each. During the initial phase, LHC will run at a peak lower luminosity of $10^{33} cm^{-2} s^{1}$.

In figure 2.2 the injection system and the main LHC nominal parameters are shown.

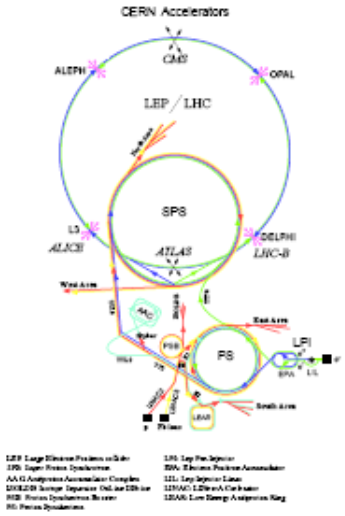
2.2 Definitions and conventions

The coordinate system and nomenclature used for describing the detector and the particles emerging from the p-p collisions are briefly summarized here as they are used repeatedly throughout this thesis.

The axis origin is on the center of the nominal interaction point, the z axis is the same of the beam counterclockwise, while the orthogonal plane is the (x; y) plane. The x axis is positive in the direction of the ring center, while the y has positive direction pointing up. In figure those conventions are summarized. Other useful variables are the radial coordinate R, measured from the interaction point, the azimuthal angle ϕ and the polar angle θ, defined in this way:

$$R = \sqrt{x^2 + y^2}$$

$$\phi = \arctan \frac{y}{x} \tag{2.1}$$



LHC nominal parameters	
Beam energy	7 TeV
Magnetic field of the dipoles	8.33 T
Bunch spacing	24.95 ns
Number of bunches	2808
Radius of the bunch at the interaction point	16 μm
Bunch length	7.7 cm
Number of particle in a bunch	$1.1 \cdot 10^{11}$
Luminosity	10^{34} cm^{-2}s^{-1}
Crossing angle	300 μrad
Circulating current	0.56 A
Energy lost per round	7 keV
Total radiated power for a beam	3.8 kW

Figure 2.2: The LHC accelerator system and his nominal parameters.

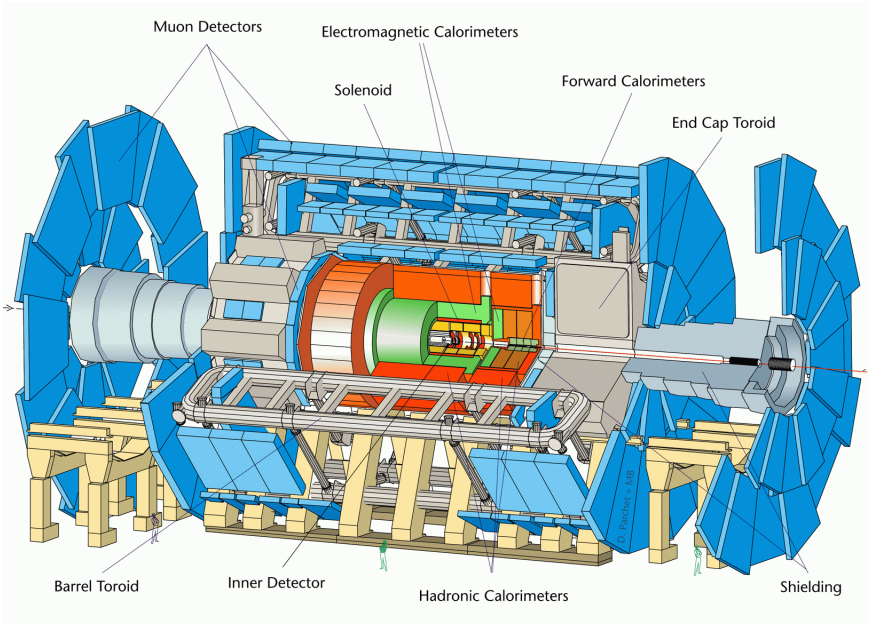


Figure 2.3: The ATLAS detector

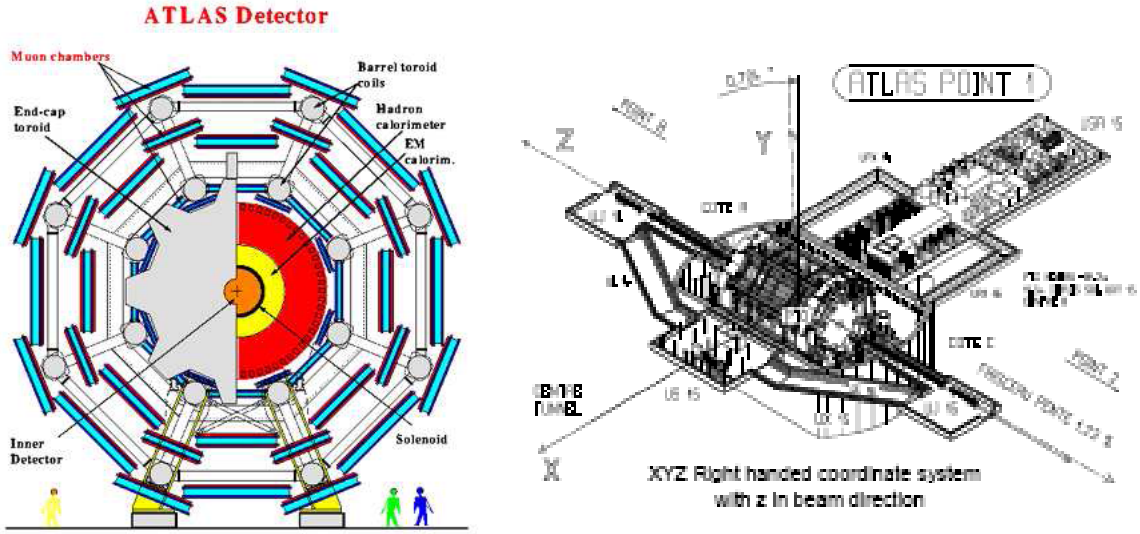


Figure 2.4: ATLAS transverse view and framework.

$$\theta = \arccos \frac{z}{\sqrt{R^2 + z^2}} \tag{2.2}$$

Instead of the polar angle ϑ it is useful to define the quantity called pseudo-rapidity, defined as η = -ln tan($\vartheta/2$). Such variable allows distributions $\Delta\eta$ that are Lorentz invariant along the z axis for ultra-relativistic particles. The ATLAS detector, as in figure 2.5, is geometrically divided in three sections:

- Barrel, at $\eta < 1.05$
- Extended Barrel or transition region, at $1.4 < \eta < 1.05$
- End-cap, at $\eta > 1.4$

2.3 Physics Requirements

The LHC luminosity and resulting interaction rate are needed because of the small cross-sections expected for many of the processes mentioned above. However, with an inelastic proton-proton cross-section of 80 mb, the LHC will produce a total rate of 10^9 inelastic events/s at design luminosity. This presents a serious experimental challenge as it implies that every candidate event for physics will on the average be accompanied by ~20 inelastic events per bunch crossing. The nature of proton-proton collisions imposes another difficulty: jet production cross-section dominate over the rare processes mentioned above,

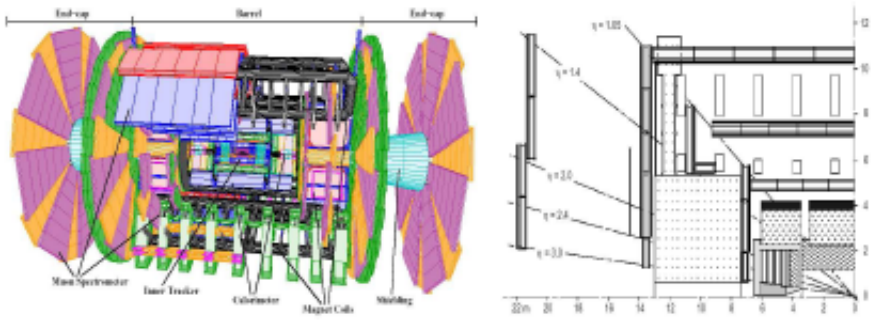


Figure 2.5: ATLAS regions in the R-z plane

requiring the identification of experimental signatures characteristic of the rare physics processes in question, such as E_{Tmiss} or secondary vertexes. Identifying such final states for these rare processes imposes further demands on the particle-identification capabilities of the detector and on the integrated luminosity needed. Viewed in this context, these benchmark physics goals can be turned into a set of general requirements for the detector:

- a good charged-particle momentum resolution and reconstruction efficiency in the inner tracker. For offline tagging of τ-leptons and b-jets, vertex detectors close to the interaction region are required to observe secondary vertexes;
- a very good electromagnetic (EM) calorimetry for electron and photon identification and measurements;
- a full-coverage hadronic calorimetry for accurate jet and missing transverse energy measurements;
- an high precision muon system that guarantees accurate muon momentum measurements over a wide range of momenta;
- a very efficient trigger system on high and low transverse-momentum objects (minimum bias events) with sufficient background rejection.

ATLAS has been designed in order to satisfy those requirements.

2.4 The magnetic system

The magnetic system [10] consists of a central solenoid (CS) that provides a solenoidal field of 2 Tesla for the inner detector and three large air-core toroids, two in the end-caps (ECT) and one in the barrel (BT) that generate the magnetic field in the muon spectrometer (see figure 2.6).

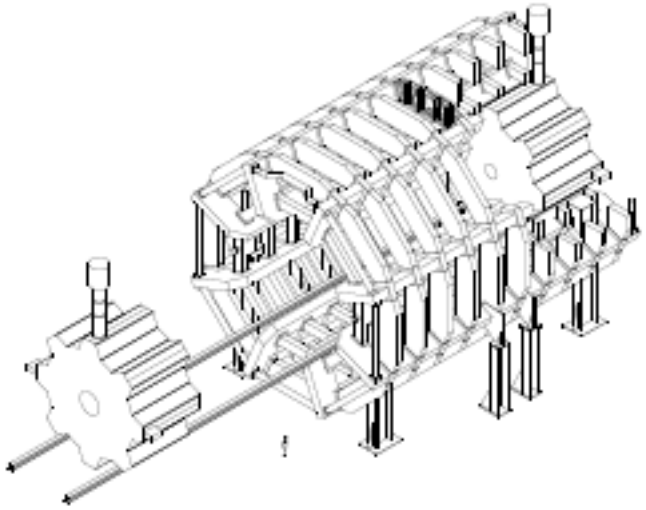


Figure 2.6: View of the superconducting air-core toroid magnet system

The CS creates a solenoidal field with a nominal strength of 2 T at the interaction point. The position in front of the electromagnetic calorimeter requires a careful minimization of matter in order to avoid showering of particles before their enter in the calorimeter. The design of magnetic system was motivated by the need to provide the optimized magnetic field configuration while minimizing scattering effects. The two end-cap toroids (ECT) are inserted in the barrel toroid (BT) at each end and line up with the central solenoid. Each of the three toroids consists of eight coils assembled radially and symmetrically around the beam axis. Both BT and ECT generate a precise, stable and predictable magnetic field ranging from 3 to 8 Tm for the muon spectrometer. This field is produced in the barrel region ($|\eta| \leq 1.0$) by the BT and in the forward region ($1.4 \leq |\eta| \leq 2.7$) by the ECT, while in the transition region ($1.0 \leq |\eta| \leq 1.4$), it is produced by a combination of the two. Due to the finite number of coils, the magnetic field provided by the toroids is not perfectly toroidal: it presents strong discontinuities in transition regions, as it can be seen in figure 2.7. The lines are drawn in a plane perpendicular to the beam axis in the middle of an end-cap toroid and the range between two consecutive lines is of 0.1 T.

2.5 The inner detector

The inner detector (ID) [11] is the innermost part of ATLAS and his role is to reconstruct the production and decay points (vertexes) of charged particles as well as their trajectories.

The inner detector has been designed to match with the following require-

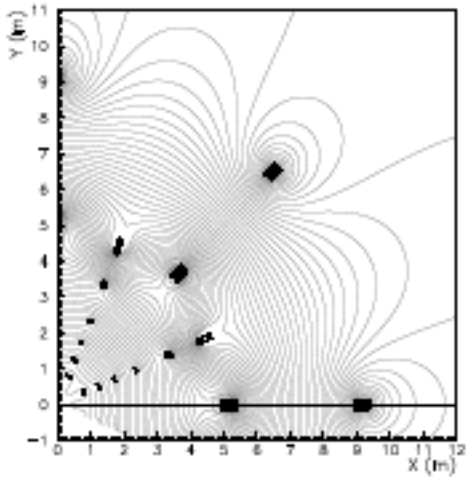


Figure 2.7: Magnetic toroid field map in the transition region, the lines are drawn in a plane perpendicular to the beam axis in the middle of an end-cap toroid.

ments:

- tracking capability up to $|\eta|<2.5$,
- transverse momentum resolution $\frac{\Delta p_T}{p_T} < 30\%$ at $p_T = 500 GeV/c$ and $|\eta|<2$,
- high efficiency (95%) for isolated tracks with $p_T > 5 GeV/c$,
- good impact parameter resolution to tag b quarks and τ's through secondary vertex identification.

An overview of the inner detector is given in figure 2.8. Its outer radius is R=115 cm and it is about 7 m long. It is divided in three zones: in the central (|z|<80 cm, barrel) detectors are placed in rings centered on the beam line while in the forward regions (end-caps) they are arranged in wheels orthogonal to the beam line. It is placed within a solenoidal magnetic field of 2T.

Pixel The pixel detector is the closest to the interaction point and it is composed by three layers in the barrel and five disks in each end-cap. The system provides three precise measurements over the full solid angle (typically three pixel layers are crossed), with the possibility to determine the impact parameter and to identify short-life particles. The required high resolution is provided by 80 millions individual square pixels of 50 μm in r $-\Phi$ and 400 μm in z. The pixel detector yields excellent spatial resolution in the bending plane of the solenoidal magnetic field, essential for transverse momentum measurement. The position along the beam axis is measured with less precision.

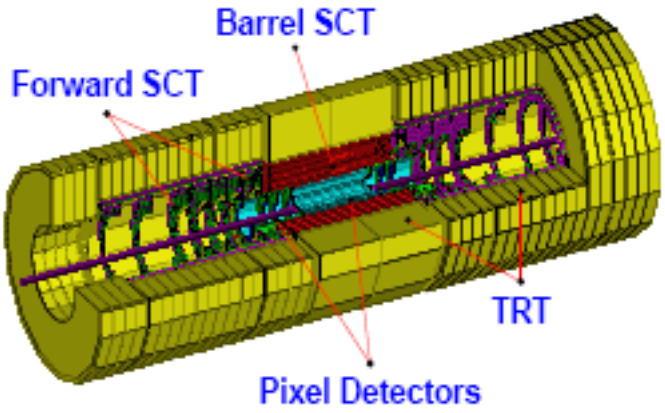


Figure 2.8: Layout of the inner detector

SCT The Semiconductor Tracker (SCT) is made of silicon detector segmented in pixels (2 layers in the barrel region and 8 wheels in the end caps) or in strips (4 layers in the barrel). Single point resolution is 13 μm.

TRT The Transition Radiation Tracker (TRT) is made of drift straw tubes filled with a Xenon gas mixture with a single point resolution of 130 μm; polypropylene radiators are provided to generate transition radiation which gives additional electron identification ability.

2.6 Calorimeter System

The ATLAS calorimeter [12, 13, 14] has been designed to meet the different requirements of the LHC physics program while operating in a very high luminosity environment. This system must be able to reconstruct the energy of electrons, photons and jet. It has as well a large hermeticity for measuring missing transverse energy.

It is divided into an Electromagnetic (EM) Calorimeter and a Hadronic Calorimeter each consisting of a barrel and two end-caps. The Electromagnetic Barrel Calorimeter (EMB) covers the pseudorapidity $|\eta| < 1.475$, the Electromagnetic End-Cap Calorimeter (EMEC) covers $1.375 < |\eta| < 3.2$, the Hadronic End- Cap Calorimeter (HEC) covers $1.5 < |\eta| < 3.2$, the Forward Calorimeter (FCAL) covers $3.1 < |\eta| < 4.9$, and the Tile Calorimeter (TileCal) covers $|\eta| < 1.7$.

Because of its good hermeticity, the calorimeter as a whole provides a reliable measurement of the missing transverse energy ($E^{miss}{}_T$). Together with the Inner detector, the calorimeter provides a robust particle identification exploiting the fine lateral and good longitudinal segmentation.

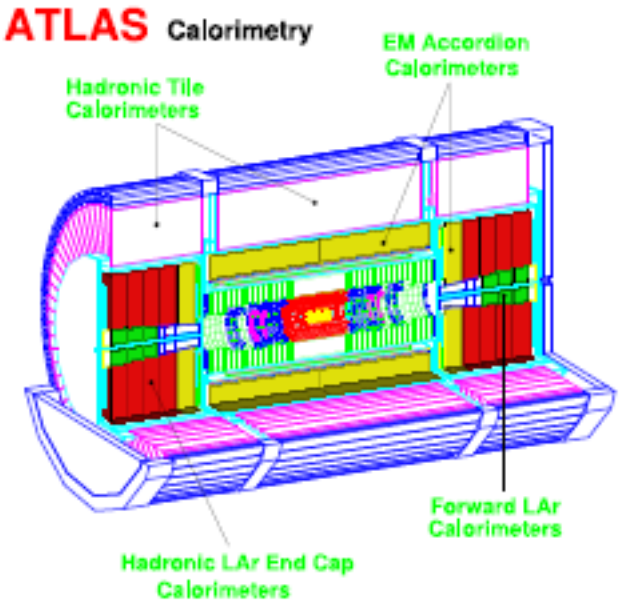


Figure 2.9: The ATLAS calorimeter system.

Electromagnetic calorimeter (LAr) A barrel cryostat around the inner detector cavity contains the barrel electromagnetic calorimeter and the solenoidal coil which supplies a uniform field in the inner tracking volume. This coil is placed in front of the electromagnetic calorimeter. Two end cap cryostats enclose the electromagnetic and hadronic end cap calorimeters as well as the integrated forward calorimeter. The barrel and extended barrel hadronic calorimeters are contained in an outer support cylinder, acting also as main solenoid flux return. The outer radius of the calorimeter is 4.23 m. The electromagnetic calorimeter uses lead absorbers in liquid Argon; it is implemented in an accordeon geometry.

The total EM calorimeter presents a ~20 radiation length in the barrel and in the end-caps region to reduce the error in the energy resolution due to longitudinal fluctuations of high energy showers due to longitudinal leakage. The particle identification is achieved by a fine longitudinal and lateral segmentation. The EM calorimeter is longitudinally segmented in three layers plus a pre-shower sampler that corrects the energy loss in the material in front of the EM.

The EM is expected to provide an excellent energy resolution:

$$\frac{10\%}{\sqrt{E(GeV)}} \oplus 0.7\% \tag{2.3}$$

In chapter 3 the ATLAS hadronic calorimeter will be described in detail.

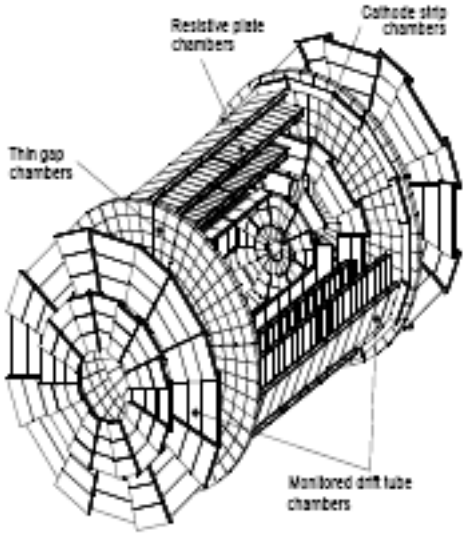


Figure 2.10: The ATLAS muon spectrometer

2.7 The muon spectrometer

The muon spectrometer [15] represents the outer part of the experiment and it is the main part of its volume: the inner radius is 4.5 m, the outer radius is 11 m and its length along z is 46 m. It is designed to detect charged particles exiting the barrel and end-cap calorimeters and to measure their momentum in the pseudorapidity range $|\eta| < 2.7$. The accurate determination of the momenta of muons allows the precise reconstruction of the short-lived particles that decay into muons (particles containing b or c quarks).

The conceptual layout of the Muon Spectrometer is shown in figure 2.10: the different technologies employed are indicated. In order to have the more as possible accurate measurement of the momentum, independently from the inner detector, the design of the muon spectrometer uses four different detector technologies including two types of trigger chambers and two types of high precision tracking chambers.

Cathod Strip Chambers (CSC) The CSC are multiwire proportional chambers with both cathodes segmented, one with the strips perpendicular to the wires providing the precision coordinate and the other parallel to the wires providing the transverse coordinate. The position of the track is obtained by interpolation between the charges induced on the cathode strips.

Their spatial resolution is better that 50 μm. They are situated after the calorimeter in the forward region ($2.0<|\eta|<2.7$) in a region where the background is elevated and so they must have a fine granularity to reject it.

Monitored Drift Tubes (MDT) A monitored drift tube (MDT) chamber consists of three or four layers (a multilayer) of 30 mm diameter cylindrical drift tubes each outfitted with a central W-Re wire on each side of a supporting frame. The MDT chambers perform the precision coordinate measurement in the bending direction of the air-core toroidal magnet and therefore provide the muon momentum measurement. The four layers chambers are located in the innermost muon detector stations where the background hit rates are the highest. An additional drift-tube layer makes the pattern recognition in this region more reliable.

They are filled with a of a Ar-CO_2mixture and they have a spatial resolution of 60 μm and the drift time in a tube is equal to 600 ns.

Resistive Plate Chambers (RPC) The RPC is a gaseous parallel electrode-plate (i.e. no wire) detector. Each of the two rectangular detector layers are read out by two orthogonal series of pick-up strips: the η strips are parallel to the MDT wires and provide the bending view of the trigger detector, the Φ strips orthogonal to the MDT wires provide the second coordinate measurement which is also required for the offline pattern recognition. The use of the two perpendicular orientations allows the measurements of the η and Φ coordinates. The RPC combine an adequate spatial resolution of 1 cm with an excellent time resolution of 1 ns.

Thin Gap Chambers (TGC) They are very thin multi-wire proportional chambers The peculiarity of TGC compared to regular MWPC is that cathode-anode spacing is smaller than the anode-anode (wire-wire) spacing. This characteristic allows a shorter drift time and an excellent response in time of less than 20 ns, which meets the requirement for the identification of bunch crossings at 40 MHz.

The TGC are filled with a highly quenching gas mixture of 55%$CO_2$and 45%n-pentane C_5H_{12}. This allows TGC to work in a saturation operation mode with a time resolution of 5 ns and with good performances in a high particle flux.

Chapter 3

ATLAS hadronic calorimeter

In this chapter a description of the hadronic calorimeter installed in the central part, $|\eta| \leq 1.475$ of the ATLAS detector will be given. In this region the tilecal (scintillating tiles) calorimeter assures the hadronic calorimetry.

All the studies that will be shown in the following of this thesis will concern this detector. In particular the calibration with a LASER system of the tilecal and the combined response to charged pions to 3 up to 250 GeV will be discussed.

3.1 Tilecal calorimeter

The ATLAS hadronic calorimeter is composed by three cylindrical parts called barrels. The central part of the calorimeter covers a region in eta between -1 and 1; this zone is called long barrel. The other two regions called extended barrel complete the calorimeter and they cover a zone in pseudorapidity up to $\eta \tilde{}1.7$. Each barrel is composed by 64 sectors, called modules. In figure 3.1 is shown a portion of the calorimeter, and in particular an half part in the long barrel and one part in the extended barrel. Tilecal is symmetric towards the direction $\eta = 0$ and with respect to the beam line. The total number of modules in the calorimeter is 64 for the long barrel and 2x64=128 for each of the extended barrels.

Tilecal is segmented in three different layers called A, BC, D along the radial direction. Each layer is divided into cells, with a dimension of 0.1 in unit of pseudorapidity, for the layers A and BC and of 0.2 for the layer D.

Tilecal is a sampling calorimeter made by layers of absorber material, iron, and by layers of active material, scintillating tiles. If we look at the calorimeter along the radial direction we see that in each module we have 11 rows of scintillating tiles [16], separated by iron layers.

Figure 3.2 shows, for the half of a central module, the position of the 11 rows of scintillating tiles with a zoom that shows how the active material and the absorber placed in a module.

The conception of the Tilecal has the particularity to have the scintillating

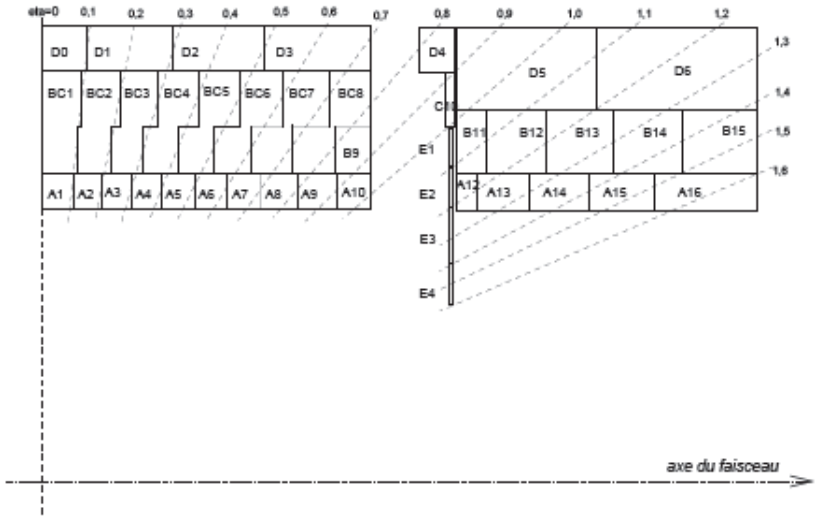


Figure 3.1: Section of a portion of the ATLAS hadronic calorimeter

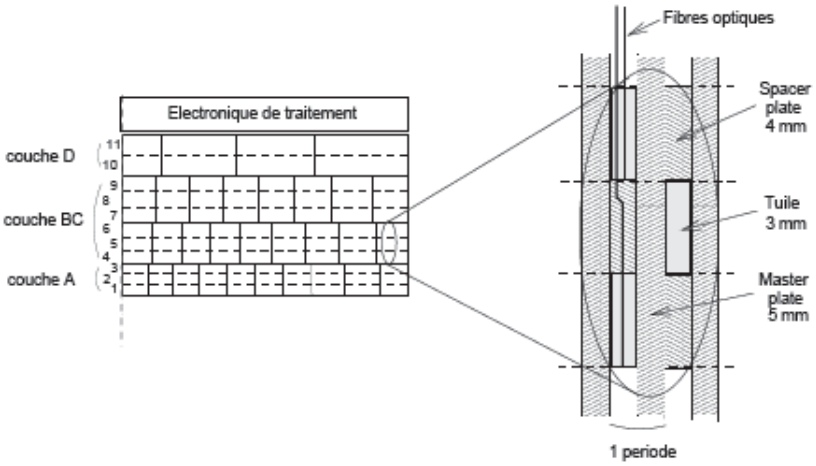


Figure 3.2: Schema of the scintillating tiles position in a tilecal module

tiles placed perpendicularly to beam axis, this configurations allows to have a biggest number of exploitable channels and to place the electronic at the top of module, in a region with a small radiation environment but with the inconvenient that the sample fraction depends strongly from the pseudorapidity.

For each tile the light is collected by two clear fibers situated at the two sides of the module.

3.2 Signal production

Scintillating tiles are are composed by polystyrene doped with *PTP (*1.5%) and with *POPOP* (0.04%). A particle that pass through the tiles generates an excitation of the middle, a fraction of the material during the disexcitation emits photons in the ultraviolet region (230 nm). Those photons are absorbed by the dopant components and remitted in the blue. The amount of light produced is proportional to the energy of the incident particle and it is expressed by the *Birk's law:*

$$\frac{dL}{dE} = L_0 \frac{dE/dx}{1 + k_b dE/dx} \tag{3.1}$$

Where L is the luminance, $L_0$is the luminance obtained for a small density ionization and k_ba constant depending from the scintillating material choosen.

As said before the scintillation light produced by a tile is collected by optic fibers that have the properties to absorb the light and remit that at a frequence of 480nm (green) where PMTs have a better sensibility. Then the light is sent, via a toron of fibers to the PMTs where thanks to a light mixer, placed at the entrance of the PMTs, the light is uniformed. In each PMT the number of photoelectron is about 30 per GeV [17].

3.3 Signal reconstruction

Each Tilecal module has is own electronic that is independent form the others modules; the totality of the electronic is placed into two support called drawers. In each drawer there are 24 places for the PMTs and the drawers are coupled to form the so called superdrawers. In figure 3.3 the different components of a drawer are illustrated. The drawers are inserted at the top of each module. The photomultipliers are placed into iron cylinder, called PMT block, in order to be protected from magnetic field produced by the toroid. Inside the PMT block we find also the HV card, in charge to send the high voltages at the different stages of the PMT, and a card in charge of the shaping of signal called "3 in 1".

The electronic placed in the drawers must assure the following tasks:

- distribution of the HV at the photomultipliers. To achieve the performances requested the gain of the PMTs must be stable at 1%, so we want be able to correct the value of the gain in order to equalize the response of the different Tilecal cells,
- signal fast reconstruction for the first level trigger and for the determination of the region of interest in the calorimeter,
- digitization of signal if it is accepted by the first level trigger.

In figure the principal elements of the electronic are shown.

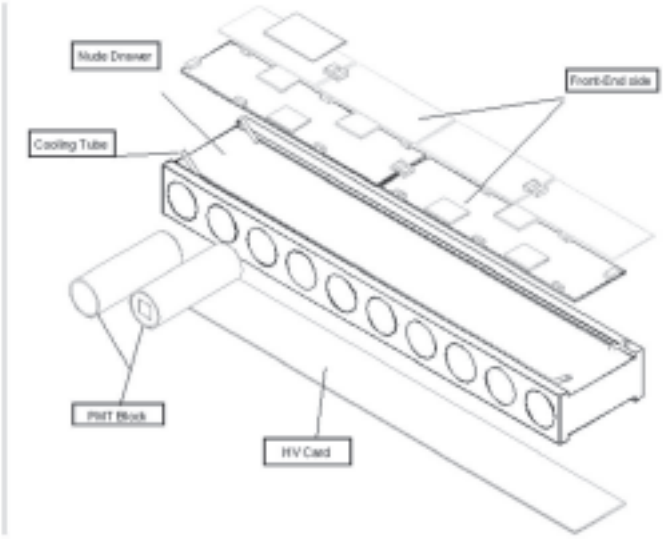


Figure 3.3: Illustration of a tilecal drawer

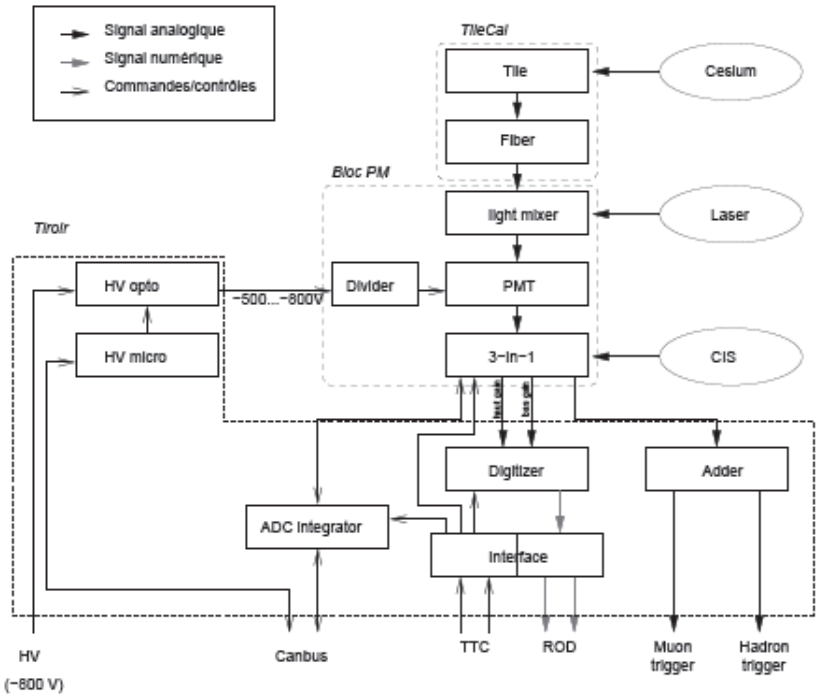


Figure 3.4: Schema of the tilecal electronics

3.3.1 HVmicro card

Using a communication bus *CANbus* this card controls the distribution of the high voltages to the photomultipliers. In this card there is a EEPROM programmable memory, containing the nominal values of the HV that must be applied.

3.3.2 HVopto card

In each superdrawer there are two cards of this type; they receives the value of the HV from the HVmicro card. The HV is set at the nominal value of -800 V and after that set at the value received from the HVmicro card with a precision of 0.2 V. With this card we can control 24 PM.

3.3.3 Divider card

It is present in each PMT and it is in charge to give the HV value at each stage of the photomultiplier.

3.3.4 "3 in 1" card

It is present in each PMT and it is in charge to assure the three following functions:

- PMT signal shaping,
- charge injection
- PMT signal integration

The last two points are related to the calibration system of the calorimeter and they will be discussed later. The electronic responsible of the shaping of the signal generates a signal where the height and the integral are proportional to the energy deposited in the cell. At the exit of the card the signal is amplified with two different gains, low gain and high gain. The amplification factor between the two gains is 64. In figure 3.5 the normalized analog signal coming from the 3 in 1 card for a physic event is shown.

The full width at half maximum is 50 ns and it is independent from the height of the peak.

3.3.5 Digitizer card

In each superdrawer there are 6 or 8 Digitizer cards. It is at this stage that the digitization of the analog signal coming from the "3in1" card is realized. Each digitizer card have 6 channels connected to the output of the "3in1" cards. A TTC_{rx}*circuit (Timing Trigger Control Receiver)* allows to decode the *TTC(Timing Trigger Control)* information carried by the Interface card . The digitization of the signals is realized using two ADC circuit with a

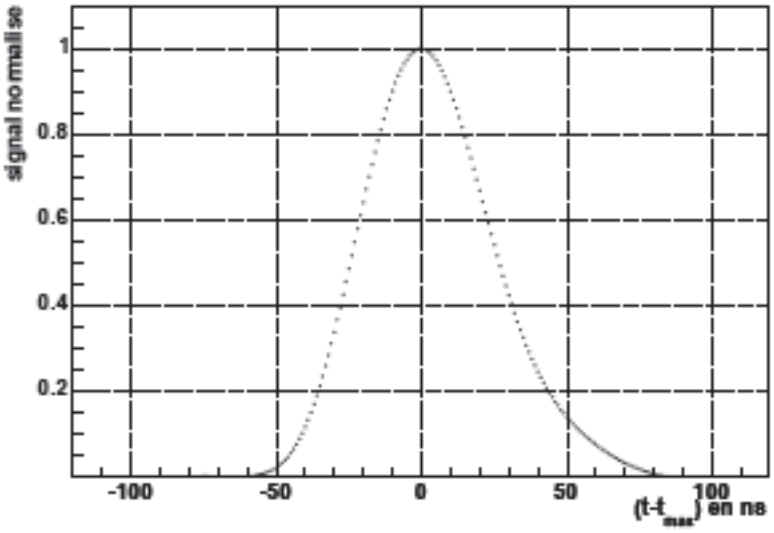


Figure 3.5: Normalized analog signal shape coming from the 3 in 1 card.

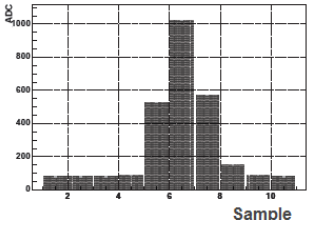


Figure 3.6: Shape of a digitized signal at the output of the Digitizer card

dynamic of 10 ADC, and the choice of the gain is done automatically. The signal is sampled each 25 ns and the total number of sample is programmable. Once the signal is digitized is saved on a buffer during 2.5 μs in order to wait the decision of the level 1 trigger and if it is accepted is sent to the Interface card. In figure 3.6 an example of a digitized signal is shown.

3.3.6 Interface card

This is an optoelectronic interface and each superdrawer is equipped with one these cards. It receives the information from the TTC using two optic fibers (the information is doubled in order to not lost the control of one superdrawer if a fiber is broken) and converts it into an electric signal then dispatched to the different TTC_{rx} circuit. Then they are transformed in optical signals and they are sent to the ROD (Read Out Driver) using two optic fibers. This card receives also the signals coming from the Digitizer card.

3.3.7 Adder card

Each superdawer has between 7 and 9 Adder cards. The six output coming from the "3in1" cards are connected at these cards, and each one of them correspond to cells placed in a projective tower in eta. Each card does the analog sum of the photmultipliers signals coming from the same tower. This card has two outputs, the first one called *Hadron trigger* send the signal measured in each tower; the second one called, *Muon Trigger*, send the signal measured in the cells of the last layer of the tilecal.

3.4 Filter algorithms

At the output of the Digitizer card the digitized signals of the n samples are avaible. They are sampled each 25 ns after the start of the acquisition given by the trigger. Some algorithms are avaible to reconstruct the sampled signal and obtain the energy of the event. Two parameters are taken into account in those algorithms:

- the phase, defined as the time passed between the start of the acquisition and the maximum of the signal at the output of the shaping signal circuit in the "3in1" card,
- a parameter proportional to the energy deposited into the cells (maximum amplitude), area of peak after the shaping in the "3in1" card.

Some examples of different methods are illustrated below.

3.4.1 Flat Filter

The reconstructed signal R is defined as the sum of the 5 consecutive samples giving the maximum value [18]. The pedestal value, defined as the value measured in the first sample is subtracted at the other samples:

$$R = max \sum_{i=1}^{i+5} (S_i - S_1) \tag{3.2}$$

This method is fast and simple, but it doesn't allow to reconstruct precisely the phase of the signal in a channel.

3.4.2 Fit Filter

This method realizes a fit of the sampled values with a function that represents the expected shape of the signal at the output of the "3in1" card[19]:

$$f(t) = R_{max} \times g(t - \tau) + b \tag{3.3}$$

where $g(t)$is the shape of the normalized signal (fig. 3.5) at the output of the "3in1" card, τ is the phase of the signal, b the pedestal value and $R_{max}$is maximum amplitude.

3.4.3 Optimal filter

This method allows to reconstruct the signal parameters (phase and amplitude) minimizing the effects of the electronic noise. The signal R and the phase τ are expressed as a linear combination of registered values in each one of the n samples S_i[20]:

$$R = \sum_{i=1}^{n} a_i S_i \tag{3.4}$$

$$R \times \tau = \sum_{i=1}^{n} b_i S_i \tag{3.5}$$

the factors $a_i$and $b_i$are parameters depending on the electronic noise and on the signal shape. Those factors must be computed for each channel and their values stored in a database.

3.5 Tilecal calibration systems

In order to calibrate the full read-out path, Tilecal was designed to be calibrated using various systems. Many parameters should be well controlled for achieving a good calibration. The energy reconstruction of hadronic particles and jets that pass in the detector demands the precise measurement of the energy deposited in the calorimeter and also the timing of that deposition. The stability and the linearity of the response should be determined with care for the different regions of the detector. As the final digital signal is a result of successive conversions, the response at each stage should be calibrated. The cell and the PMTs responses as well as the digitizers responses have to be precisely measured. The full calibration process relies on three subsystems:

- Charge injection system,
- Laser
- Cesium source

3.5.1 Charge injection system

One of properties of the "3in1" card is the charge injection system used for the calibration of the electronics. Using a *CANbus* or a *TTC* signal is possible to generate a charge, known with great precision, and inject it into the shaping circuit. The signal that is obtained is reconstructed like a signal coming directly from the photomultipliers (i.e. digitization with the digitizer card, conversion in an optic signal).

With this system we are able to calibrate the response of the electronic chain and to monitor the behavior of this response during the time.

The charge Q is obtained and then injected thanks to a discharge of a capacity C_{inj}. If we take V_i as the initial value of the tension of charge of the

capacity, we can express Q as:

$$Q_{inj} = V_i \times (C_{inj} + C_0) \tag{3.6}$$

where C_0=0.13 pF is the capacity of the injection circuit. Two different values are avaibles for capacity C_{inj}, 5 or 100 pF, in order to test low and high gains respectively. The value of the tension V_i is set by a digital to analog converter (DAC) that has a dynamic of 10 bits; the maximum avaible value is V_{max}=8.192 V and if we express Q_{inj}as a function of the N_{ADC} values of the DAC we obtain:

$$Q_{inj} = \frac{N_{ADC}}{1023} \times V_{max}(C_{inj} + C_0) \tag{3.7}$$

During the calibration process, and using one of the algorithms explained above, the response R of the electronic is measured and reconstructed for different values of the injected charge. With the measure of the parameter $R = f(C_{inj})$ we are able to calculate the conversion factor $k_{ADC \to pC}$ between the response R expressed in ADC counts and the injected charge.

With this tool we can correct also the non-linearity of the electronic for high signal when the electronic circuits are saturated. This correction allows to extend the observable energy range, with a non-linearity of the response lower than 1%.

During the data taking is foreseen also to inject a constant charge in order to monitor the evolution the response of the electronics and to correct in case of drift. Test beam in 2004 show that the conversion factor $k_{ADC \to pC}$ is stable with a precision of 0.1% [21].

In the last year about 99.7% of Tilecal channels have been calibrated with the charge injection system, and we saw that the calibration improves the gain precision of the front-end electronics by 1.6% with 0.7% systematic uncertainty. Stability studies have shown a stability of 0.1% over an year, confirming the results obtained at the test beam.

The main objective has been to prepare for physics data taking by meeting our goal of having a <1% sensitivity. In figure 3.7 is summarized the CIS stability over one year; it is important to notice that the problematic channels are less that 1%, in the plot are represented by the non gaussian tails of the distribution.

3.5.2 Cesium calibration

Tilecal modules were designed to be calibrated with a Cs^{137} source emitting γ of 662 keV. The Cesium source (~10 mCi), which passes through the cells in special pipe, thanks to an hydraulic system (figure 3.8).

The Cesium system has to achieve the following goals:

- Quality control of the coupling between cells and fibers,
- equalization of the cells response,
- monitoring of the cell response in the long period.

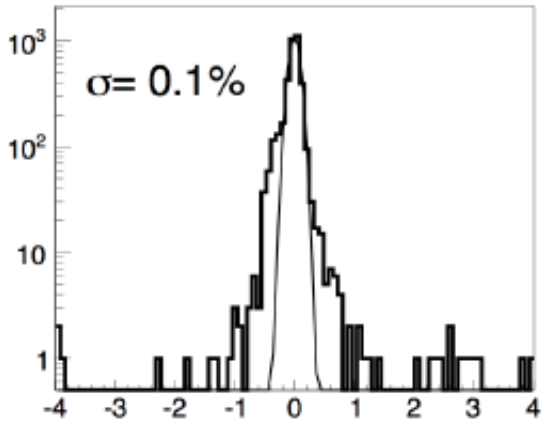


Figure 3.7: CIS stability over 10000 Tilecal channels over one year. The non gaussian tails are due to some problematic channel and it represents <1% of the detector.

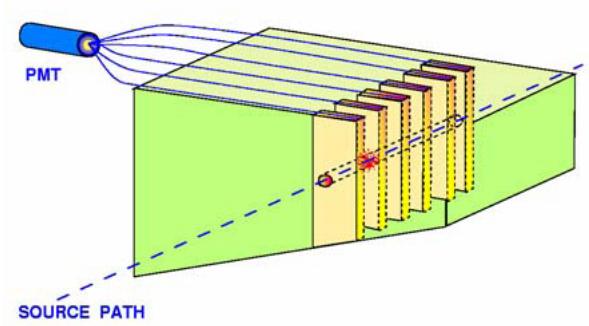


Figure 3.8: Mechanical concept of Cesium calibration system

The final result of this process is the equalization of the cells response with a precision of 1%, see figure 3.9.

Figure 3.10 shows the distribution of the cells gains normalized to 1 for LBA channels. The data was acquired during the summer 2008 after equalization of the HV settings. One can observe that the gains of individual channels can be adjusted to a chosen value with a spread of about 0.3%.

3.5.3 LASER Calibration

The main task of the Laser system is to provide information on the linearity and the stability of TileCal PMTs. Calibrated laser pulses are sent from the Laser box, located in the ATLAS counting room (USA15) to the PMTs through dedicated optical fibers. Thus, the stability and the linearity of the PMTs are

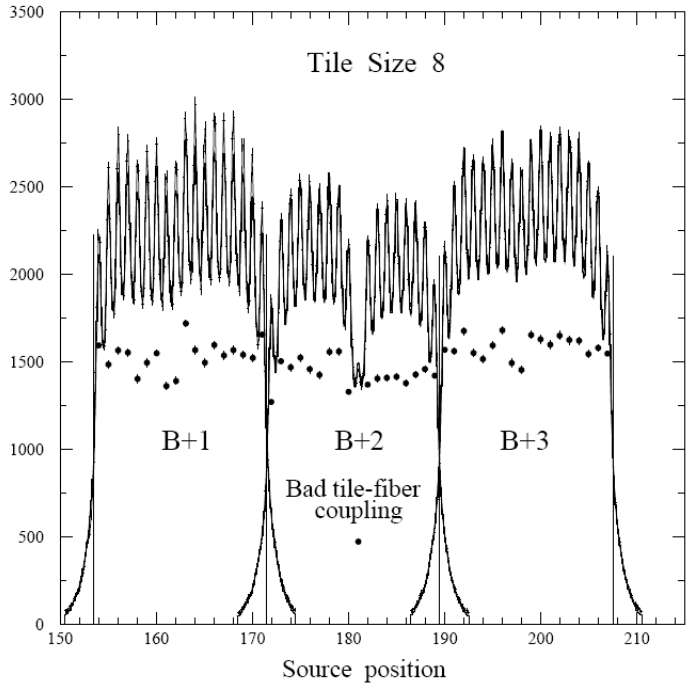


Figure 3.9: PMT response to the Cs source. During the run, the source moves into the cells and generates a signal on the PMTs (top). The cell structure with scintillating tiles and iron plates is visible(bottom).

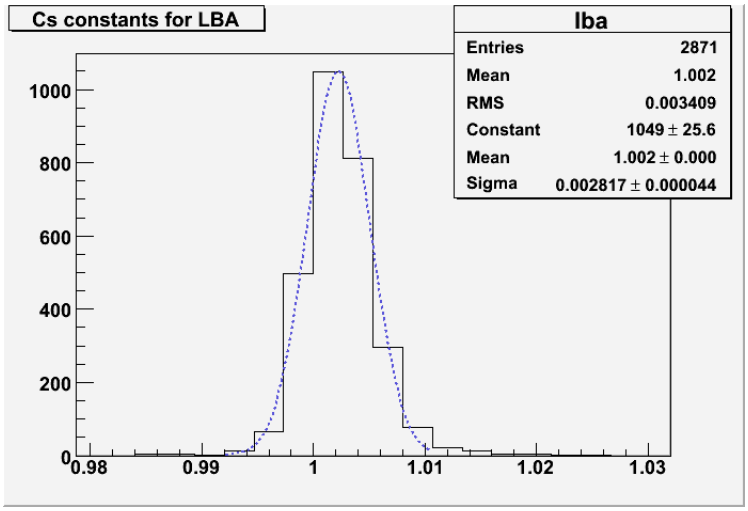


Figure 3.10: Distribution of Cesium constants for LBA channels normalized to 1.

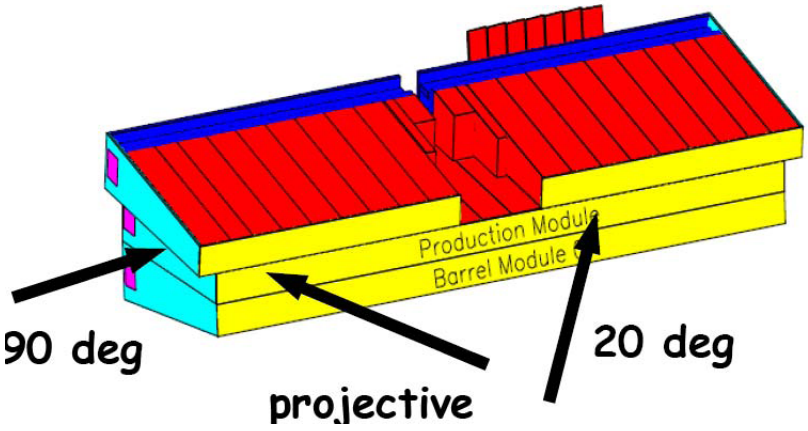


Figure 3.11: Cell response measured with 20°electrons.

monitored. In addition it could be possible comparing the response, to adjust the high voltage settings of the PMTs, providing together with the Cesium system a complete calibration system for the optical part of the detector.

The system will be discussed carefully in the Chapter 4 of this thesis.

3.5.4 Cells electromagnetic scale calibration

After the signal reconstruction operated with one of the algorithm explained above (see paragraph 3.4) we have an energy expressed in ADC counts, then after the charge injection calibration we are able to convert that value in pC. A last conversion must be applied in order to have a scale for the measure of the energy and this scale must be the same for the data and for the Montecarlo. The conversion factor is obtained using data collected at test beam.

The objective of the test beam studies was to understand the response of the detector, to determine its performances and, as said before, to measure the energy to charge conversion. About 12% of TileCal modules have been tested with electron, muon and hadron beams with a momentum ranging from 3 to 250 GeV/c. Modules that were exposed to SPS H8 beam line at CERN.

To determine the electromagnetic (EM) scale, electrons of different energies and at 20°, 90°or projective in η were used. the choice of electrons is justified form the fact that the simulation is more precise.

In particular the conversion factor was obtained using electrons at 20°, that pass through peripheral cells, but this value is valid for all the cells because of the response equalization with Cesium (see figure 3.11). The conversion factor $k_{pC \rightarrow GeV}$was obtained from the the ratio between the response $R_e^{pC}$of the calorimeter and the incident energy of the electron. So now we can define the response $R^{GeV}$of the calorimeter at the EM scale as:

$$R^{GeV} = \frac{R^{pC}}{k_{pC \to GeV}} \tag{3.8}$$

In the follow, and in particular in the chapters 5 and 6, dedicated to the test beam studies, the energy expressed in GeV must interpreted as already calibrated at the EM scale.

Chapter 4

The Tilecal LASER calibration system

In this chapter the LASER monitoring system will be presented. The commissioning and the performances (stability and linearity) will be illustrated with particular attention.

The LASER monitoring system plays an important role in the Tilecal calibration scheme, and in particular in measuring the response of the 9582 PMTs, and the associated electronics, used in the calorimeter.

4.1 The LASER setup

The first proposal for a LASER monitoring system is resumed in [24] where a concept already known in high energy physics experiment ([25, 26, 27]) is used. LASER pulses are similar to a signal produced by a particle crossing the TileCal, but with the difference that the energy of the light pulse initially produced can be known with great precision, better than 1%. This should allow to monitor the PMT gain stability and linearity.

The choice and the conception of the system was done following two main constraints. The first one came from the pulse shape width; in fact it must be of the order of 10 ns. The second one is the need to have a powerful light source able to saturate simultaneously the 9582 TileCal PMT. Following this road map the choice of a commercial Q-switched DPPS (Diode Pumped Solide State) LASER produced by SPECTRA-PHYSICS [28] has been made. This is a frequency-doubled infrared LASER emitting a 532 nm green light beam. This wavelength value is close to the one of the light produced by the physical signals (480 nm). The energy of the pulses delivered by this kind of LASER is few μJ, which is sufficient to saturate all the PMTs, and to test their properties.

The LASER system consists of two main parts:

- the LASER box,
- the Light distribution system.

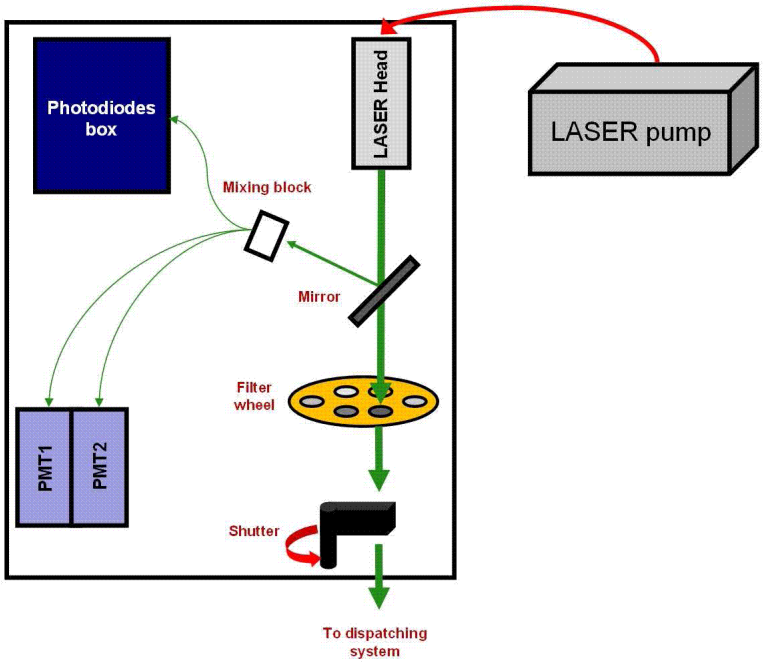


Figure 4.1: In the LASER box, are present also the LASER pump, where the LASER pulse is generated, and the LASER head, where the pulse is sent to the system.

They will be discussed in the following sections.

4.1.1 The LASER box

The LASER box, in figure 4.1, plays a key role in the system architecture. Not only the LASER is contained in the box but also PMTs and photodiodes used for the triggering and monitoring.

Four Si PIN photodiodes, produced by HAMAMATSU [29], are used for the measurement of the light intensity emitted by the LASER, and they are placed in a specific box (figure 4.2) with the associated electronics. The two PMTs placed in the LASER box are used for the LASER pulses timing. The humidity and the temperature in the box are controlled constantly using a dry air system and Peltier elements.

The diodes are calibrated with a source of ^{241}Am[1] that emits alpha particles (see figure 4.2). This calibration is regularly done in specific runs, where the source is placed in front of each diode, for a determined time interval. Outside

[1] The Source activity is 3.7 kBq

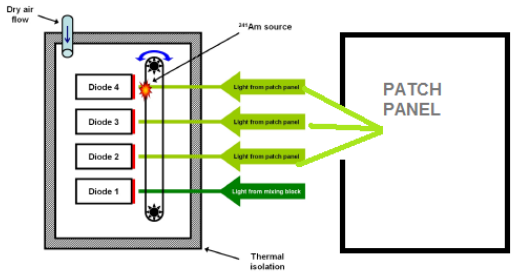


Figure 4.2: The photodiode box

Filter number	1	2	3	4	5	6	7	8
Nominal value	700-1400	80-126	26-38	9-11	1	2.9-3.4	80-126	230-430

Table 4.1: Nominal values for the filters attenuation factors.

acquisition period the source is stored in dedicated garage at the top and at the bottom of the photodiodes box.

Four optic fibers connected to the box dispatch the light to the four diodes; one of the fiber send the light directly coming from the LASER head to one of the diodes and the three others receive the light coming from the Coimbra[2] box (see section 4.1.2). This setup permits to have a constant monitoring on the amount of energy coming from the LASER head and on what is really measured by the TileCal PMTs.

One diode and the two PMTs, placed in the LASER box, receive light thanks to a semi-reflecting mirror, reflecting $8.8\% \pm 0.2\%$ of the light that is sent. The homemade mixing block, is shown in figure 4.3.

The light which is not reflected by the mirror pass through a filter wheel, that is a motorized tool containing eight slots; one of them is empty while in the other seven neutral-density filters providing beam attenuation from a factor 3 to 1000 are placed. In table 4.1 the attenuation factors given by the constructor are given. The measurement of the attenuation factors of the filters must be measured because the nominal value given by the constructor depend from the wavelength of the light, and for that reason it could be different from the nominal value. The results of this measure will be shown in section 4.5.2.2. Their knowledge is important for the determination of the linearity of TileCal photomultipliers.

The last component of the LASER box is an electromechanical shutter

[2]The so called Coimbra box, is a component of the LASER distribution system where the light is disptached to long clear fibers that sent the light in the TileCal PMTs.

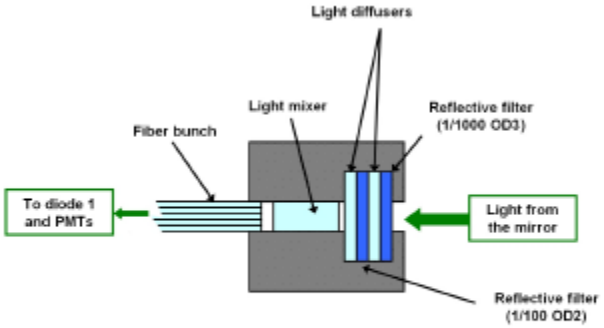


Figure 4.3: The light mixing block in the LASER box

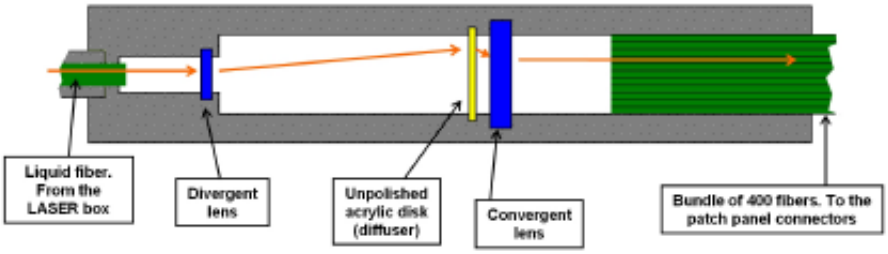


Figure 4.4: The Coimbra box.

installed for safety reasons, and is closed when we don't want that the LASER pulse goes to the calorimeter. As we will see later the LASER can be used in two different ways; in a standalone mode for system intercalibration purpose or in ATLAS mode in order to calibrate Tilecal PMTs.

4.1.2 The distribution system

If a LASER pulse is emitted when the shutter is open the light is collected by liquid fiber [30] that connects the LASER box with the first component of the distribution system, shown in figure 4.4, and known as the Coimbra box.

This box dispatches the primary beam toward a bunch of 400 (384 send the light to TileCal drawers, 16 are used as spares) long clear fibers. This is an optical system based on two lenses that expand the beam diameter. In order to prevent effects related to light coherence, like speckles as we will see later, a

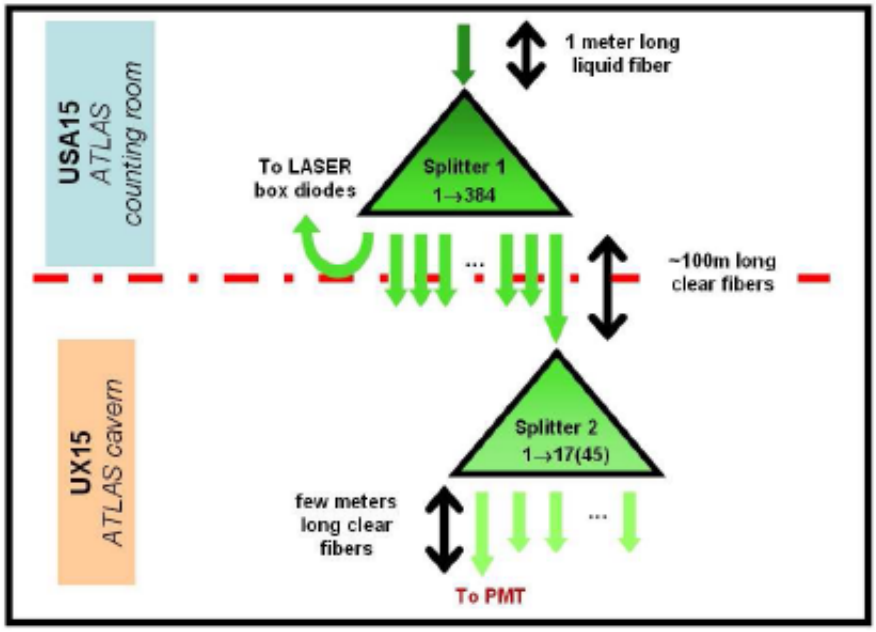


Figure 4.5: The light distribution system

diffuser has been placed in front of the convergent lens. Once that the bundle of fibers reach the patch panel each one of them is glued to an adjustable connector, that joins them to other fibers that go into the calorimeter [26]. The adjustement allows to change the light intensity by changing the distance between the position of the extremes of the two fiber. Using those connectors we equalize the light sent to the TileCal.

The connectors are organized in a patch panel where on the other side long clear fiber (≈100m) transport light to the calorimeter drawers. The 384 fibers are divided as follows: 128 for the two end-cap barrel, 128 for the long barrel. Once in the super-drawer the light is splitted for the last time in order to reach all the PMTs. Each extended barrel modules is fed by two fibers, i.e. 17 PMTs are illuminated by the same fiber. For what concerns the barrel modules, each one is fed by two fibers, i.e. 45 PMTs are illuminated by the same fiber.

Not all the fibers coming from the Coimbra box send the light to the calorimeter, as said in paragraph 4.1.1 some of them send back the light to the LASER box diodes allowing to measure the light collected after the patch panel (Coimbra box). To simplify the linearity tests each one of the three diodes cover a different region of energy in the dynamic range of the TileCal PMTs. For this purpose additional attenuators were put in front of these fibers at the level of the patch panel.

4.2 LASER electronics

The components installed in the LASER box are controlled by an electronic system located in a VME crate outside the LASER box. This crate contains:

- a **VME** processor, on which the low level control software runs,
- an eight channel **ADC** for the laser box photodiodes and PMTs signal digitization,
- a **TDC** for the measurement of the LASER pulses timing,
- **SLAMA,** the core of the system to control the other electronics devices,
- **LILAS II,** this device must achieve two main tasks:
  1. a charge injection system used to test the linearity of the electronics of the photodiodes,
  2. an interface between the **SHAFT** [27] board, that is the Tilecal calibration requests system in charge to generate the three calibration signals of the tilecal detector, and **SLAMA.**
- **LASTROD**[3]**,** this is the LASER system ROD (Read-Out Driver), included in the ATLAS trigger and data acquisition system,
- **CMDMOTOR,** this is the device in charge to control the moving of the components described before, like the radioactive source, the filter wheel and the shaft,
- **LASERSAFETY,** this is a device in charge to control the different environment variables , like temperature, gas flow etc.

Thanks to this electronics architecture the LASER system is a flexible tool able to work in different modes as illustrated in the following section.

4.3 LASER operating modes

The LASER can operate in different modes, related to the task that it has to achieve. A first mode is the system intercalibration and the second mode is the LASER mode, that is used when a LASER pulse is sent to the calorimeter to perform test or realize TileCal PMTs calibration.

[3]This device is independent from the LASER and it can work also when the LASER system is not operational or could be used for other purposes.

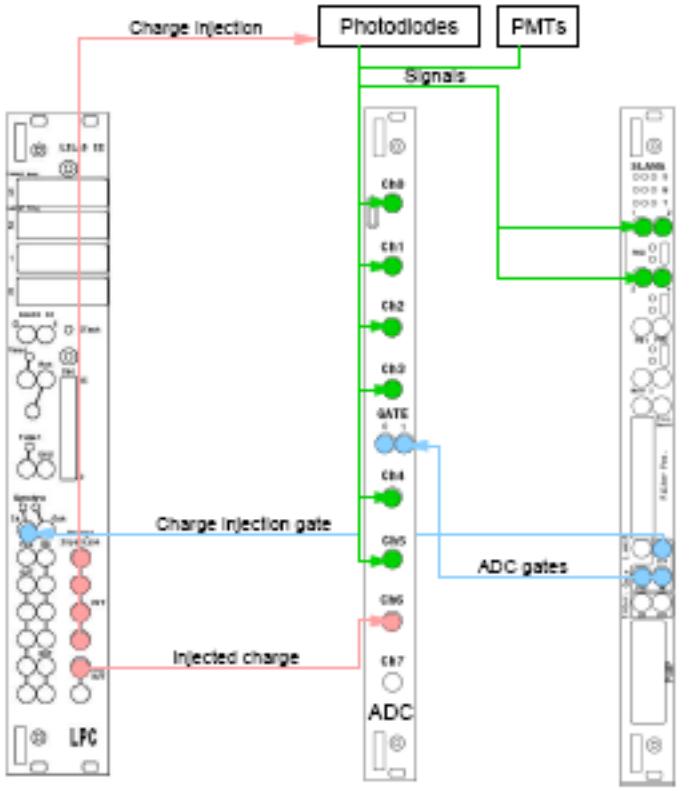


Figure 4.6: LASER system hardware involved in the LASER box calibration. On the left is shown the LILAS II card, on the center the ADC and on the right there is SLAMA.

4.3.1 System intercalibration mode

The aim of this configuration is to perform the calibration and monitoring of the LASER box components, and in particular diodes, PMTs and the associated electronics. When the LASER is running in this configuration there is no light emission. The parameters involved in the LASER box calibration are: the pedestals, the diodes response to the alpha source and the diodes electronics linearity. In figure 4.6 is shown the electronics involved in the system intercalibration operations.

4.3.1.1 Pedestals

When the system is operating in this mode we measure the signals on the photodiodes and the PMTs when no LASER light is sent. The average over all the events is the electronic offset, and the RMS is the electronic noise.

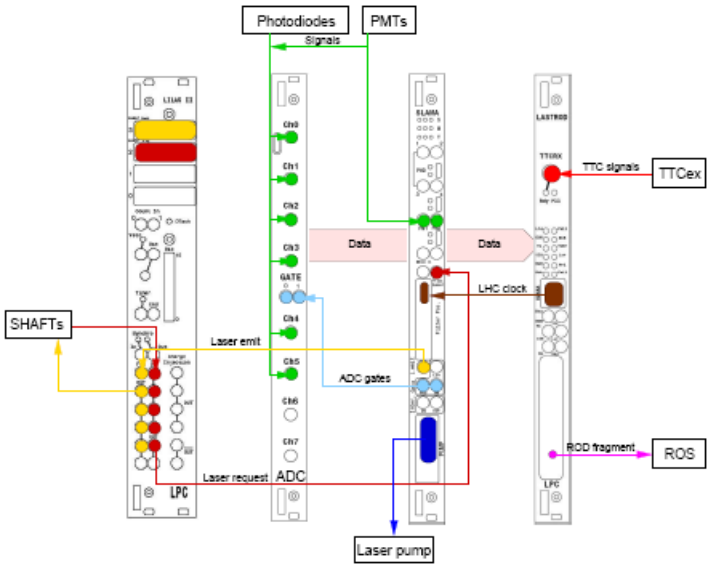


Figure 4.7: LASER system hardware involved in LASER mode. On the left is shown the SHAFT, on the center ADC and on the right the LASTROD.

4.3.1.2 Photodiodes response to an alpha source

In this configuration the embedded alpha source, shown in figure 4.2, is used to test the response of the photodiodes. This source is moved, in front of each photodiode. The signal is fed into SLAMA, where a trigger is generated if is above threshold. In this way for each event only one photodiode contains energy coming from alpha radiation, while the others signals are pedestals.

4.3.1.3 Diodes electronics linearity

This mode allows to measure the linearity of the photodiodes electronics. A known charge is injected in the electronics. The response of the diode electronics and the value of the injected charge is recorded.

A Digital to Analog Converter (DAC) is used to set an electric level from which LILAS II will generate a charge proportional to the DAC level. Once this charge is injected the response of the electronics is digitized by an ADC.

4.3.2 LASER mode

A scheme of the electronic used in this mode is shown in figure 4.7. In this configuration the LASER can work in two different ways:

- in standalone LASER mode in order to test the system and the configuration,

- in the ATLAS configuration to perform the calibration of TileCal photomultipliers and in particular the stability and the linearity of the gain.

The system has been tested during the commissioning period of the LASER system and the results will be shown in section 4.4.

4.4 LASER system commissioning

When the system installation in the pit was completed, a commissioning campaign was performed to check the stability of the different components installed in the LASER box. This campaign was used also to understand the amount of data and the conditions needed to calibrate each component with the requested precision. The main point, for the LASER, is the comparison between the signals obtained in the TileCal PMTs with the signals collected by the photodiodes in the LASER box. It's for that reason that these diodes need to be calibrated with great attention; any lack of information at this stage will be reported into the Tilecal systematic errors.

In particular we have to study three parameters:

- The diodes stability,
- The linearity of the diodes associated electronics,
- The diodes resolution

And in addition to that also the pedestals must be monitored.

4.4.1 Pedestals

The pedestals values of the different channels have been measured during two weeks in March 2008. The main results of that measurement are summarized in figure 4.8.

From this figure we can get different information. The stability of the pedestals values, is shown in the plot on the top left. In bottom left, is shown the relative error on the pedestal defined as the $\frac{\sigma}{mean}$, where σ is the resolution of the pedestal distribution and the mean is the peak obtained from a gaussian fit. On the right is shown, for each ADC channel, the stability of the pedestal measured with respect to the mean pedestal for the channel considered.

From all these plots, we can affirm that pedestals values are stable better than 0.5%, and this is into the limit of 1% imposed by the precision required on the calibration of the PMTs. It has been decided that during the data taking a pedestal value will be measured before each LASER run.

4.4.2 Photodiodes stability (response to the alpha source)

This is another quantity that has been carefully monitored, because it involves the response of the photodiodes that are in charge to measure the LASER light.

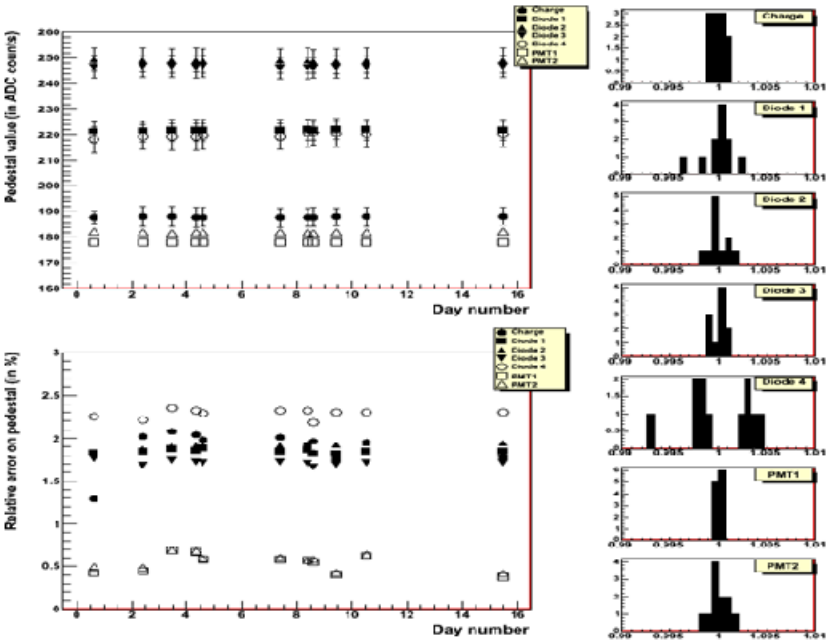


Figure 4.8: Pedestal stability. On the plots on the left is shown on the top the evolution of the pedestal value in the time and on the bottom the evolution of the relative error on the pedestal value. In the plots on the right is shown, for the four photodiodes and for the two photomultipliers in the LASER box, the stability of the pedestal measured w.r.t. the mean pedestal for the channel considered.

It is clear that this monitoring must be independent from the LASER light and it's for that reason that an alpha source has been chosen to do that. As our source is emitting mono-energetic particles, the position of the peak measured by the photodiodes should remain constant along time. If a change in the peak position is observed it means that there is a problem which could come from:

- Electronic of the photodiodes: in this case the problem should be seen also in the linearity run,
- Photodiode itself: in this case we have to control if the photodiodes linearity is correct,
- Change of the humidity value in the box.

Our aim is to have a resolution better than 0.1% on this parameter as required by the limits on the precision of the tilecal PMTs.

First of all we have to chose the best estimator for the photodiodes response stability. We could think that the peak position would be a good candidate,

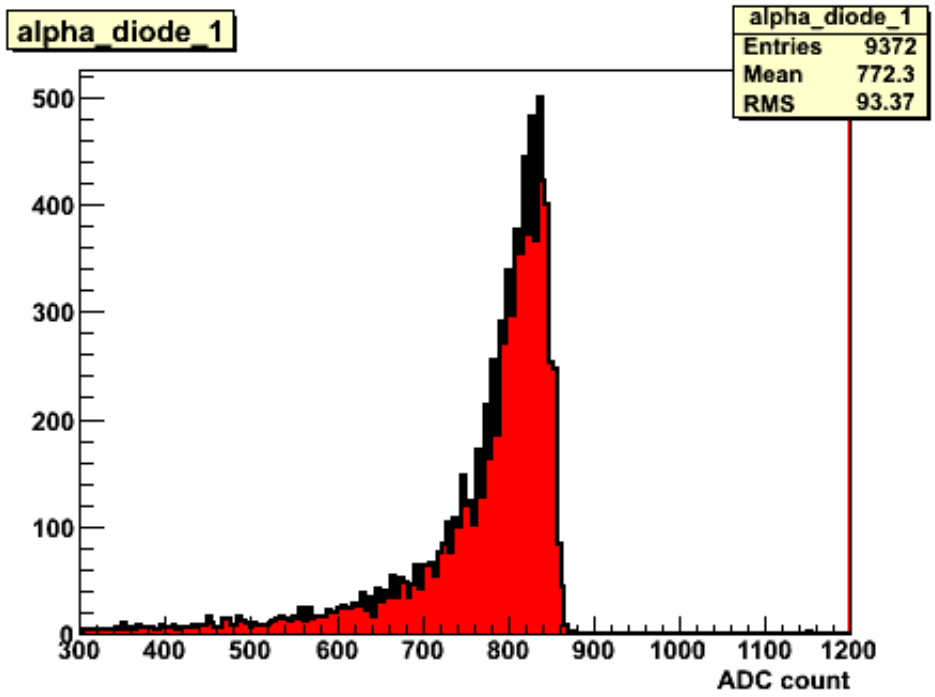


Figure 4.9: A typical alpha spectrum

but if we look at the alpha spectrum, figure 4.9, we see that it won't be easy to extract this value in a sufficient robust way. A gaussian fit also is not the good solution because only the right part of the distribution is gaussian. The shape of the distribution comes from the presence of air between the source and photodiodes that generates the left tail in the distribution.

Finally the mean and the RMS of the distribution of the photodiode response to an α source have been chosen to estimate the stability of the response. The only problem of this choice was related to the large RMS value. We had to verify that the number of events requested to have the error on the mean, defined as $\frac{RMS}{\sqrt{N}}$ where N is the number of events, within our requirements was not to big. But if we assume that the peak value is 1000 ADC counts, the RMS 100 ADC counts and the number of events 10000 we obtain:

$$\Delta E = \frac{10^2}{\sqrt{10^4}} \tag{4.1}$$

where E is the peak value:

$$\frac{\Delta E}{E} = 10^{-3} \times 1 = 10^{-3} \tag{4.2}$$

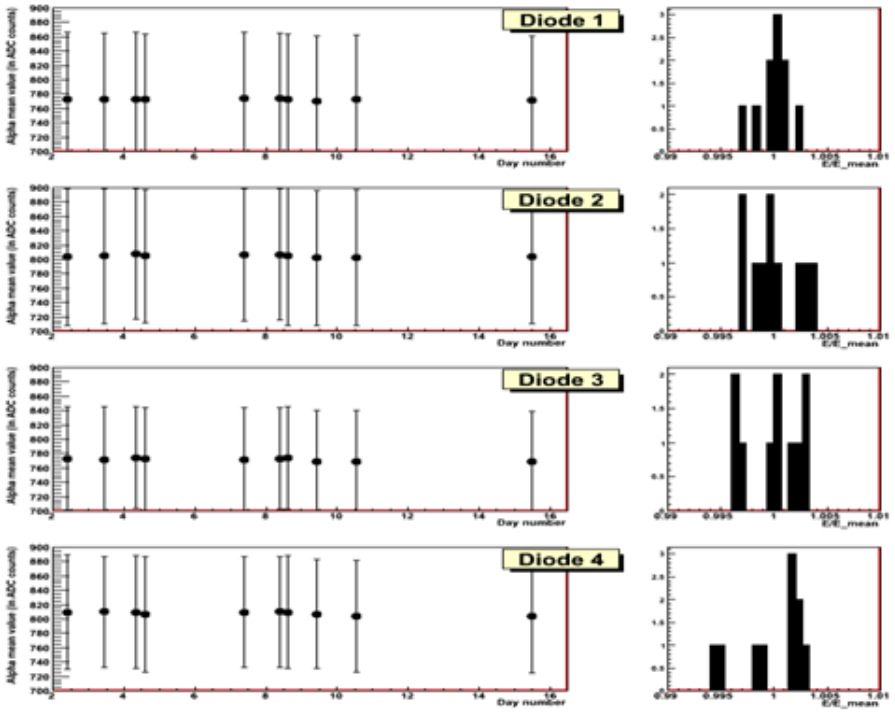


Figure 4.10: Stability of the photodiodes response, the error bars are the RMS values. On the left is shown the stability of the mean of the distributions. On the right is shown the stability of the mean w.r.t. to the mean value of the considered diode.

So the result coming from equation 4.2 demonstrates that with 10000 events, in an ideal situation, we can reach a precision of 0.1% on our measure using the mean and the RMS of the distribution of the photodiode response to an α source as estimator of the response stability.

Figure 4.10 shows the results for the stability of the photodiodes response. In the left column is plotted the mean value of the distribution as a function of the time (the number of days) for the four photodiodes. In the right column is shown, for each photodiode, the stability of the mean value with respect to the mean of the mean values for the considered photodiode.

These results show that the response of the diodes is stable with the time better than 0.5%.

In figure 4.11 are shown the plots obtained for the resolution of the diodes, defined as the ratio RMS/Mean. In the left columns plots the resolution as a function of the the time is shown, while on the right column is shown the resolution value measured with respect to the mean resolution for the considered diode. Those plots tell us that our estimator is robust and allows us to reach

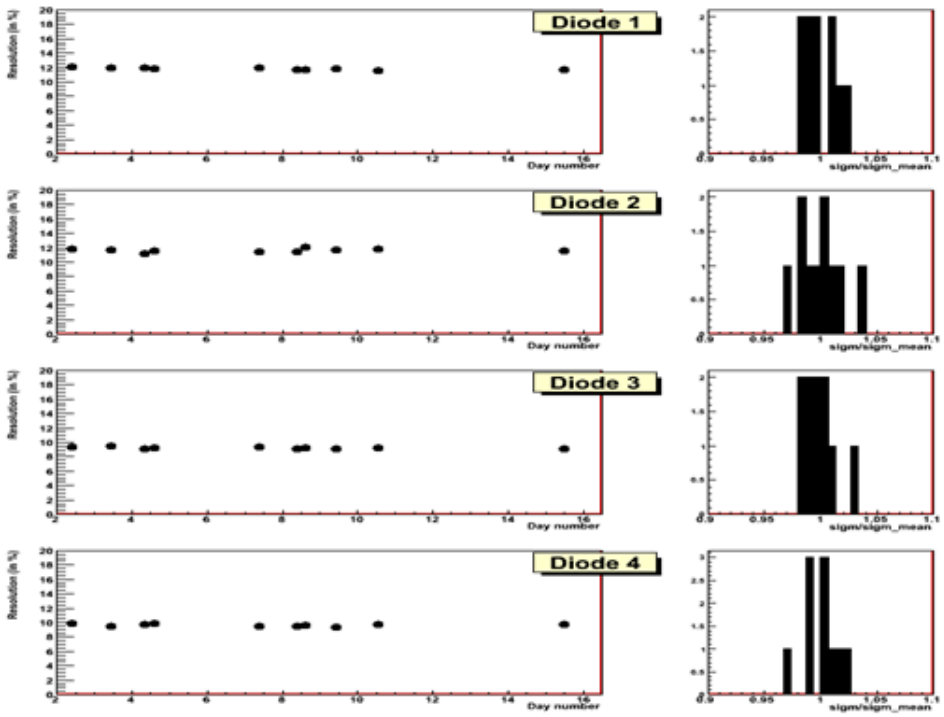


Figure 4.11: RMS/Mean stability distribution. On the left is shown the resolution as a function of the time, on the right is shown the resolution value measured w.r.t. resolution for the considered diode.

the precision of 0.1% on the mean collecting 10000 alpha events. This statistics is easy to obtain, in fact it takes only few minutes of data taking.

4.4.3 Linearity of the photodiodes electronics

The linearity of the electronics associated to the diodes is a crucial point for the comprehension of the system. When we measure the linearity of the PMTs in TileCal we want to be sure that the diodes in the LASER box are linear. We monitor this parameter because the value of the signal from the TileCal PMTs is compared with the signal measured in the diodes. It's clear that if our diodes are not linear the results will be difficult to interpret. The requested value for the linearity of our system is 1%.

The linearity of the diodes is tested with a charge injected in the diode electronics, using the LILAS II card. The injected charge is measured in order to control the linearity of the ADC that we are using.

A linearity run is analyzed as follows: the spectrum obtained is fitted to a polynomial of order 1, the residuals and the chi-square are computed. The

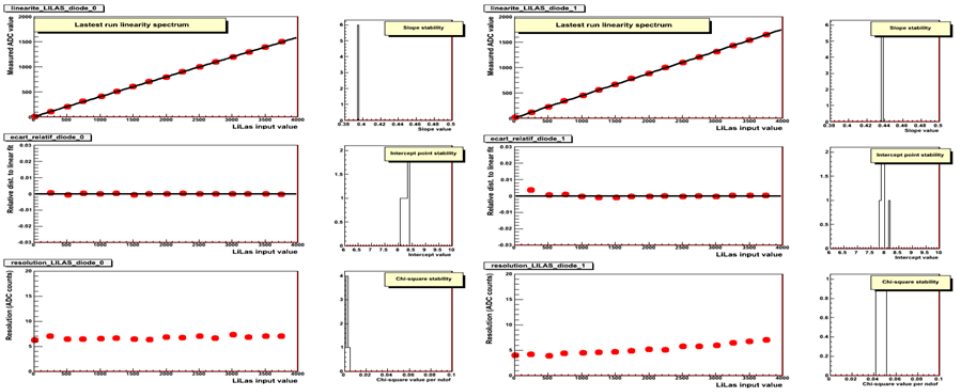


Figure 4.12: Linearity results for the injected charge(left column) and one of the four diodes (right column). For each component is shown on the left the linearity spectrum with the corresponding fitted line (top), the relative distance to the linear fit (middle), and the absolute resolution (bottom). The three plots on the right show, for all the runs, the values of the intercepted slopes and intercept points obtained (top and middle), and the value of the chi-square per degree of freedom (bottom).

results obtained for the charge injected (left column) and one the four diodes (right column) respectively are summarized in figure 4.12. For each of the two components shown there are six plots, on the left are shown the linearity spectrum with the corresponding fitted line (top), the relative distance to the linear fit (middle), and the absolute resolution (bottom). The three plots on the right show, for all the runs taken during the commissioning period, the values of the intercepted slopes and intercept points obtained (top and middle), and the value of the chi-square per degree of freedom (bottom).

Once looked at all these plots is clear that the linearity is within our requirements (1%), and we see that the degradation of the resolution is small ($<$2%) when the injected charge is increasing.

4.5 Tilecal calibration and monitoring with the LASER system

The role of the LASER system in Tilecal can be divided mainly in two part:

- Monitoring, that will be performed both online and offline, using the LASER events taken during the LHC gaps[4],

[4]With LHC gap we define the empty bunches cross during an LHC run. It is in those intervals that calibrations signals will be sent

- Calibration, that will be performed mainly offline using the LASER events taken outside physics run. It's with those events that we will test the PMTs stability and linearity.

The calibration coefficients, that will be used to correct for gain changes between to Cesium calibration runs, will be calculated by dedicated tools in ATHENA, the ATLAS framework, which will provide ROOTtuple containing the coefficients.

4.5.1 Monitoring

As said before the monitoring will be realized both *online* and *offline*.

Online monitoring will consist in real-time following of Tilecal's critical parameters, and it is realized using the events collected in the LHC gaps. These controls are mandatory to ensure a good quality of the recorded data. Concerning the LASER system the parameters which will be monitored online are:

- *The timing of the LASER events,* to check that we are on the middle of the LHC gaps,
- *The mean light amplitude distributed by the patch-panel fibers,* to check that there is no problematic channel/fiber,
- *The ratio* $PMT_{Tile}/PMT_{RefTile}$, this ratio should be constant over time. For this task we don't use the diodes in the LASER box but a photomultiplier of TileCal.

The first point is most critical, in fact a wrong timing in the LASER events will produce fake physics events; is for that reason that an automatic emergency stop has been implemented in the system, and it will start, stopping the LASER pulses, if the LASER event BCID[5] becomes out of it' normal range.

The role of the *offline monitoring* is to check the data and detector integrity. In case of the LASER system this part is very common with the calibration; each time that a new calibration constant is computed one has to verify their validity, so one has to do offline monitoring. This task will be achieved doing the comparison between the data of a run taken during the filling of the machine, and another run taken in the past used as reference.

4.5.2 Calibration

The calibration of the TileCal PMTs with the LASER must cover, as said before, two aspects the stability and the linearity of the gain. Both the aspects have been carefully studied and investigated, and now a procedure to estimate the stability has been establish while for the linearity things are little bit less advanced. Both aspects will be discussed in the following sections.

[5]Bunch Crossing Identifier: it is a number that identifies the type of events during a LHC run

4.5.2.1 Stability

The stability has been the first aspect studied, in fact before to approach the linearity of the PMTs we must be sure to be able to control their stability. Instability in the system or a wrong evaluation of that could affect the linearity itself.

The parameter that defines our stability and that we want to monitor is :

$$\Delta_i^{\frac{n}{n+1}} = \frac{(R_i^{n+1} - R_i^n)}{R_i^n} \tag{4.3}$$

Where i is the number of the photomultiplier taken into account, n is the reference run and n+1 is the last run realized and $R_i$is defined as:

$$R_i = \frac{E_i^{pmt}}{D1} \tag{4.4}$$

where D1 is the signal measured in the diode in the LASER box that receives the light that comes directly from the LASER head and E_i^{pmt} is the signal measured in a TileCal photomultiplier.

A method to determine the stability of the TileCal photomultipliers has been implemented in the official ATLAS software ATHENA. The approach of this method could be defined as iterative. At each stage the correction applied cancels different effects that could affect the system in different moments. Two sources of variation coming from from the LASER has been identified:

1. The first source of variation is an effect due to the filter wheel. We observed for two runs taken with the same filter wheel position but in different period of time a global shift[6] in the calibration constant. We reproduced this effect during a test where two consecutive runs (run 1 and 2) were taken with the filter wheel in the same position, then we we moved the wheel to another position and finally we put it back in the initial position and we take a LASER run again (run3). If the effect is introduced by the movement of the filter wheel we have to see a difference between run 2 and 3 and no difference between run 1 and 2 (figure 4.13). In figure 4.14 top is shown the difference between run 2 and 3, this means that at each time that we change the position of the filter wheel we introduce a global bias in the global amount of light sent in the Coimbra box.

2. The second source of variation in our calibration constants is an effect coming from the Coimbra box. The method used to detect this problem is explained later in this section.

We can express the value of the parameter $\Delta_i^{\frac{n}{n+1}}$ as the same of the different possible source of instability:

[6]For global shift we mean a variation affecting all the TileCal PMTs.

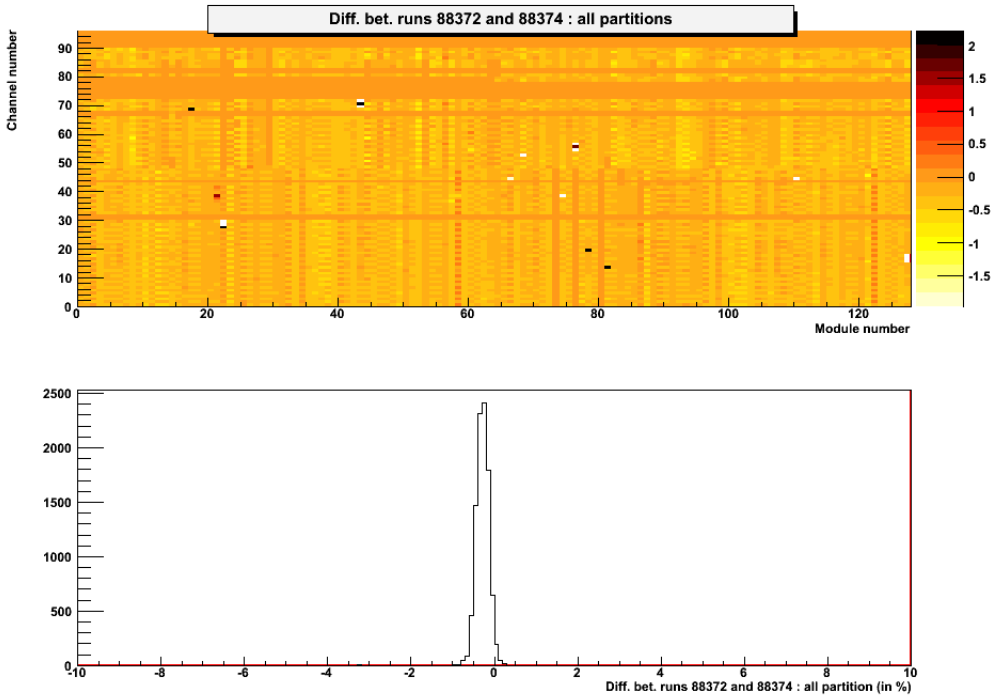


Figure 4.13: Difference between run 1 and 2 obtained for one TileCal module in the test for the filter wheel effect.

$$\Delta_i^{\frac{n}{n+1}} = \Delta_{filter}^{\frac{n}{n+1}} + \Delta_{fiber}^{\frac{n}{n+1}} + \Delta_{pmt}^{\frac{n}{n+1}} \tag{4.5}$$

In order to remove the sources of instability introduced by the LASER system itself we can correct that in the following way:

- get the ratio variation for all the channels just to have the overall variation ($\Delta_i^{\frac{n}{n+1}}$), and the related RMS, due to the filter wheel ($\Delta_{filter}^{\frac{n}{n+1}}$).Some iterations are realized to remove the tail of the distribution,
- the filter wheel correction is applied at all the channels, in order to have the variation and the RMS on the fibers, defined as the variation from the mean value. We do again some iterations to remove the tails of the distribution,
- Now we have removed the variation coming from the fibers ($\Delta_{fiber}^{\frac{n}{n+1}}$) and we can compute the final variation.

Now we can write the expression for the parameter that evaluates the instability on the TileCal photomultipliers, that we define as our final variation, once

Δ_{fiber}	Δ_{filter}
Before correction	
2%	3%
After correction	
<0.5%	<1%

Table 4.2: Evaluation of the different effects affecting the instability of the PMT coming form the LASER box. Before and after that the correction for the fibers and for the filter wheel are applied.

that the sources of instabilities coming from the LASER system are taken into account, as:

$$\Delta_{pmt}^{\frac{n}{n+1}} = \Delta_{i}^{\frac{n}{n+1}} - \Delta_{fiber}^{\frac{n}{n+1}} - \Delta_{filter}^{\frac{n}{n+1}} \tag{4.6}$$

The systematic coming from the effect on the filter wheel (1) can be reduced using one of the diodes receiving the light from the Coimbra box, because they are placed after the filter wheel, instead of the diode that receives the light directly from the LASER head.

The results of the procedure are shown in figure 4.14 and 4.15 top. In table 4.2 are resumed the estimation of the different effects. We can see that the spread on the measure is about 2% for the effect generated by the fiber (2), figure 4.14 top, and we want to understand at which stage this problem appears, in order to reduce the systematics coming from this effects.

A strategy to point out the source of our problem has been established. We decided to realize a method based on hypothesis test of the chi-square. This test will allow to see how is the behavior of real data with respect to a perfect behavior, in particular for our problem an evolution of the ratio PMT/D1 that is constant as function of the time. From a mathematical point of view the chi-square is defined as:

$$\chi^2 = \sum_{i=1}^{k} \left(\frac{x(t_i) - \mu(t_i)}{\sigma(t_i)} \right)^2 \tag{4.7}$$

where:

- $x(t_i)$is the measured value
- $\mu(t_i)$is the value expected from the hypothesis, in our case it is independent from the time
- $\sigma(t_i)$is the error coming from the measure

In the ideal situation the measured values and the ones coming from the hypothesis are compatibles, so the value of the χ^2will be near to zero. The minimal value of function that we will call χ^2_{min}will follow a distribution function

$f(\chi^2_{min})$that will depend on the number of degree of freedom. If our measures confirm the hypothesis the distribution of probability of the χ^2given by:

$$F(\chi^2_{min}) = \int_{\chi^2_{min}}^{\infty} f(\chi^2_{min}) \tag{4.8}$$

must be flat between 0 and 1.

This method has been applied during the analysis of the LASER runs. We did the hypothesis that the distribution of the ratio PMT/D1 must be flat over the time. So we fitted this distribution with a constant line (μ_i=a). Our sample of data was done by runs taken several days at constant rate of 5 Hz.

The results of this first are resumed in figure 4.17, where the distribution of probabilities of the chi-square is shown.

It's clear that our hypothesis test is not verified in fact the probability distribution is not flat and this means that the fluctuation of each point is bigger than the error on the point. To understand the problem we started to see the distribution of the ratio PMTTile/D1. If we look at figure 4.16, we see that this distribution is not flat and in particular at the beginning of the run a strong trend is shown.

To find the origin of this instability the whole LASER box was investigated, and at the end we focused our attention on the optic fibers that dispatch the signal to the PMTs. To verify if the problem is at this stage we measured the signal sent from each fiber; and in particular do that this time we didn't measure the ratio PMTTile/D1 but the ratio between an arbitrary TileCal PMT and all the others installed on the same fiber. The stability test is now applied at the distribution of figure 4.18 where the ratio PMTTile/PMTref as a function of time (seconds) is shown.

From figures 4.18 we see that our hypothesis test is verified under these conditions, in fact the distribution of probability is a flat between zero and one.

The fact that the ratio between two TileCal PMTs of the same fiber is constant as a function of the time shows that a problem is present in the so called Coimbra box; it is here that the light is dispatched on the different fibers that send the light to the TilecCal PMTs. We have an hint that push us to affirm that the repartition of the light is not uniform in the time, and that in particular some speckles problems are present. The speckle[32] effect is a result of the interference of many waves, having different phases, which add together to give a resultant wave whose amplitude, and therefore intensity, varies randomly. They form a pattern of slightly lighter and darker spots, so the illumination of the fibers is not completely uniform. This would not be a problem as we adjust individually the transmission through each fiber. But as this is due to interference effects, any tiny variation changes the speckle pattern and then slightly the light sent to each fiber. The changes with time are due to small vibrations, thermal expansion, changes in pressure and temperature, etc.

So we have modified the Coimbra box, and in particular we put a diffuser

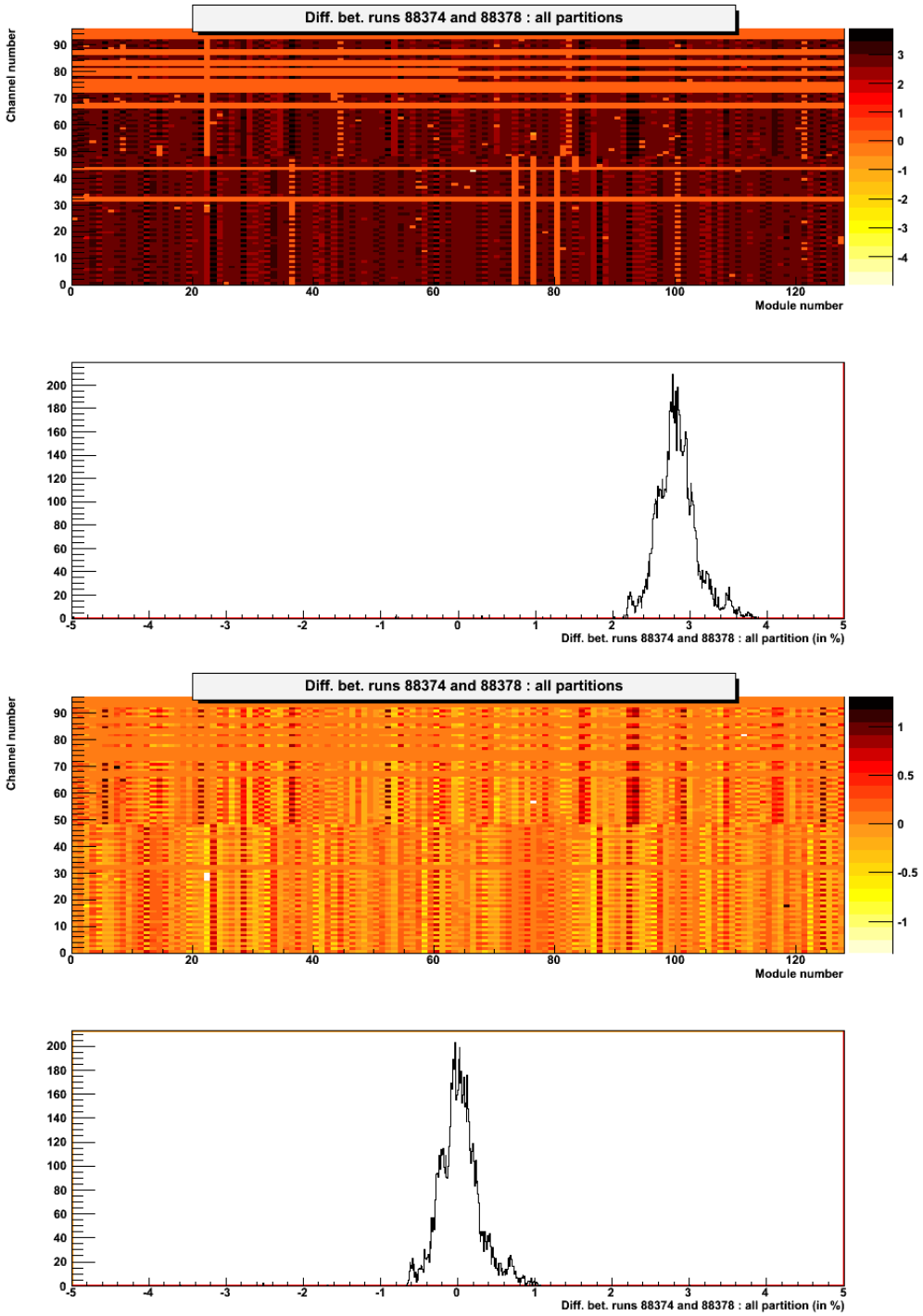


Figure 4.14: Evolution of the parameter $\Delta_{filter}^{\frac{n}{n+1}}$. In the top plot the shift due to the filter wheel is shown. In the bottom plot the result when this effect is removed. The two dimensional plots are a map the amount of light measured in a TileCal partition. On the x axis there is the module number and on y axis there is the photomultipolier number. The spread present here is related to miscalibration of the reference diode.

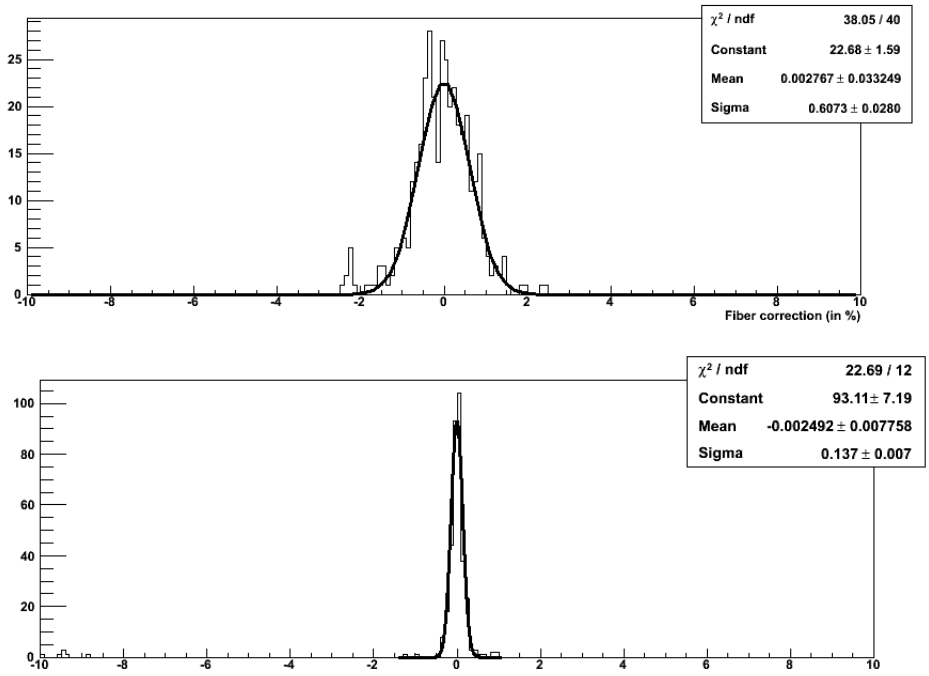


Figure 4.15: Spread of$\Delta_{fiber}^{\frac{n}{n+1}}$. In the top plot is shown the result of the measure before the application of the diffuser. In the bottom plot the same result but after the application of the diffuser.We can see that there is a gain of factor four from the precedent measure.

in the Coimbra box. The modification effected is shown in figure 4.19.

After that modification new data were collected and the same hypothesis test was performed. In figure 4.21, the test results are shown and we can affirm that now TileCal PMTs are stable and so the hypothesis is verified. This means that now the fluctuations as a function of time are compatibles with the errors on the single measures.

In figure 4.15 bottom, we see how this modification change the value of the spread on the $\Delta_{fiber}^{\frac{n}{n+1}}$ that is a factor four better than what measured before. The insertion of the diffuser doesn't has effects on the shift coming the filter wheel; in fact this effect is related to total amount of light sent and not to their fluctuations with the time.

4.5.2.2 Linearity

In this section results of the linearity studied will be presented. The status of this activity is well advanced but not yet finalized; in particular there are some effects affecting our measurements that need more attention.

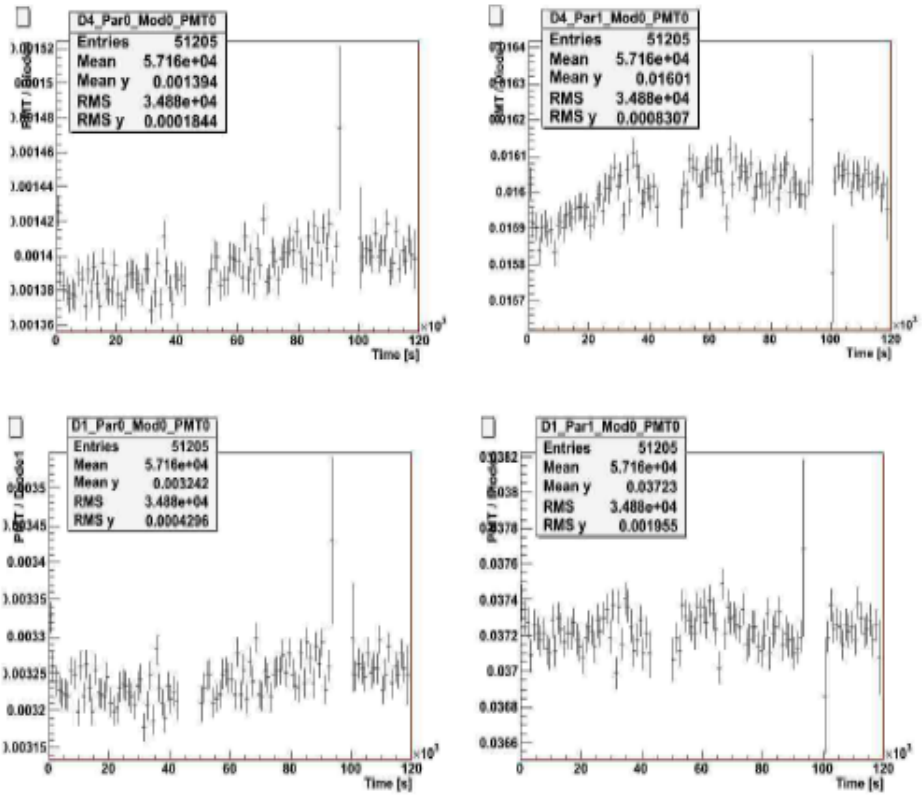


Figure 4.16: Distribution of the ratio PMTTile/D1 as a function of the time (seconds) for two different partitions. The distribution is not flat and a strong trend at the beginning of the run is present.

In this study too the quantity that will be analyzed is still the ratio PMTTile/D1[7] but this time as function of the energy measured in the Tilecal PMTs, and we measure the deviation from a flat line; this deviation gives us the value of an eventual non linearity in the TileCal PMTs dynamic. Some different runs were realized in order to cover the whole TileCal PMTs dynamics using five different filters (2, 3, 5, 6, 8).

Each filter cover a different energy region and they are summarized in table.

Five runs of 20000 for each filter were taken at different energies in order to cover the dynamic of the TileCal PMTs. With this set of data we can cover the region of energy between 80 MeV and 400 GeV, that it doesn't represents the full dynamic but with the present configuration is the maximum that we can perform; in fact it will be necessary to have other photodiodes in

[7] The diode that is used is the Diode 1 that see the light directly coming from the LASER head.

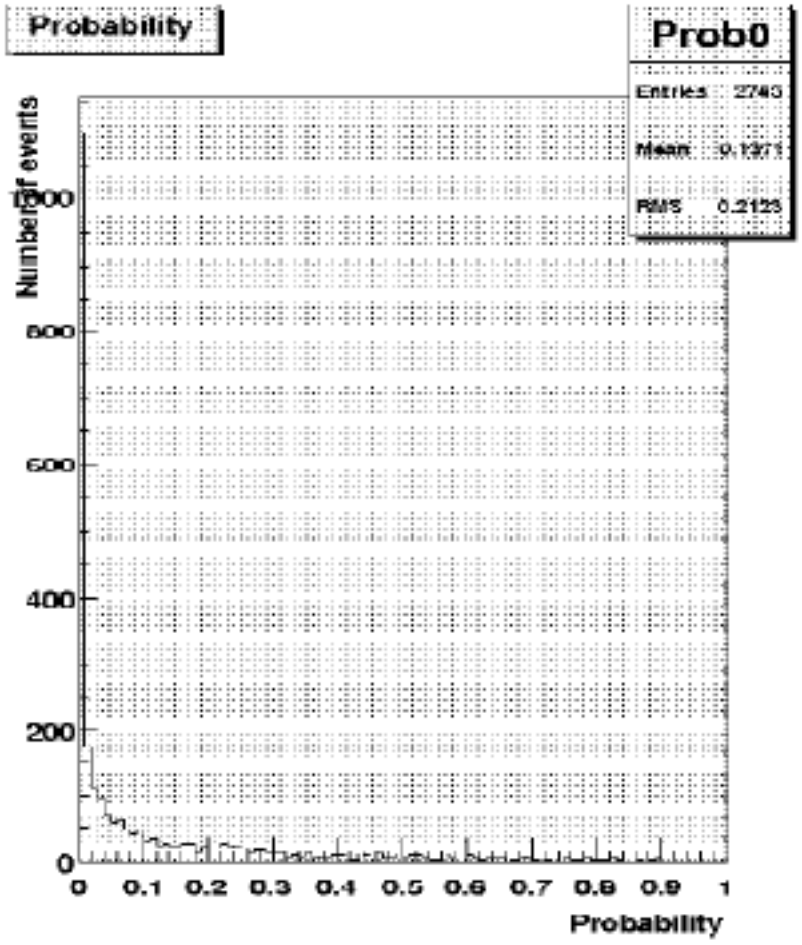


Figure 4.17: Hypothesis test: slopes distribution and chi-square probability distribution. The test is performed on the distribution of the ratio PMTTile/D1 versus the time.

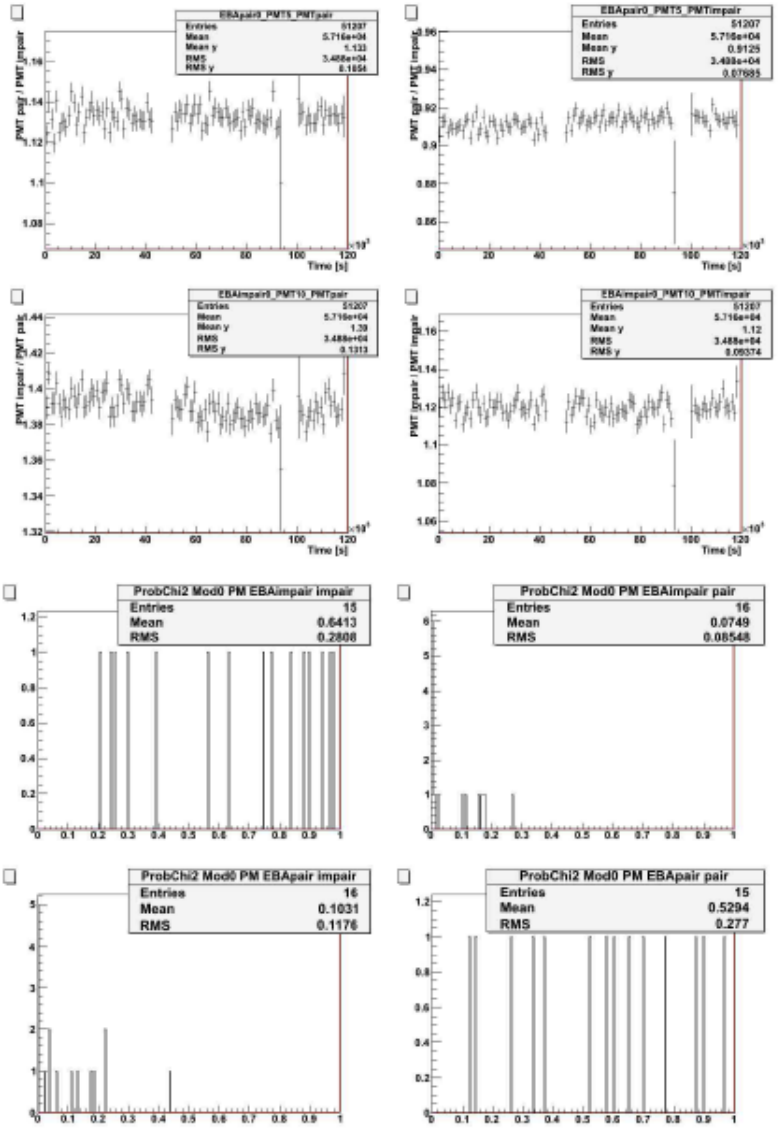


Figure 4.18: Example of the ratio PMT/PMTref for some fiber and distribution of chi-square probability for different fibers in a partition.

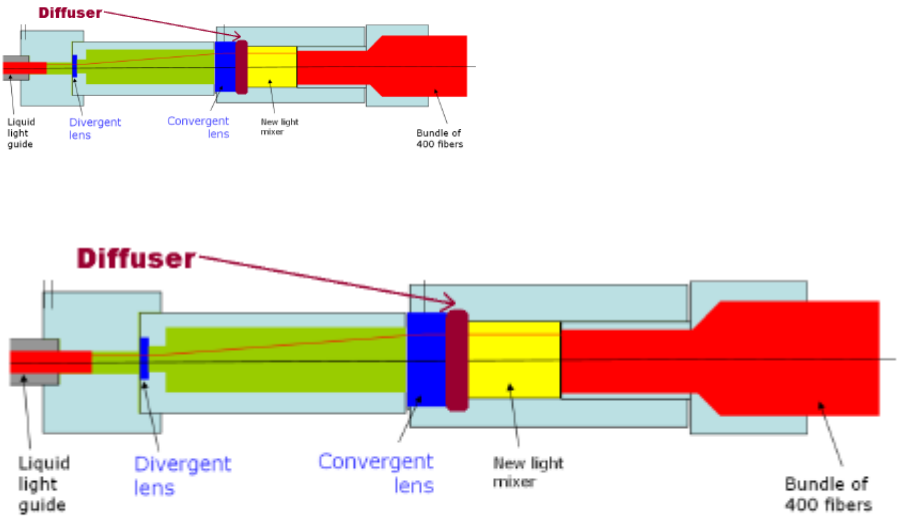


Figure 4.19: Modification in the Coimbra box. On the top before the change, on the bottom after the insertion of the diffuser.

the LASER box to exploit measures with the other three filters, and a more powerful LASER.

The results presented in figure 4.21, show on the x axis the energy measured in one TileCal PMT obtained from a gaussian fit on the energy distribution and on the y axis the ratio between one PMT and one of the diodes in the LASER box, and in particular one where a signal is present.

From those plots we see that the linearity of the PMTs is measured with a variation that goes from 0.08% in the case of low signals to 3.17%, all the values are summarized on table 4.3, where R is the ratio PMT/D1, in the case of biggest signals; only the statistical is calculated and is defined as the sigma of the distribution over the square root of the number of events. These fluctuations at present are not yet understood, but we consider that this isn't an effect of linearity coming from photomultipliers[33] but again an effect introduced by the LASER system itself.

Some points on these distributions where not taken into account because they are obtained using signals that in the diodes are to smallof the same order of magnitude than the pedestals (~100 ADC counts). This means that the signal registered on the diode is a quantity to measure with the maximum care; in fact a wrong or imperfect measure at this stage could introduce a systematic effect on the final measure.

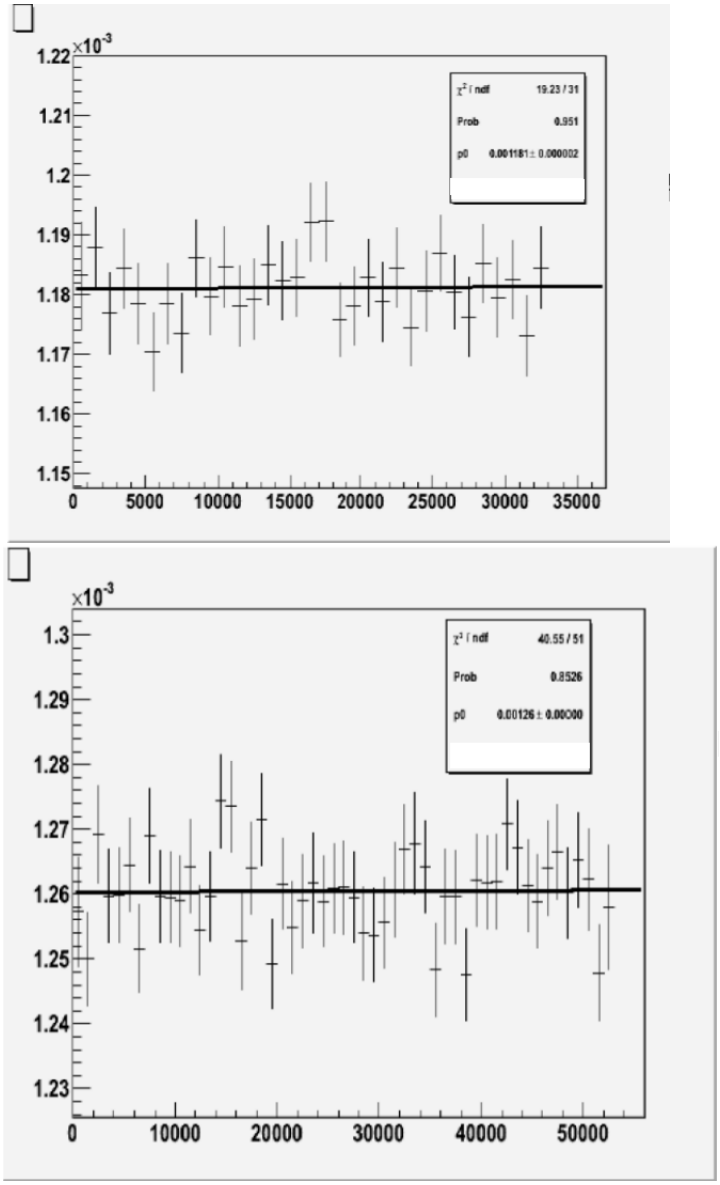


Figure 4.20: Ratio PMTTile/D1 as a function of the time after the insertion of the diffuser.

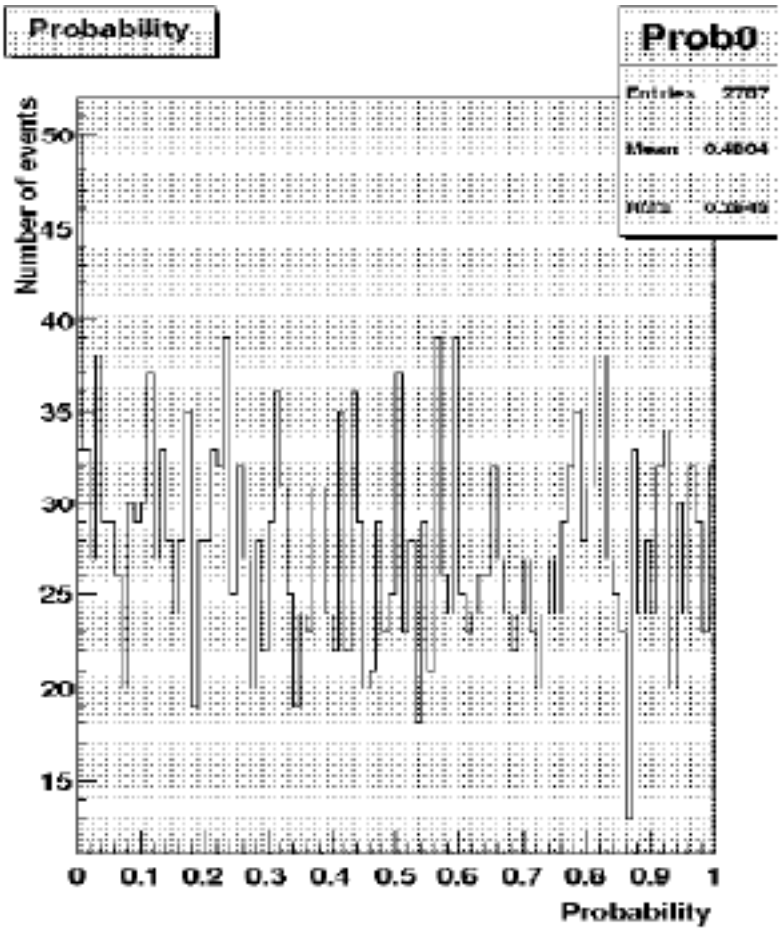


Figure 4.21: Probability distribution after the insertion of the diffuser.

Filter	$\frac{R_{max}-R_{min}}{R_{max}+R_{min}}$
2	0.8%
3	0.4%
5	2.34%
6	3.17%
8	0.08%

Table 4.3: Variation for each filter, where R is the ratio PMT/D1. This value are obtained from the points in the plot in figure 4.21 and 4.22.

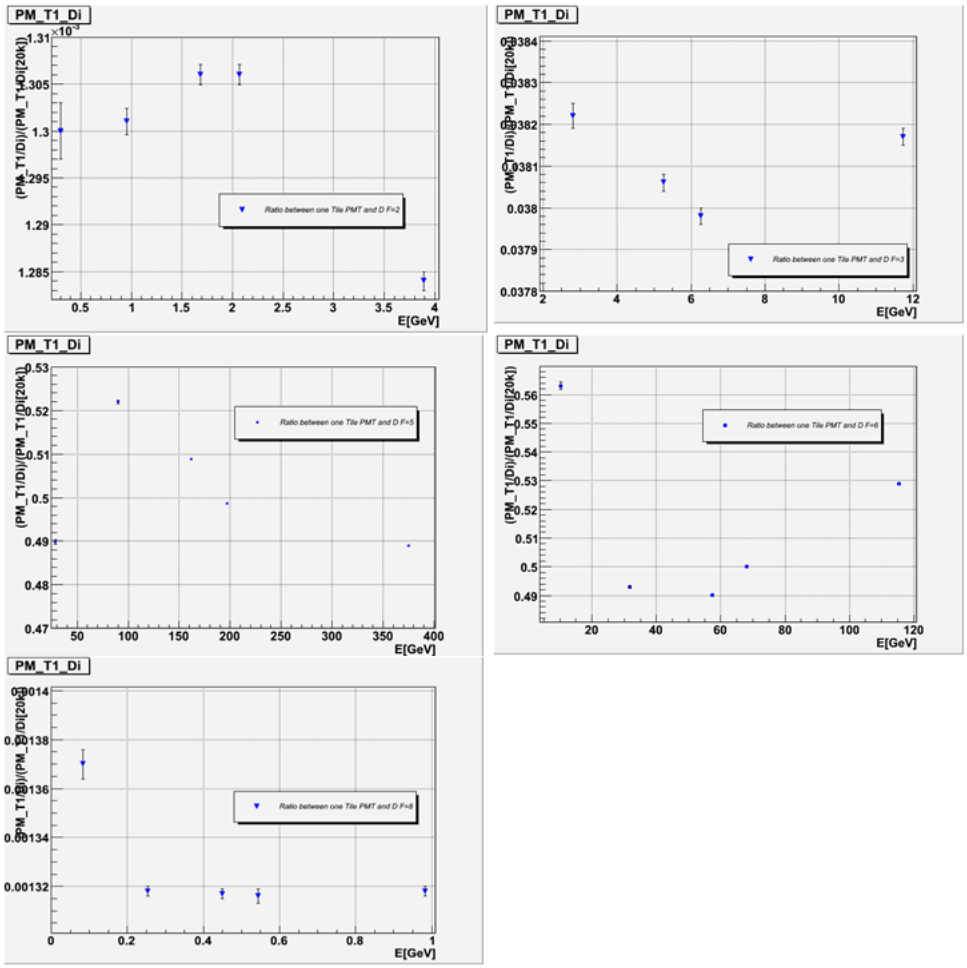


Figure 4.22: Linearity plots for filters 2, 3,5, 6, 8

Filter number	2	3	5	6	8
Nominal value	80-126	28-36	1	2.9-3.4	230-430
Measured Value	94.095±0.037	31.027±0.043	1	3.302 ± 0.810^{-3}	367.089±0.412
Energy range (GeV)	0.4-4	3-12	80-370	10-115	0.1-1

Table 4.4: Measured and nominal filter attenuation factors. The energy range covered by each of them is also shown.

Right now we are not able to cover the full dynamic of the photomultipliers, because of the limited number of photodiodes avaibles in the LASER box. As we have seen the measure strongly depends on those components; it will be good to have a bigger number of that in order to have a signal that is big enough to not be affected by the electronic noise but at the same time that not saturates the ADC. For the LASER upgrade is foreseen to install further photodiodes in the LASER box.

When the source of the non linearity will be understood, the next step in the determination of the linearity of the photomultipliers will be to put the measures obtained for different filters in a unique plot of the same type that has been shown 4.21. To do that we have to measure the attenuation factor of each filter.

To measure the attenuation factors we use the photodiode that receives the light directly coming from the LASER head, and in particular we do the distribution of the ratio $\frac{Diode_1}{Diode_i}$, see figure ,where the $Diode_1$is the diode that sees the LASER light coming directly from the LASER head and the $Diode_i$where *i=2, 3, 4* is one of the diodes that measure the intensity of the light really sent to the tilecal. We fit this plot with a gaussian distribution and the peak value will be the real attenuation factor.

The values obtained are normalized to the value of the filter 5, that has a nominal value of 1 (no filter at that position of the wheel). This different attenuation values where chosen to provide a full coverage of the Tilecal dynamics, from few hundred MeV to 1-2 TeV. The results are resumed in table 4.4.

4.6 Conclusions

We have shown that the LASER system is a reliable tool for what concern the calibration of the Tilecal PMTs. The commissioning has demonstrate that the LASER box parameter are under control and that all the tools installed for the intercalibration are working. The procedure to control the stability of the PMTs is now established and flexible and we are in condition to use that in different situation. The stability of the gain is measured with a precision fo 1%. The work on linearity is ongoing and right now we can perform the linearity studies on a great part of Tilecal PMTs dynamic, and we pointed out some modification at the system in order to increase and simplify the measures on that subject. At present we are able to measure the linearity with a precision

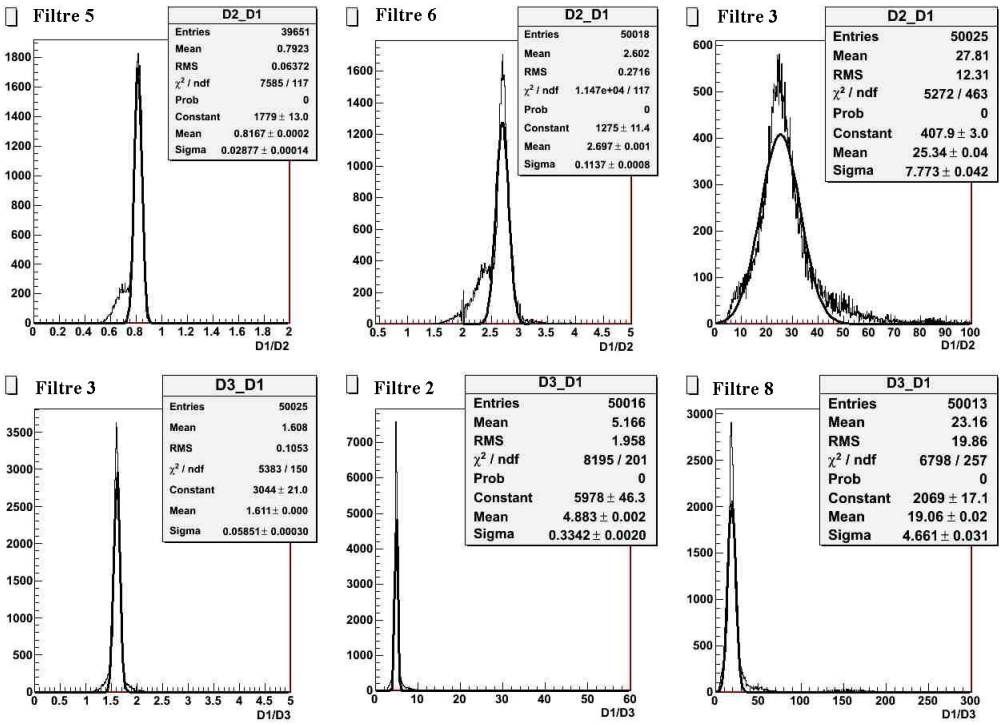


Figure 4.23: Reference histograms for the filter attenuation measure.

that varies between 0.08%, at lower energy value, and 3% at high energy value. The measure is realized on the half of the TileCal (100 MeV-400 GeV).

With all those elements a calibration strategy can be pointed out. The calibration will be realized in two different ways, during the LHC run using the gap between two bunch crossing, and during the fill of the LHC.

During the LHC fill the calibration will be more accurate, and it will be realized in the following way:

1. Calibration of the LASER box
   a) pedestals
   b) alpha run
   c) diode linearity
2. Stability run
3. Linearity run, less frequent than the stability
4. If some difference appears:

a) computation of the new calibration constants

This procedure is the proof that the LASER system is exploitable by the ATLAS experience.

Chapter 5

ATLAS calorimeters response to high energy pions

In 2004 the ATLAS combined test beam took place on the H8 beam line of EHN1. This was the first time that all subdetectors of ATLAS were tested together. Most of them were in the final production version. The main purpose and motivation of this test beam are summarized below:

- Combined reconstruction of muons, electrons and pions using the information coming from the inner detector, the combined calorimetry system, and the muon spectrometer,
- Test of the reconstruction and simulation software and tuning of the Monte Carlo to the test beam data,
- Classical studies concerning the performances of the subdetectors, like linearity and uniformity versus energy and eta as well as energy and resolution studies.

This chapter will start with the description of the H8 beam in order to understand how pions are produced and which the possible sources of contamination are. It continues with the description of the ATLAS setup in H8. After the description of the energy reconstruction methods used in the LAr and in Tilecal, we present the selection cuts applied to have a pure pion sample. Finally, the result of the analysis of the response of the ATLAS central calorimeters to high energy pions are presented.

5.1 H8 beam line

5.1.1 Primary beam coming from the SPS accelerator

The beam used in 2004 is a secondary beam produced from the 400 GeV/c proton beam coming from the SPS accelerator. The primary beam is extracted and sent onto three different targets, T2, T4, and T6. The secondary beam

coming from the target T4 is send down to the H8 line, where the ATLAS subdetectors are installed. The particles, pions, muons and electrons, produced in the collision of the beam onto T4, have energies between 10 and 350 GeV/c.

About 40% of the protons present in the primary beam do not interact in the target and contaminate the beam.

5.1.2 Secondary high energy beam

The momentum selection of the particles is done using a combination of dipole magnets and collimators (C3, C6, C9) limiting the angular spread of the beam. In figure 5.1 is shown the instrumentation of the beam line from T4 down to the last collimator C9. In addition, the pion content of the sample is enriched by using a lead absorber of 1 or 2 X_0, depending the run conditions. This is useful to reduce electron contamination in the beam.

5.1.3 Tertiary high energy beam

An addition beam configuration has also beam used during that period. This tertiary beam was produced by using a polyethylene target (see figure 5.2). This tertiary beam is composed of positive pions with energies between 20 and 180 GeV. Electrons are eliminated by a lead absorber.

5.2 The ATLAS detector at 2004 combined test beam

On figure 5.3 are shown the different subdetector installed in 2004 in the H8 beam line. The following detectors were part of the data taking campaign:

- the inner detector (ID), Pixel, SCT and TRT
- the calorimeters, Liquid Argon and TileCal
- the muon spectrometer.

In addition to the ATLAS subdetectors just mentioned, some more detectors are used for the trigger and for the measurement of the beam position.

5.2.1 H8 beam line instrumentation

The H8 beam line is equipped with scintillators, wire chambers and a Cerenkov counter. Figure 5.4 are shown the position of the different detectors on the beam line.

Wire chambers Five wire chambers, denoted from BC-2 to BC2, are installed in the beam line. These chambers have an active surface of 11x11 $cm^2$and a spatial resolution of about 200 μm.

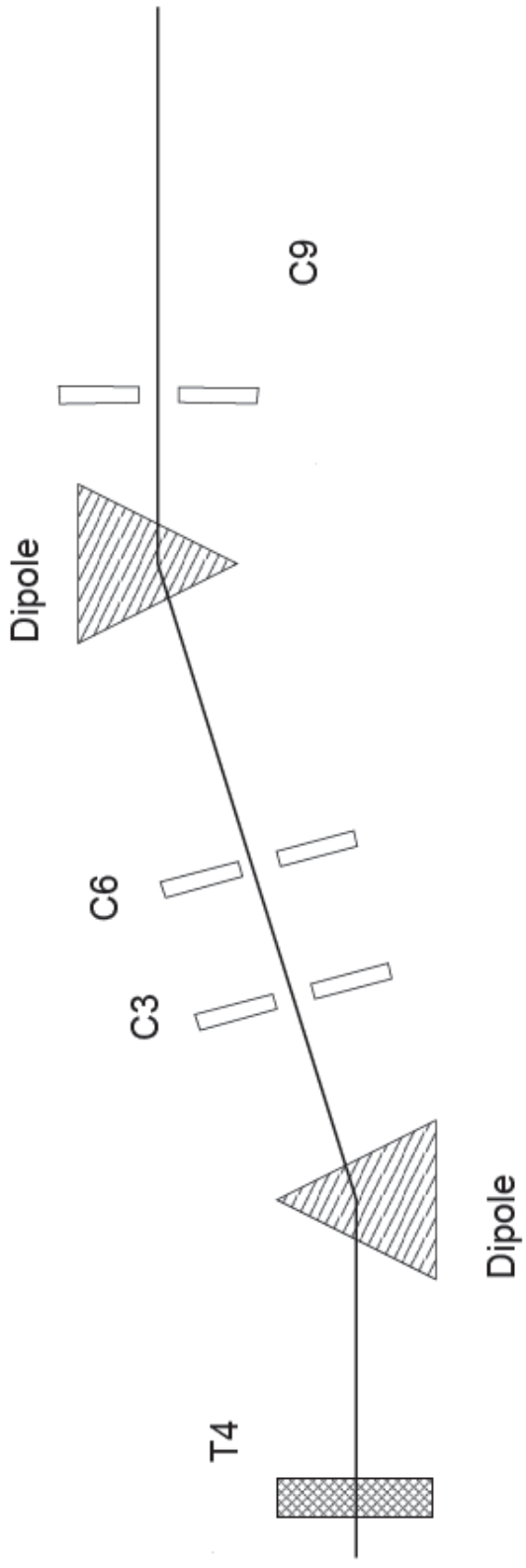


Figure 5.1: Production of a high energy secondary beam.

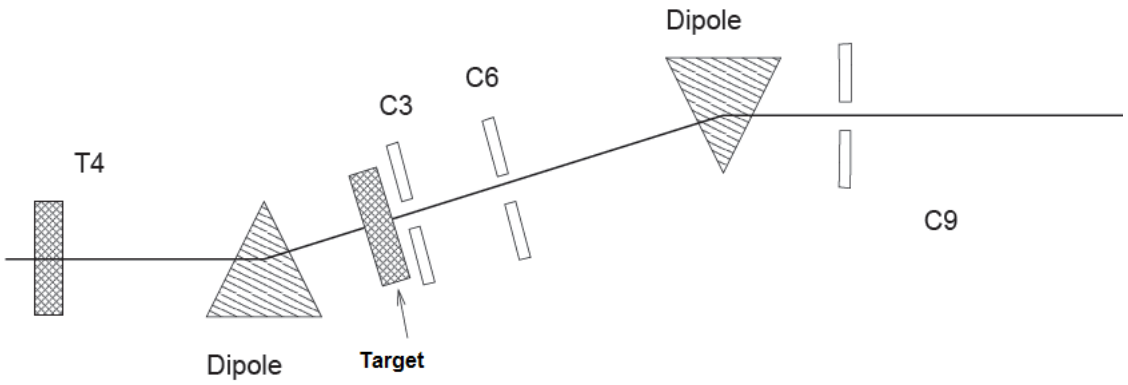


Figure 5.2: Production of a high energy tertiary beam.

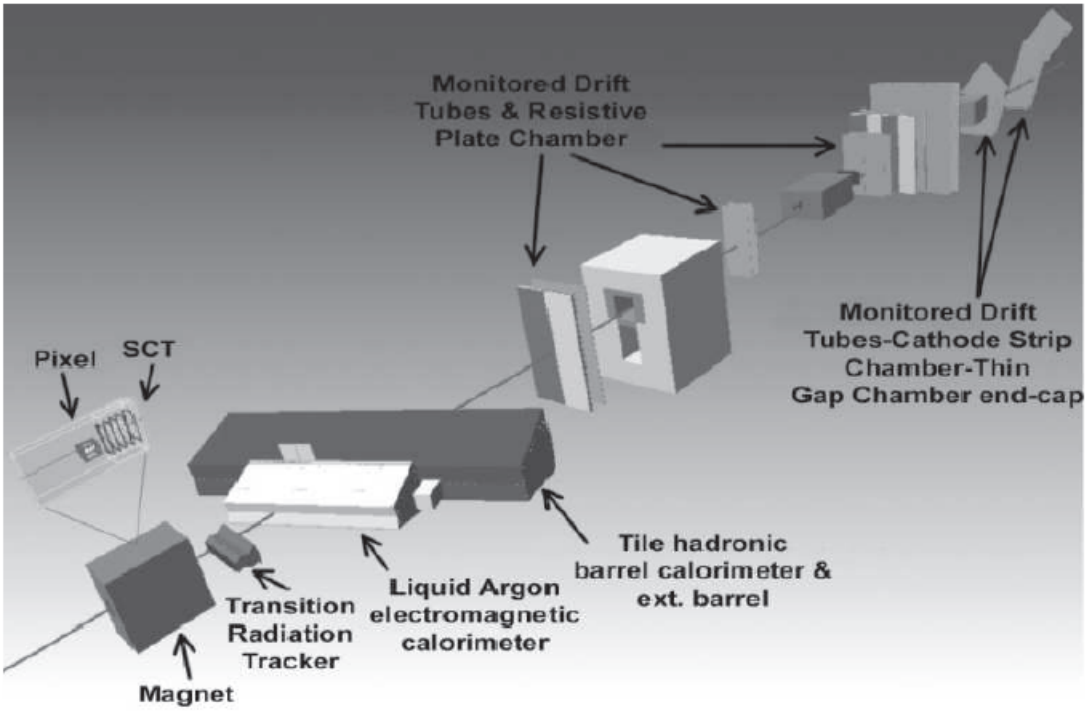


Figure 5.3: ATLAS subdetectors installed for in 2004 test beam.

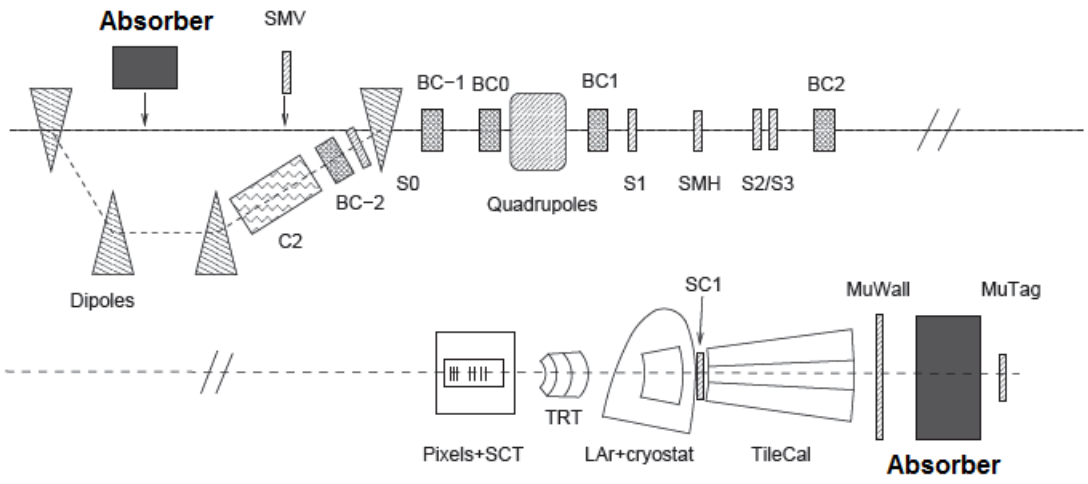


Figure 5.4: H8 beam line instrumentation

Scintillators Nine scintillators are placed in the beam line and their characteristics are summarized below:

- *SMV (Muon Veto):* of muons coming from the high energy beam. It is located off the beam line, in direct view of T4. It is used for low energy analysis.
- *S0:* it is used for the beam quality control. The dimensions are 10x10x0.6 cm^3(height, width and thickness respectively) . Not used in this analysis,
- *S1, S2, S3:* used for the quality control of the beam. In multiple coincidence they give the trigger to the DAQ system. The dimensions of S1 is 10x10x0.6 cm^3while the dimensions for S2 and S3 are 5x5x1 cm^3,
- *SMH (Muon Halo):* this is a big scintillator used to detect the presence of muons in the beam halo. This scintillator is not used because of alignment problems,
- *SC1 (Cryostat):* it is placed behind the cryostat housing the electromagnetic calorimeter and before the first sample of Tilecal. This scintillator allows the study of the hadronic showers. Not used in this analysis,
- *MuTag:* this scintillator (40x40x2 cm^3) is placed after an absorber which stops pions in the beams; it detects mostly muons. This is used in the analysis to reject muons,
- *MuWall:* this is a wall made of 12 scintillators divided in two samples placed 1.5m after Tilecal. Not used in this analysis.

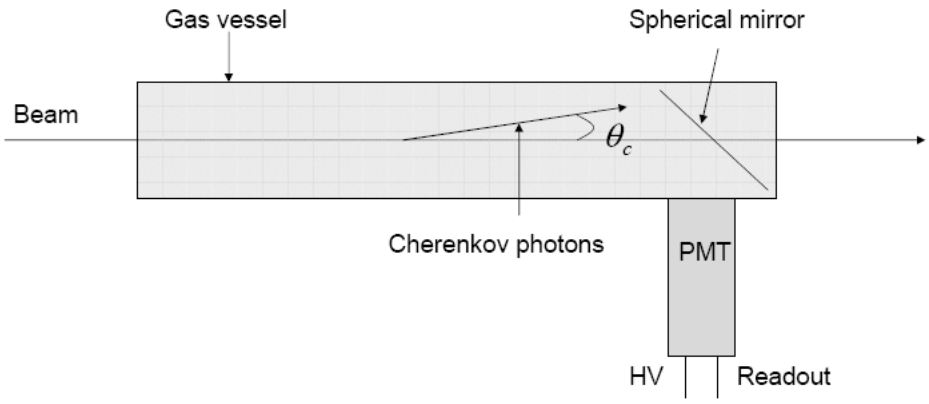


Figure 5.5: Simplified schema of a Cerenkov counter. The particles enter from the left.

Cerenkov counter The basic principle of a Cerenkov detector is quite simple. They are usually filled with a gas. When a particle travels through the gas it produces a wave of polarized molecules along its path. When the molecules depolarize they emit radiations in all directions. If particles travel faster than the speed of the light in the media the emitted radiations become coherent in a certain direction (forward); the result is a significant amount of light produced. This effect will give rise to circular wave fronts. In figure 5.5 is shown a simplified picture of the Cerenkov counter.

If $v > c/n$, Cerenkov light is emitted with an angle $\theta_c$between the emitted photon and the direction of the incoming. It is given by:

$$cos\theta_c = \frac{1}{n\beta} \tag{5.1}$$

Light is then collected by a photomultiplier; the number of photons N is equal to:

$$N \simeq ALsin^2\theta_c \tag{5.2}$$

where A is a constant which depends on the quantum efficiency, and L is the length of the detector. For a given momentum of the particles, $\beta = \sqrt{1 - m^2c^2/p^2}$ and consequently ϑ_c depend only from the mass of the particle. If the mass of two particles is sufficiently different it is possible to identify them using the signal on the photomultipliers.

The Cerenkov counter C2 is installed on the low energy beam line to separate electrons from pions.

More information about this detector can be found in reference [31].

5.2.2 The inner detector

In the following we are going to describe very rapidly the three components of the Inner Detector System:

- the *SCT, Semi Conductor Tracker,*
- the *Pixels,*
- the *TRT, Transition Radiation Tracker.*

The Pixel detector is composed of 6 modules divided into 3 samples placed along the beam line. Contrary to ATLAS where in the final configuration the modules have angle of 20° with respect to horizontal, here they are vertical. Each module cover a surface of 60.8x16.4 mm^2in the $z \times y$ plane.

The SCT is placed after the Pixel detector and is made of 6 planes with 2 modules each. The surface covered by this detector is 120x60 mm^2 and there is a 4mm overlap between the upper and lower samples. In figure 5.6 is shown the pixel and SCT detectors in the beam line.

To reproduce the magnetic environment of the ATLAS experiment the Pixel and SCT are located inside a magnet [31]. The nominal magnetic field is of 2T; it is used to study the performances of the tracking devices. All the data taken for the present analysis were recorded without magnetic field.

Outside the magnetic field area is the TRT; it is composed by two modules of the central barrel, as shown in 5.7. Some more information about the TRT system can be found in the following chapter where it is used to select low energy pions.

5.2.3 Calorimeters

The calorimeter modules exposed at test beam in 2004 were respectively 1 module of the LAr central barrel and three modules of the hadronic calorimeter barrel as shown in figure 5.8. The whole system is placed on a moving table which allows to change the incident angle of the particles between -1 and 1 in eta and -0.2 and 0.2 in PHI. The different orientation accessible are resumed in figure 5.9, and given in unity of eta. The moveable table permits to put the calorimeters in a position so that the incoming particles are projective in η as it will happen in ATLAS.

5.2.3.1 The electromagnetic calorimeter LAr

The LAr calorimeter is placed in a cryostat, as shown in figure 5.10. Table 5.1 summarizes various parameters (angular coverage, granularity and thicknesses) for the two calorimeters exposed to the test beam.

The energy of the incident particle is reconstructed using the OFC method (see chapter 3). For each event, this method gives the energy, calibrated at the electromagnetic scale (see chapter 3), deposited in each cell. The total energy is the sum of the energy deposited in each cell. In order to limit the electronic

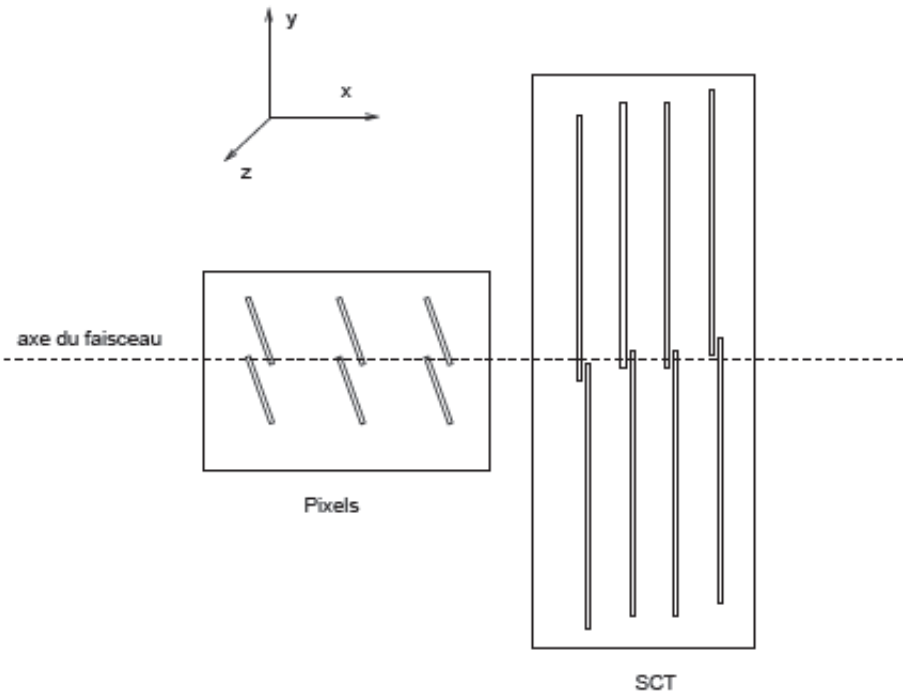


Figure 5.6: SCT and pixel modules at 2004 combined test beam.

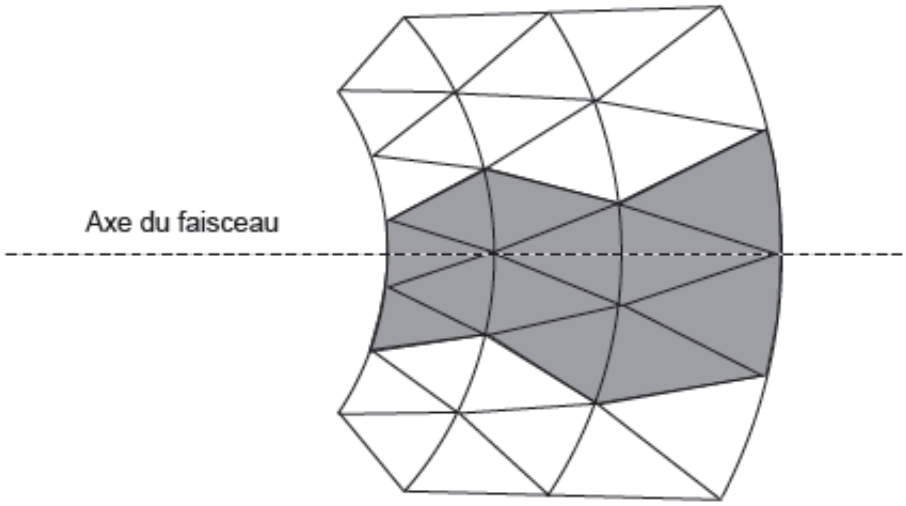


Figure 5.7: TRT module at 2004 combined test beam

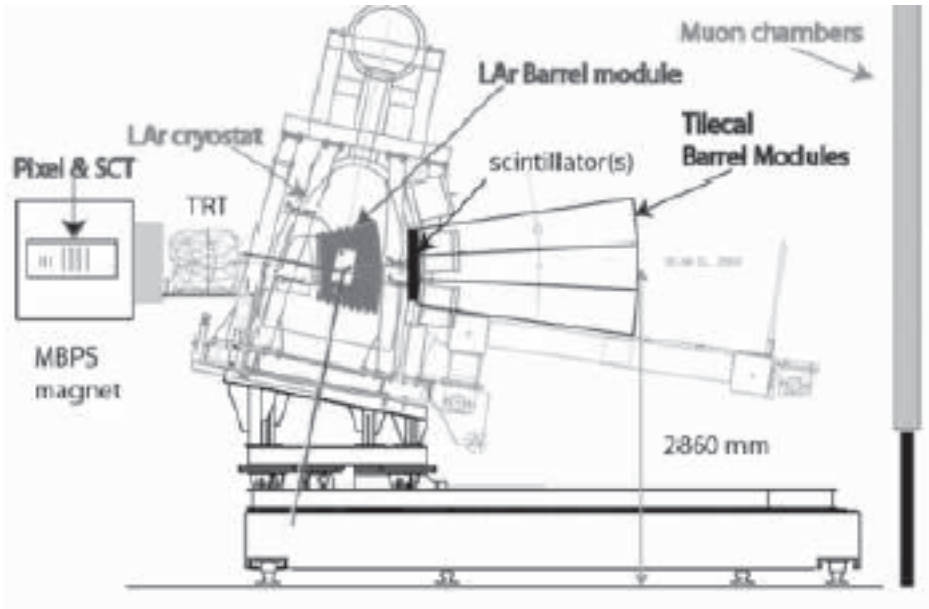


Figure 5.8: View from the side of the LAr and Tilecal calorimeters placed on the moving table. In this figure we can see also the position of the others detectors.

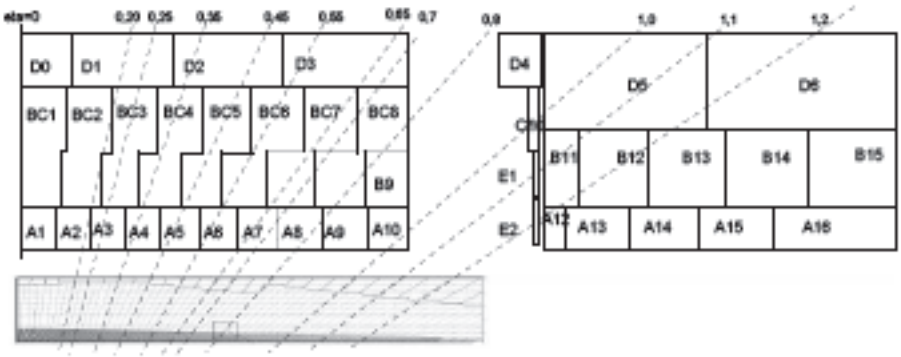


Figure 5.9: Top view of Tilecal and LAr cells.

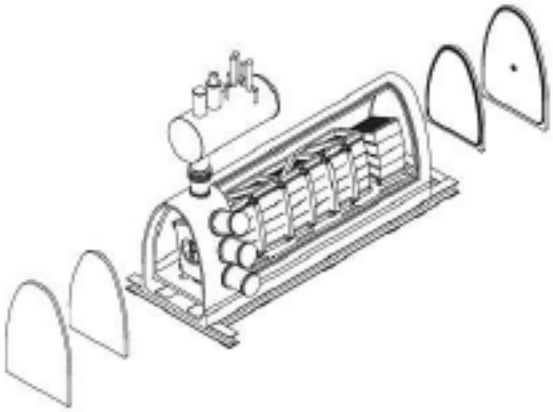


Figure 5.10: LAr view put inside the cryostat.

	Layers granularity	CTB 2004	ATLAS
LAr	$\Delta\eta \times \Delta\phi = 0.0031 \times 0.1$ $\Delta\eta \times \Delta\phi = 0.025 \times 0.0245$ $\Delta\eta \times \Delta\phi = 0.05 \times 0.025$	Thickness at $\eta = 0$: $6+16+2 = 24X_0$ $(\equiv 1.2\lambda)$	Thickness at $\eta = 0$: $6+16+2 = 24X_0$ $(\equiv 1.2\lambda)$
Cryostat		$\approx 1X_0$	$\approx 1X_0$
Distance between LAr and TileCal		≈ 30 cm	≈ 25 cm
TileCal	$\Delta\eta \times \Delta\phi = 0.1 \times 0.1$ $\Delta\eta \times \Delta\phi = 0.1 \times 0.1$ $\Delta\eta \times \Delta\phi = 0.2 \times 0.1$	Coverage in ϕ: 0.294 rad (3 modules) Thickness at $\eta = 0$: $1.4+4.0+1.8 = 7.2\lambda$	Coverage in ϕ: 2π rad (64 modules) Thickness at $\eta = 0$: $1.4+4.0+1.8 = 7.2\lambda$
Active thickness		$\approx 9.2\lambda$ at $\eta = 0$	$\approx 9.2\lambda$ at $\eta = 0$

Table 5.1: Granularity and angular coverage of the LAr and Tilecal calorimeters at 2004 test beam.

noise the sum is calculated in a limited region of η and ϕ around the beam direction. The window in eta corresponds to $\eta_{beam} \pm 0.2$ and in phi is equal to ± 0.2 rad ($\phi_{beam} = 0$). The electronic noise can be further reduced asking for a signal in each cell bigger than $|2\sigma_{noise}|$. For each run, the standard deviation σnoise of the electronic noise has been determined using randomly triggered events. Typical σ_{noise} values are 12 MeV (1st layer of LAr), 28 MeV (2nd layer of LAr), 22 MeV (3rd layer of LAr) .

5.2.3.2 Hadronic calorimeter Tilecal

TileCal is placed after the LAr in order to reproduce the geometry of the ATLAS detector as it will be installed in the pit. The distance between the active parts of the two calorimeters is 30 cm instead of the 25 cm foreseen in

η_{beam}	η_{min}	η_{max}
0.20	-0.01	0.41
0.25	-0.01	0.46
0.35	0.14	0.56
0.45	0.19	0.66
0.55	0.34	0.76
0.65	0.39	0.86

Table 5.2: Eta interval around the beam axis where are contained the Tilecal cells involved in the energy reconstruction.

ATLAS.

The three TileCal modules cover a region in ϕ between -0.2 and 0.2, and in eta it varies between -1 and 1 for the central barrel. Tilecal is segmented in three samples along the longitudinal direction. The information about the Tilecal granularity are reported in table 5.1.

Similarly, in order to reduce the contribution due to electronic noise, the same method as explained in section 5.2.3.1 is used. The values measured for TileCal are: 30 MeV (1st layer of TileCal), 30 MeV (2nd layer of TileCal) and 25 MeV (3rd layer of TileCal).

5.2.4 Muon spectrometer

Also different parts of the muon spectrometer were tested in 2004 test beam. The different subdetectors exposed to the beam were:

- *MDT (Monitored Drift Tubes)*
- *RPC (Resistive Plate Chambers)*
- *CSC (Cathode Strip Chambers)*
- *TGC (Thin Gap Chambers)*

The informations from all these detectors are not used in the present analysis. Therefore no detailed information is given here. More basic information can be found in [34].

5.3 Rejection cuts

The beam delivered by the SPS is made of protons; pions, electrons and muons produced on a target are transported down the H8 beam line to the experimental set-up. The fraction of each particle is related to the energy and to the polarization of the primary beam. The first step of the analysis consists

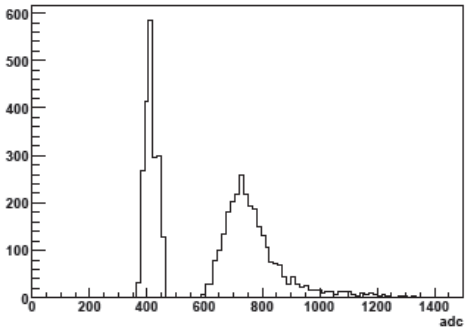


Figure 5.11: Signal in the MuTag scintillator. The signal produced by the muons corresponds with the peak around 700 ADC counts.

to select a pion [1] sample as pure as possible and monoenergetic. The pions are selected from all the remaining particles by mean of various cuts which we discuss below.

They are valid only for high energy particles; the cuts related to low energy particles are more complex and will be illustrated in detail in chapter 6.

5.3.1 Muon rejection

Muons are rejected using the scintillator MuTag placed behind the hadronic calorimeter and an absorber. With such a configuration only muons are generating a signal in the scintillator. Electrons and pions are absorbed well before the scintillator. Figure 5.11 shows a typical response of the scintillator (the peak at 400 ADC counts is the pedestal scintillator). To reduce the muon contamination we apply a cut on the ADC value; this cut we have taken as 500 ADC counts. The muon rejection factor can be increased asking for more than 5 GeV energy in the calorimeters (muons interact little in the LAr calorimeter). By this cut we reject muons which don't arrive to the scintillator because of the multiple scattering.

5.3.2 Electron rejection

The electron contamination varies with the beam conditions, in particular with the energy; it is maximal at 180 GeV. At the energies considered in this analysis, electrons impinging on the calorimeters deposit a very large fraction of their energy in the LAr calorimeter, figure 5.12. In the case of the pions, a large fraction of the energy is deposited in TileCal. Electrons were identified and then rejected requiring:

[1] At 20, 50 and 100 GeV we have pions and protons in the sample because we used a positive beam, while at 150, 180, 200 and 250 we have only pions in the sample because we used a negative beam.

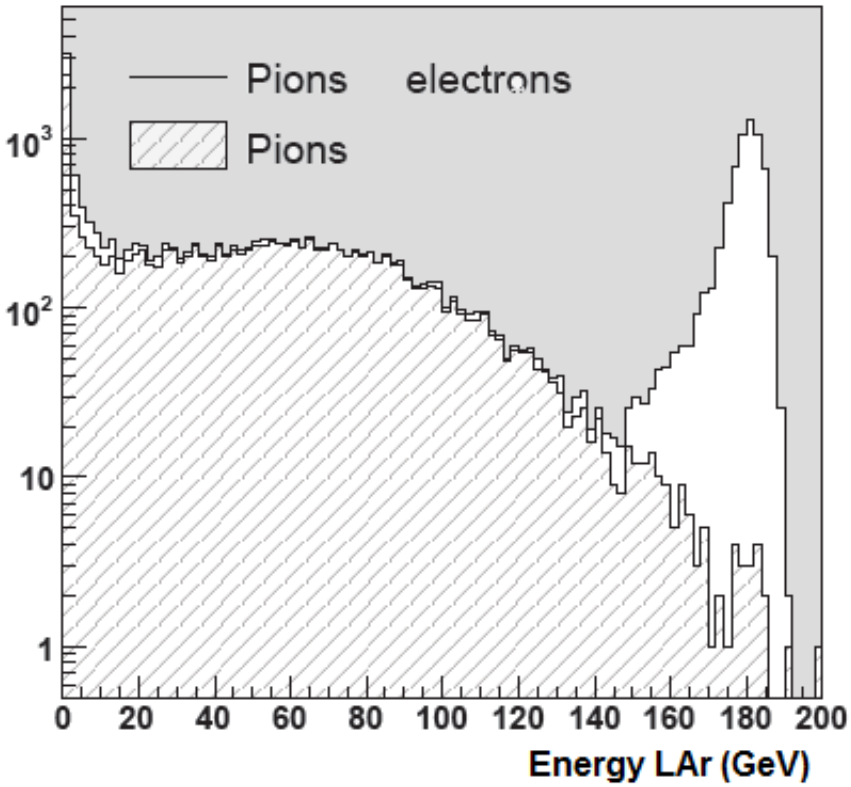


Figure 5.12: Energy distribution in LAr for a sample of electrons and pions and for a sample of pure pions. The nominal energy of the beam is 180 GeV.

$$\frac{E_{LAr}}{E_{LAr} + E_{Tile}} < 0.98 \tag{5.3}$$

Here, E_{LAr} denotes the energy measured in the LAr calorimeter and E_{Tile} denotes the energy measured in TileCal.

5.3.3 Interactions upstream the calorimeters

In order to reject particles which started to shower before their arrival in the calorimeters we use different scintillators placed in the beam line. Figure 5.13 shows the distribution for the S2 and S3 scintillators to muons, selected as explained in section 5.3.1 (the distribution individuated by the oblique lines corresponds to muons), and to other particles (essentially electrons and pions). The muon signal is taken as reference to determine the signal generated by an isolated single particle which passes through the scintillator. Larger signals, signals which are in the tails of the distributions, beyond the tails of the muon

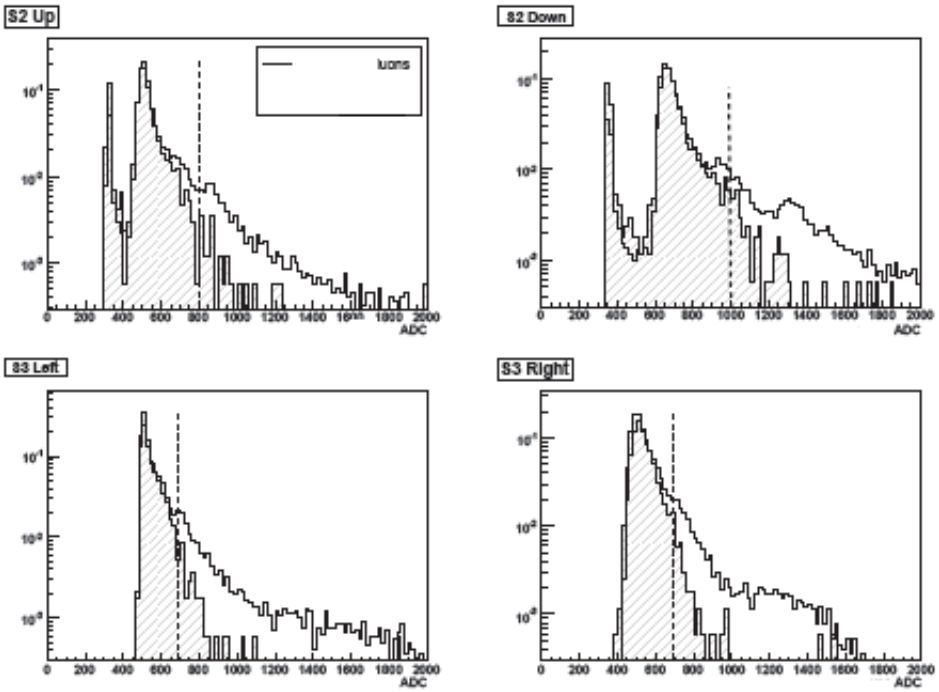


Figure 5.13: Signal distribution in the scintillator , for S2 and S3, read by four photomultipliers (up, down, left, right). The double peak in the top plots is generated by an inefficiency in the scintillator.

distributions, are considered as generated by multiple particles and rejected. The 4 values of the applied cuts are shown by the dashed lines. To evaluate the systematic introduced by these cuts another method was used to rejected particles that showered before the calorimeters. The cut applied on the scintillator is defined by

$$E_S < \mu_S + 2(\mu_S - \mu_{S,noise}) \tag{5.4}$$

The μ_S and the $\mu_{S,noise}$ are the mean values obtained from the signal distributions for the muon sample or for random triggers. No differences in these two methods were observed. The cut applied in the analysis is the first described in this section.

5.3.4 Beam chambers cuts

The spatial spread of the beam is monitored by four beam chambers. A cut can be applied to reduce the dimension of the impact point at the entrance of the calorimeter system. The accepted events have the impact point coordinates verifying in each chamber (n) the 2 conditions:

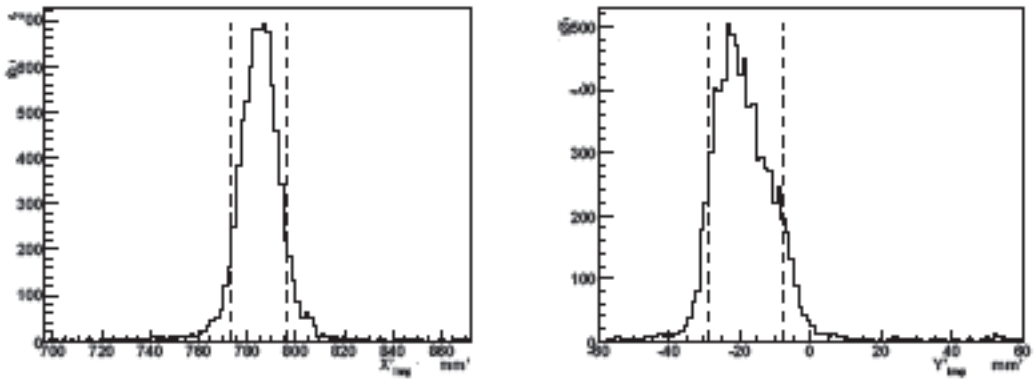


Figure 5.14: A typical distribution of the impact point in a wire chamber. The dashed lines represent the cuts obtained with the equations 5.5 and 5.6.

$$|y_{BCny}| < \mu_{BCny} \pm 2rms_{BCny} \tag{5.5}$$

$$|x_{BCnx}| < \mu_{BCnx} \pm 2rms_{BCnx} \tag{5.6}$$

Where μ_{BCny} and μ_{BCnx} correspond to the mean values of the distributions of the measured beam impact points, respectively in x and y. 2rmsBCnx and 2rmsBCny are the corresponding root mean squared (rms) values.

A typical cut is shown in figure 5.14.

5.4 Measure of the response and the resolution of the calorimeters

Before to start the analysis there is another cut to apply concerning the LAr preshower [14]; we ask for a minimum ionizing particle in order to have only hadrons that start their shower in the calorimeters and not in the cryostat. Once all the described cuts have been applied we get a hadron sample ready for the analysis The combined response of the two calorimeters depends from different parameters; first of all the non-compensation of the two calorimeters and the energy response to hadrons which is not linear. This non compensation is different for the two calorimeters; this means that the response to hadrons will be different in the LAr and in the TileCal. Another thing to consider is the energy loss in the cryostat, which is difficult to evaluate. It is known that the combined response to hadrons is a function of the incident energy, eta and the position where the shower begins. In this thesis we will not discuss about the corrections to compensate these effects. We will concentrate on the combined response and we will compare the results with the simulation.

The combined energy reconstruction was done in the following way:

- sum of the energy in the cells inside the window $\Delta\eta \times \Delta\phi = 0.4 \times 0.4$ around the beam axis in the LAr,
- sum of the cells in a window depending on the η of the beam, see table 5.2, for Tilecal.

In chapter 3 we have explained how the signal is calibrated at the electromagnetic scale. This calibration is significantly different for the two calorimeters and this means that the two calorimeters are not intercalibrated. If we assume that this scale is not too different we can express the total energy as:

$$E_{tot} = E_{LAr} + E_{Tile} \tag{5.7}$$

Figure 5.15 shows the distribution of the energy in the LAr, in Tilecal and the total energy for pions with an energy of 180 GeV and eta equal to 0.35.

We can see that the distribution of the total energy can be fitted with a gaussian, the χ^2 of the fit is good (see bottom right plot in figure 5.15) , this means that the two electromagnetic scales are not too different and that the assumption done before is valid.

5.4.1 Measurement of the beam energy

The beam energy is calculated for each run from the magnet currents and the beam-line collimator settings. A Hall probe was used to precisely determine the magnetic field in the bending magnets. Based on this Hall probe measurement the relation between the measured magnet currents and the magnetic field in the bending magnets is known. The precision of the beam momentum is given by:

$$\frac{\Delta E_{beam}}{E_{beam}} = \frac{25\%}{E_{beam}} \oplus 0.5\% \tag{5.8}$$

where E_{beam} is the beam energy. The beam energy values and the systematic error are given in table 5.3 for the different settings of the beam.

5.4.2 Combined fractional response

The fractional response of the calorimeters is defined as the ratio between the value of the reconstructed energy and the measured beam energy, as resumed in the equation below:

$$R_h = \frac{E_{rec}}{E_{beam}} \tag{5.9}$$

As explained in section 5.2.3.2 the value of the reconstructed energy is obtained by the sum of all the cells which are in eta window, as defined in section 5.4, and with an energy measured in the individual cell that satisfies

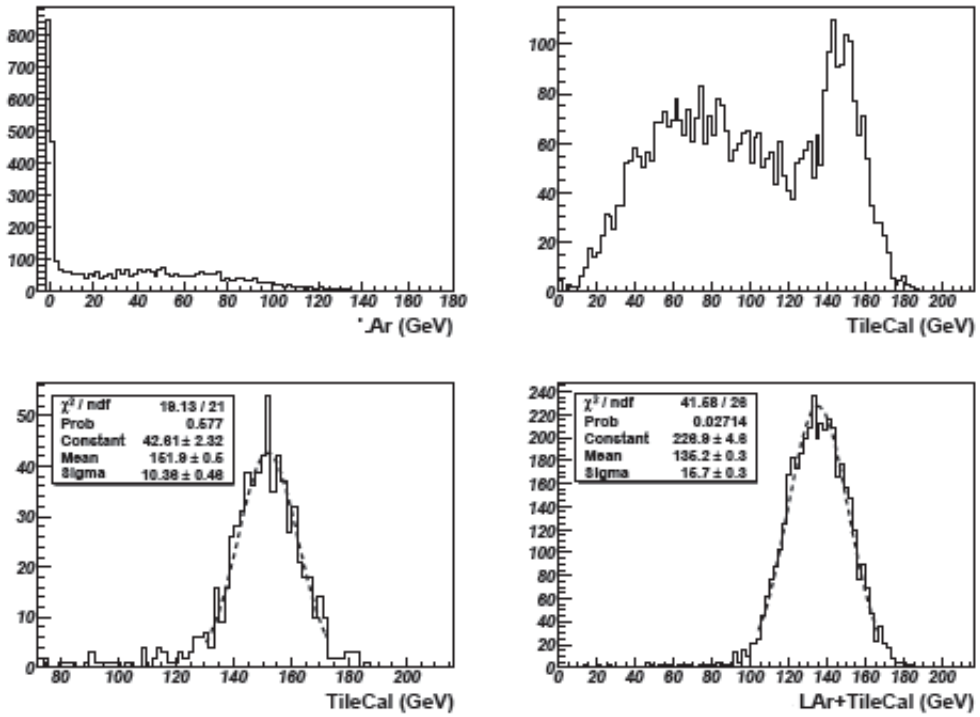


Figure 5.15: Energy distribution for pions at 180 GeV and eta equal to 0.35. In top left is shown the response to pions in the LAr, in top right the response to pions in Tilecal, in bottom left the response of Tilecal to a pion at minimum of ionization and the combined response in bottom right.

E_{nom}[GeV]	E_{beam}[GeV]	ΔE_{beam}[%]
20	20.2	1.3
50	50.3	0.7
100	100.5	0.6
150	150.5	0.5
180	180.6	0.5
200	200.8	0.5
250	251	0.5

Table 5.3: Measured beam energy with respect to the nominal value and systematic error on the measure, and obtained using equation 5.8.

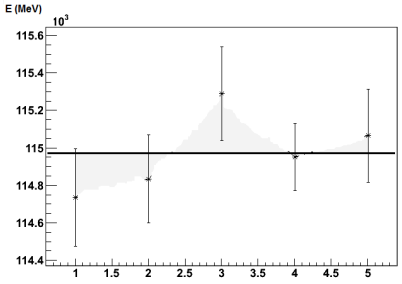


Figure 5.16: Distribution of energy values for different runs at 150 and eta 0.35. The result of the fit is quoted as E_{rec}.

the condition $|E_{cell}| > 2\sigma_{noise}$ where σ_{noise} is the standard deviation of the electronic noise. The energy distributions are fitted by a Gauss function with iteration of the fit in the range of $\pm 2\sigma$ around the peak value, where σ is the standard deviation. The iteration stops when $\Delta\mu_{fit}$, which is the difference between the peak values of two consecutive fit is lower than 10 MeV. The expression for $\Delta\mu_{fit}$ is resumed below:

$$\Delta\mu_{fit} = \mu_i - \mu_{i-1} < 10MeV \tag{5.10}$$

$\mu_i$and $\mu_{i-1}$are the guassian peaks of the last two iterations. For runs at the same energy and at the same eta the values μ_i, that satisfies equation 5.10, are fitted with a constant, see figure 5.16. The result of the fit is quoted as the measurement (E_{rec}). This procedure allows also checking the stability of the TileCal energy response, that as shown in figure 5.16 for a run at 150 GeV and eta 0.35 is satisfying. The uncertainty of this measure is given by the statistical error and by the systematic error coming from the uncertainty on the beam measurement. At these errors we have to add also the systematic errors coming from the incertitude on the EM scale in LAr and in TileCal.

In table 5.4 are summarized the values of R_h and the errors $\Delta R_h$where the statistical and systematic error are summed in quadrature. The systematic error coming form the cuts is negligible.

Figure 5.17 shows the evolution of the combined fractional response to hadrons as a function of the beam energy for the different available values of η. The response shows a non-linearity that is a typical property of non-compensating calorimeters ($e/h > 1$); in fact the response to the electromagnetic component is higher than the response to the hadronic component of the shower.

Figure 5.16 shows that the combined fractional response is higher at large values of the beam energy, confirming that the electromagnetic component is more important at high energies.

Figure 5.17 shows the combined fractional response as function of eta for different energies; one observes a dependence of the fractional response to the beam incidence angle (eta).

E_{nom}	η_{beam}	R_h	ΔR_h(total)	R_{σ_h}	ΔR_{σ_h}(total)
20^+	0.25	0.65	0.01	0.252	0.006
20^+	0.35	0.64	0.01	0.257	0.004
20^+	0.45	0.64	0.01	0.248	0.004
20^+	0.55	0.64	0.01	0.249	0.004
20^+	0.65	0.63	0.01	0.265	0.004
50^+	0.25	0.70	0.01	0.180	0.002
50^+	0.35	0.69	0.01	0.172	0.001
50^+	0.45	0.70	0.01	0.180	0.002
50^+	0.55	0.70	0.01	0.182	0.002
50^+	0.65	0.68	0.01	0.186	0.002
100^+	0.25	0.73	0.01	0.135	0.002
100^+	0.35	0.72	0.01	0.141	0.002
100^+	0.45	0.72	0.01	0.140	0.001
100^+	0.55	0.71	0.01	0.147	0.001
100^+	0.65	0.72	0.01	0.189	0.001
150^-	0.25	0.76	0.01	0.124	0.002
150^-	0.35	0.75	0.01	0.131	0.002
150^-	0.45	0.76	0.01	0.129	0.002
150^-	0.55	0.76	0.01	0.140	0.003
150^-	0.65	0.75	0.01	0.148	0.003
180^-	0.25	0.77	0.01	0.125	0.002
180^-	0.35	0.76	0.01	0.126	0.002
180^-	0.45	0.76	0.01	0.127	0.002
180^-	0.55	0.76	0.01	0.130	0.005
180^-	0.65	0.76	0.01	0.136	0.003
200^-	0.25	0.77	0.01	0.118	0.002
200^-	0.45	0.76	0.01	0.125	0.002
200^-	0.55	0.76	0.01	0.128	0.002
200^-	0.65	0.76	0.01	0.133	0.003
250^-	0.25	0.77	0.01	0.117	0.001
250^-	0.55	0.79	0.01	0.113	0.001
250^-	0.65	0.77	0.01	0.120	0.001

Table 5.4: R_h, see equation 5.9, and R_{σ_h} , see equation 5.11, with the respective errors. The error for R_h is the sum in quadrature of the statistical error on the reconstructed energy and the systematic error on the beam energy measure, on the LAr and TileCal EM scale and on the detector uniformity. The error for R_{σ_h} is only the statistical error calculated doing the sum in quadrature of the error on the standard deviation of the distribution and the error on the reconstructed energy.

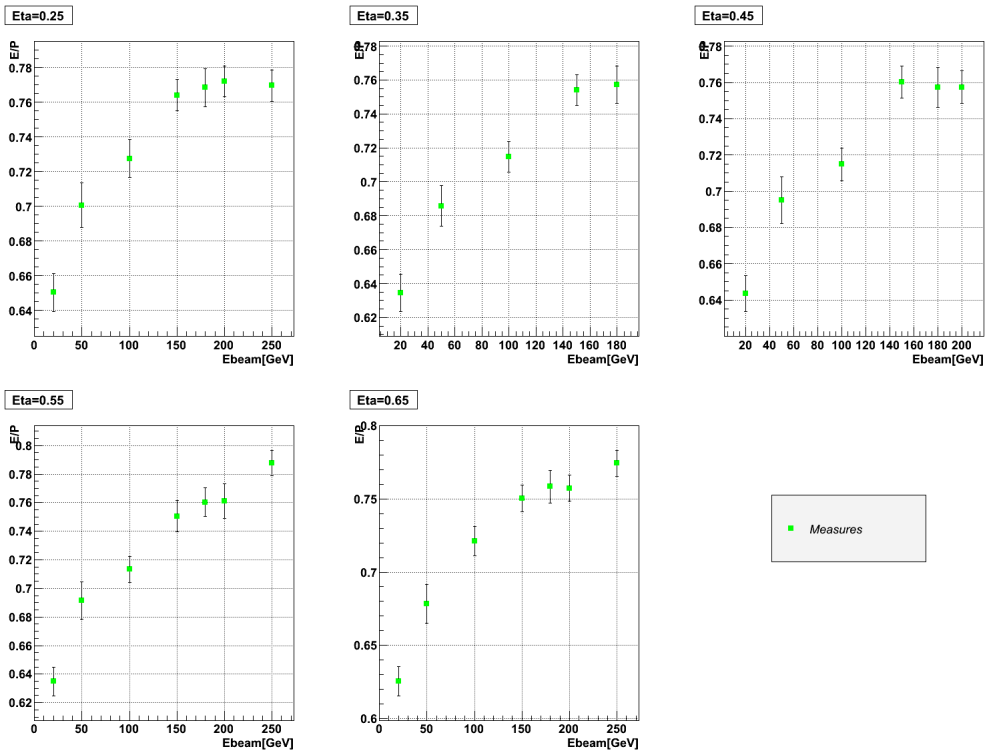


Figure 5.17: Evolution of the fractional response to hadrons as a function of beam energy.

5.4.3 Combined fractional resolution

We define the combined fractional resolution as the ratio between the standard deviation of the energy distribution and the total reconstructed energy (E_{rec}), as written in the equation below:

$$R_{\sigma_h} = \frac{\sigma_{rec}}{E_{rec}} \tag{5.11}$$

Figure 5.19 shows the evolution of the combined fractional resolution as function of $1/\sqrt{E_{beam}}$, for the different values of eta available. In table 5.4 are resumed the values obtained for R_{σ_h} with the statistical error calculated doing the sum in quadrature of the error on the standard deviation of the distribution and the error on the reconstructed energy.

Fitting the distributions one gets access to the resolution sampling term and the constant term for the various beam impact points. The following parametrization is adjusted to the data:

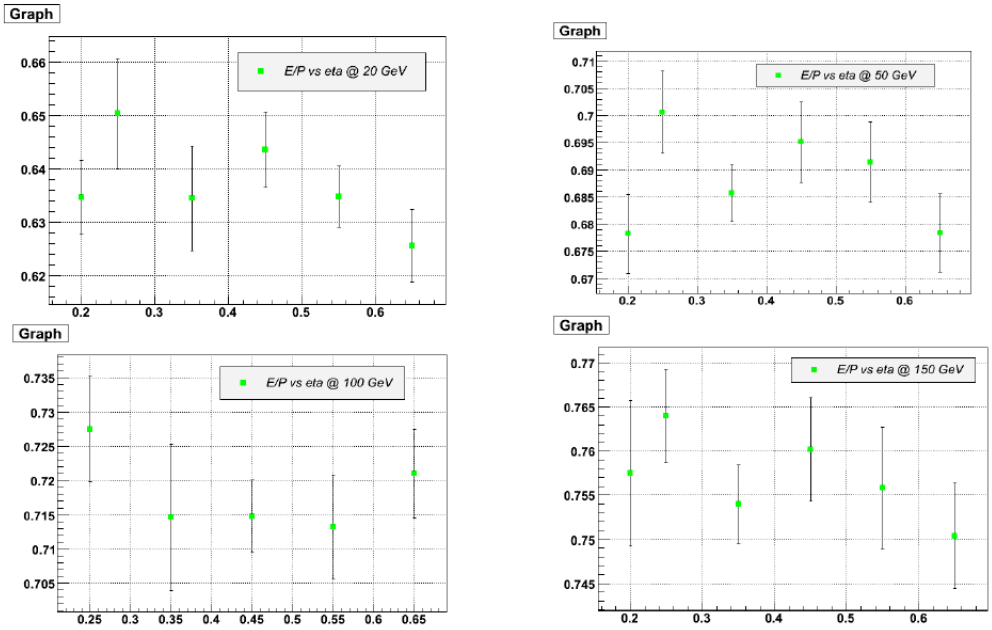


Figure 5.18: Evolution of the fractional response to hadrons as a function of eta, for different values of the beam energy.

η	a [% $GeV^{-\frac{1}{2}}$]	b[%]
0.25	106±1	8.6±0.2
0.35	105±1	9±0.1
0.45	103±1	9.4±0.1
0.55	109±1	9.6±0.1
0.65	116±1	10.2±0.1

Table 5.5: Parameters of the resolution function $\frac{\sigma_{rec}}{E_{rec}} = \frac{a}{\sqrt{E_{beam}}} \oplus b$ for the pion sample.

$$\frac{\sigma_{rec}}{E_{rec}} = \frac{a}{\sqrt{E_{beam}}} \oplus b \tag{5.12}$$

The parameter a characterizes the sampling fluctuations and the parameter b represents the constant term. In appendix A the calculation to obtain relation 5.12 is shown.

The results of the fit are resumed in table 5.5.

It is important to notice that no correction concerning non-compensation effects, intercalibration and energy losses were applied[2]; so is not surprising that values obtained for the resolution are different from what is expected in ATLAS[12]. But the aim of this analysis is not the optimization of the performances of the calorimeters, but to obtain quantities that can be easily compared with the simulation.

The fractional resolution will be the second parameter after the fractional response which we will compared to the simulation.

5.4.4 Comparison between data and Monte Carlo

The experimental results were compared to the predictions of the Monte Carlo (MC) simulation program Geant4[3]. The Monte Carlo simulation models the interaction of particles with the detector material on a microscopic level. The detailed shower development follows all particles that interact electromagnetically in the calorimeter with an expected travel path (range) larger than 1 mm. Also hadron interactions and photo-nuclear interactions are simulated. The QGSP BERT hadronic showering model was used in the simulation. This is the model presently being used in the simulation of the ATLAS detector for proton-proton collisions.

In order to compare real data with Monte Carlo, the energy was reconstructed using the same method in the two cases. The comparison between data and Monte Carlo could be quantified using the quantities:

[2] In order to correct for these effects we need the results coming from TileCal standalone analysis.

[3] The version 4.91 has been used.

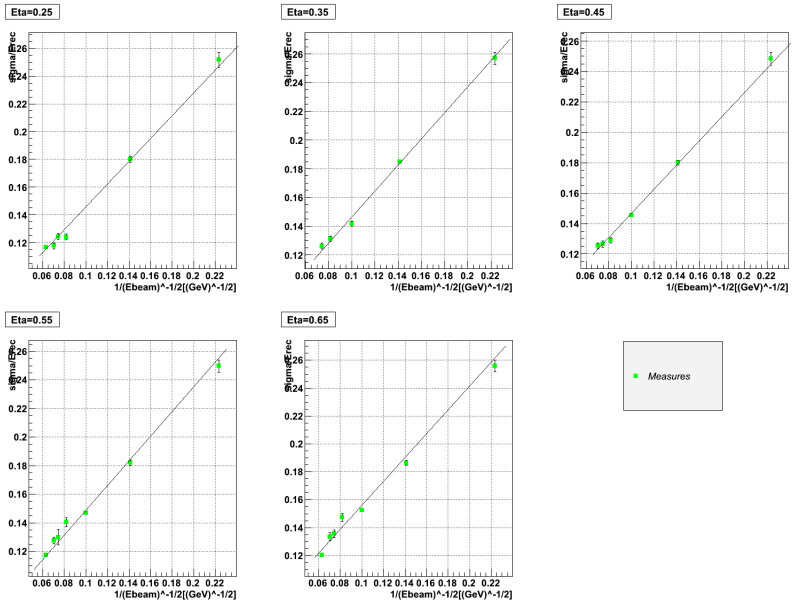


Figure 5.19: Fractional energy resolution represents as function of $1/\sqrt{E_{beam}}$.

$$\left(\frac{R_{E_{hMC}}}{R_{E_h}}\right) - 1 \tag{5.13}$$

$$\left(\frac{R_{E_{\sigma hMC}}}{R_{E\sigma_h}}\right) - 1 \tag{5.14}$$

The results are reported in table 5.7. The presence of protons in the sample (at 20, 50 and 100 we are using a positive beam), has been reproduced in the simulation. The values for the proton contamination were taken using the TRT information for positive beams and are resumed in table 5.6. At 20 GeV to reproduce the fraction of proton in the sample we used instead of the value reported in table 5.6, that is negative, the value 0 ± 0.2. Figure 5.20 and table 5.7 (values are in %) show a very good agreement between data and Monte Carlo; a difference of about 2% is present between data and Monte Carlo, but if we tak into account the errors on the fractional energy this discrepancy is negligible.

For the resolution a deviation between -14% at 20 GeV and -1% at 250 GeV is present, figure 5.21.

Conclusions The combined energy reconstruction was realized doing the sum of cell responses calibrated at the electromagnetic scale for LAr and TileCal calorimeters. Such a reconstruction allows to compare the data with the simulation. In this chapter the fractional energy response was measured with an

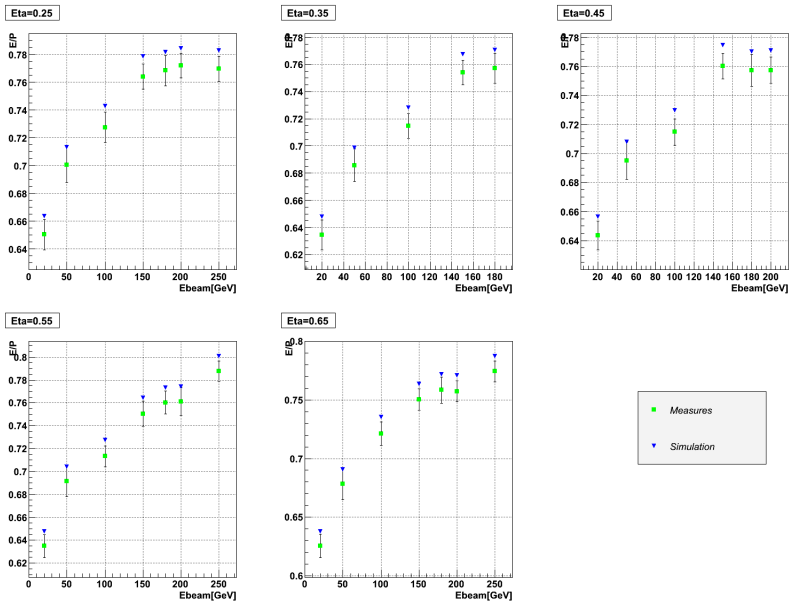


Figure 5.20: Measured and simulated fractional response to pions. The presence of protons in the sample at 20, 50 and 100 was considered (presence of a positive beam).

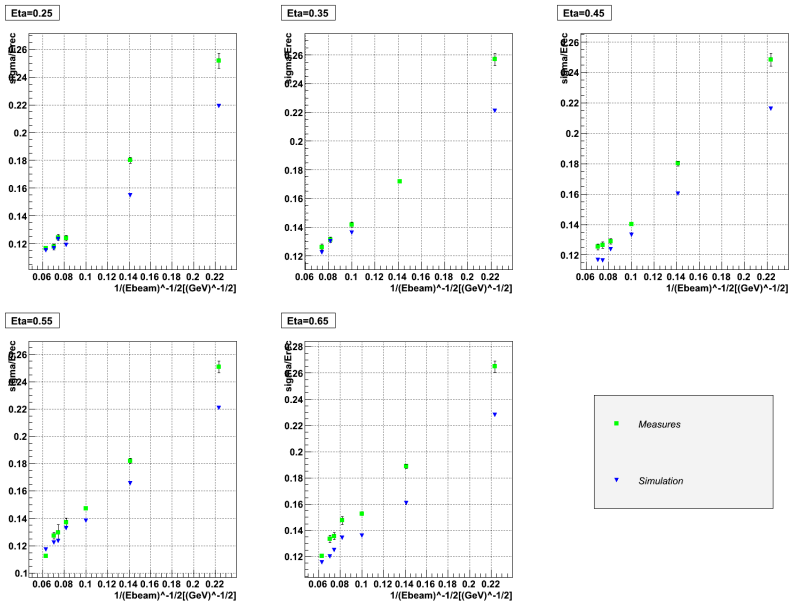


Figure 5.21: Fractional energy resolution for data and the simulation.

E[GeV]	f_p
20	-0.15±0.32
50	0.45±0.12
100	0.76±0.04

Table 5.6: Proton contamination f_p using TRT in case of positive beams

error of 1% dominated by the uncertainty on beam energy and non uniformity effects in the calorimeters. The fractional energy resolution has been measured with an error of 2% or lower. These measures can be used as reference for the comparison with the simulation. The difference with simulation is about 2% on the fractional reconstructed energy. This difference can be explained by the fact that the longitudinal profile of the shower is systematically longer in the simulation than in the data, but an analysis of the shower development is necessary. For the points at 50 and 100 GeV an additional systematical error coming from the values of proton contamination has been considered. This error equal to 1% at 50 GeV and 0.4% at 100 GeV and is considered in the errors on table 5.7.

The simulation can be used now for the study of the calorimeters behavior in the case of jets and the determination of the jet energy scale.

E_{nom}	η_{beam}	$\left(\frac{R_{E_{hMC}}}{R_{E_h}}\right) - 1$	$\left(\frac{R_{E_{\sigma hMC}}}{R_{E\sigma_h}}\right) - 1$
20^+	0.25	2±2	-13±2
20^+	0.35	2±3	-14±2
20^+	0.45	2±3	-13±2
20^+	0.55	2±2	-12±2
20^+	0.65	2±2	-14±2
50^+	0.25	2±1	-14±1
50^+	0.35	2±1	-10±1
50^+	0.45	2±1	-11±1
50^+	0.55	2±1	-9±1
50^+	0.65	2±	-15±1
100^+	0.25	2±1	-7±1
100^+	0.35	1.9±0.7	-4±1
100^+	0.45	2.1±0.7	-5±1
100^+	0.55	2±1	-6±1
100^+	0.65	2±1	-11±1
150^-	0.25	2±1	-4±1
150^-	0.35	2±1	-1±1
150^-	0.45	2±1	-4±1
150^-	0.55	2±1	-3±1
150^-	0.65	2±1	-9±1
180^-	0.25	2±1	-1±1
180^-	0.35	2±1	-3±1
180^-	0.45	2±1	-8±1
180^-	0.55	2±1	-5±1
180^-	0.65	2±1	-8±1
200^-	0.25	2±1	-1±1
200^-	0.45	2±1	-7±1
200^-	0.55	2±1	-4±1
200^-	0.65	2±1	-10±1
250^-	0.25	2±1	-1±1
250^-	0.55	2±1	4±1
250^-	0.65	2±1	-4±1

Table 5.7: Relative difference in percentage of the response and resolution between data and simulated events, for different values of the nominal beam energy and pseudorapidity. The errors were obtained combining in quadrature the systematic error and the statistical error. At 50 and 100 GeV the systematic error coming from the presence of protons in the sample is considered. Statistical error for the Monte Carlo data is negligible.

Chapter 6

ATLAS calorimeters response to very low energy pions

Part of the 2004 combined test beam program was dedicated to the study of the response of the central calorimeters to low energy pions (energy lower than 10 GeV). This study is very important because a large part of the fraction of jet energy is carried by particles of a few GeV. For example, in a 150 GeV jet, particles with energy smaller than 10 GeV carry about 25% of the total energy [35]. To illustrate this, in figure 6.1 is shown the result of a simulation of the jet energy fraction carried by charged particles with energies lower than 10 GeV; the jet energy is reconstructed in a cone of ΔR=0.7. Therefore, for a precise jet energy reconstruction an accurate knowledge of the response of the central calorimeters to low energy charged particles is needed. For this reason the H8 beam line as been set up in 2004 to allow data taking at low energies. In this chapter we will study the response of the central calorimeters to charged pions with a momentum between 3 and 9 GeV. At these energies the beam is strongly contaminated by electrons and muons; part of the chapter also addresses the selection criteria to obtain a pure pion beam.

6.1 The experimental set-up

In the SPS H8 line, the very low-energy (VLE) pion beam is produced by an 80 GeV secondary pion beam impinging on a 1 m-long polyethylene target [36]. The target is a cylinder with a diameter of 4 cm and is placed about 45 m upstream of the detectors, 6.2. An absorber (beam dump) is placed after the target to stop secondary particles with a small detection angle.

In figure 6.2 is shown the instrumentation of the beam line upstream to the detectors. There are four dipole magnets (B1, B2, B3 and B4) which perform the momentum and charge selection of VLE particles. Negative pions were selected; their response in the calorimeters is discussed in this chapter. A threshold Cerenkov counters C [37] located between B3 and B4, is used to separate electrons from pions and muons. The transverse beam profile is

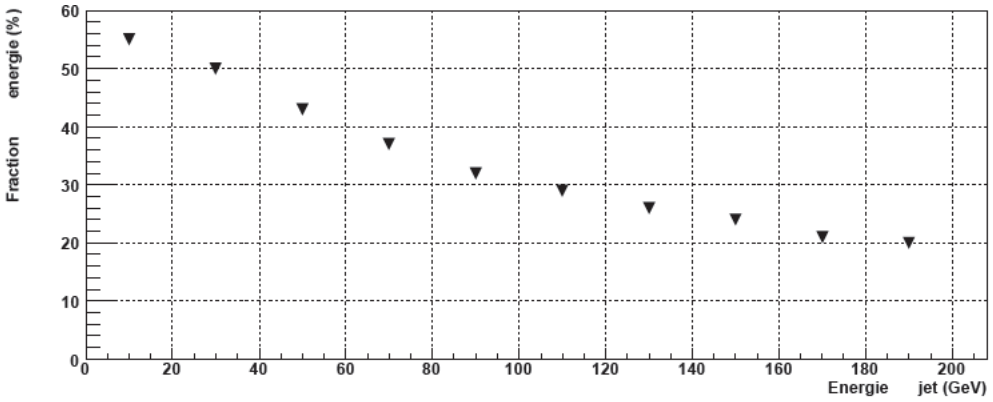


Figure 6.1: Jet energy fraction carried by charged particles with an energy lower than 10 GeV as a function of the jet energy.

monitored by five wire chambers, BC- 2 to BC2 [38]. Two scintillators, S2 and S3, with an active surface of 55 cm2 [39] were used in coincidence to trigger the data acquisition and to provide the trigger timing.

Depending the setting of the beam elements, the beam is composed of:

- pions with a momentum ranging between 3 and 9 GeV,
- electrons with the same momentum,
- high-energy muons, E<80 GeV, which did not stop in the absorber (halo muons). These muons are not expected to be synchronous with the trigger of the data acquisition,
- low-energy muons coming from meson decays. Their momentum is less than or equal to the momentum of the initial meson.

6.2 The selection criteria

In order to apply selection criteria which will permit to select an as pure as possible pion sample, the following subdetectors have been used:

- The TRT (Transition Radiation Tracker) to count the number of tracks and to separate electrons from pions and muons,
- The Cerenkov counter C to separate between electrons, pions and muons,
- The wire chamber BC-2 to reduce the spatial extension of the beam, to reject muons coming from the high energy beam line,
- The TILECAL calorimeter in order to separate pions and muons.

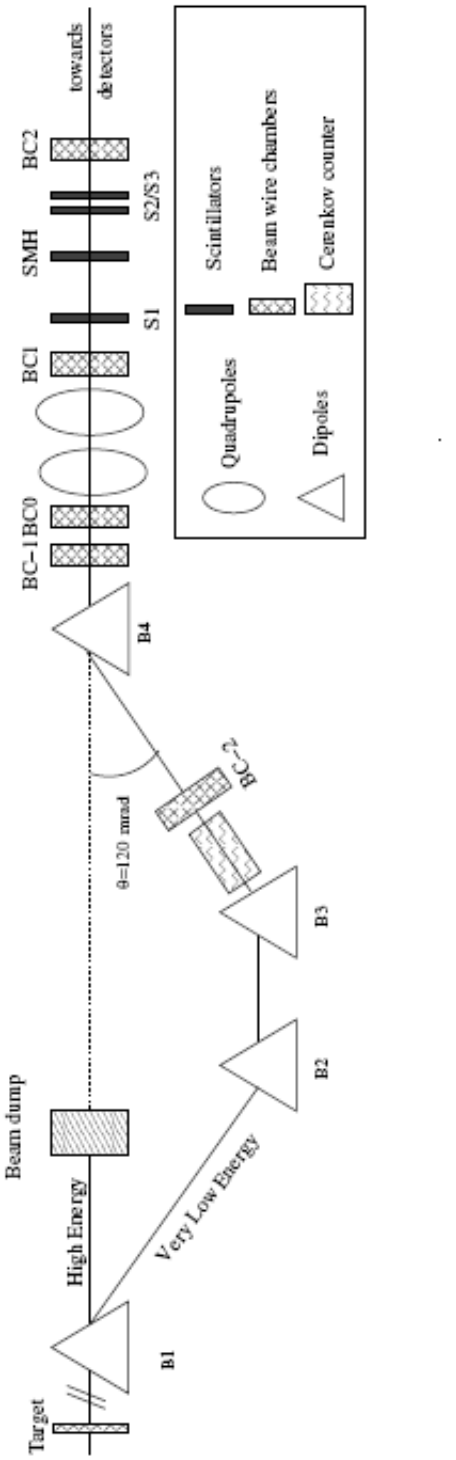


Figure 6.2: Layout of the H8 beam line. Only the devices used in the analysis are shown.

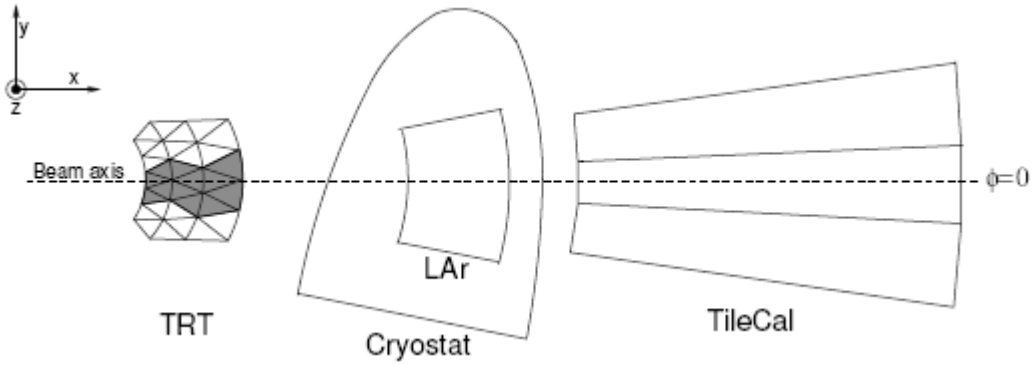


Figure 6.3: Side view of the detector layout in the 2004 combined test beam. Only sub-detectors that are used in this paper are represented.

The various selection cuts are now described in more details.

Two barrel modules of the TRT were placed in front of the calorimeters (see figure 6.3). These modules are composed of layers of straws filled with an active gas (each straw acting as a drift chamber), surrounded by a radiator. The readout electronics is designed to provide two types of digital signals, depending on the amplitude of the analog signal from the straws:

- a low-threshold (LT) signal for tracking hits (a track is defined by 25 LT hits),
- a high-threshold (HT) signal for energetic photons produced by transition radiation from electrons [41].

A particle passing through the TRT can be identified as an electron or a pion, depending on the number of HT hits recorded along its track. In the present analysis, the TRT information has been used both to select single track events and for pion/electron separation. By selecting one reconstructed track in the TRT, and only one, one rejects events with a small and high energy values reconstructed in the calorimeter. This is illustrated by figure 6.4. The left side plot of figure 6.4 shows the number of reconstructed TRT tracks for a beam of 9 GeV. The impact on the total (LAr+TileCal) reconstructed energy of the number of tracks (full line corresponds to one track and dotted line to no selection on the number of tracks) is shown on the right plot of figure 6.4. The peak at 8 GeV corresponds to electrons; pions are in the region between 2 and 6 GeV. The lower values obtained for the pions are due to the non compensation of the hadronic calorimeter; this non compensation generates a smaller response to pions than electrons for the same incident energy. Only events in which one single particle reaches the calorimeters are selected. This selection is obtained by requiring exactly one reconstructed TRT track with more than 30 LT hits (*cut#1*).

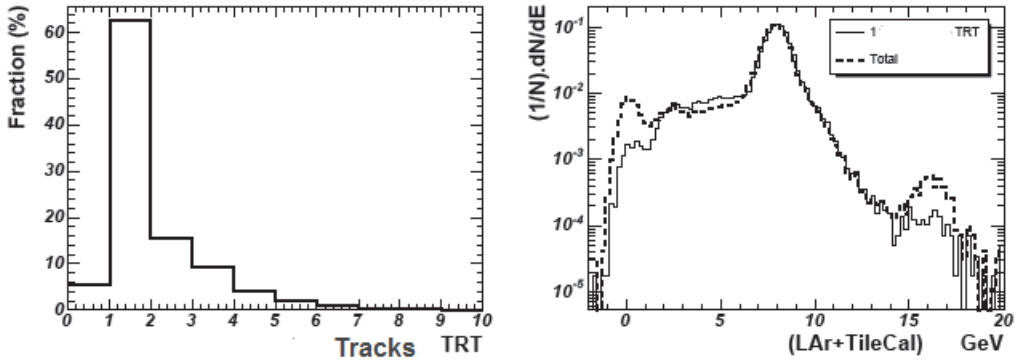


Figure 6.4: On the left: distribution of the number of reconstructed tracks in the TRT. On the right: influence of the number of tracks on the reconstructed energy.

cut#2: to select particles with a well defined trajectory through the beam line, a hit in at least one of its two planes is required. In particular the presence of a hit in BC-2 ensures that the incident particle has passed through the VLE line. In this way we reduce the contamination from the high-energy halo muons passing through the beam dump. To further reduce these high-energy halo muons we have used another feature of the system. When a very low energy particle triggers the data acquisition system, a high energy muon from the halo may arrive close enough in time to be registered together with the low energy particle. But the signal produced in TileCal by halo muons is, in general, not synchronous with the trigger. This feature can be exploited to reject some of the high-energy halo muons. The time difference t between the trigger time ($t_{trigger}$) and the time of the reconstructed signal shape in each cell of TileCal (t_{pulse}) was computed. On the left of figure 6.5 is shown the measured distribution of Δt for a 9 GeV pion beam. Only cells with a signal greater than 75 MeV, corresponding to three times the electronic noise, enter into the distribution. The sharp peak at Δt =50 ns corresponds to particles in time with respect to the trigger while the large uniform tails are due to out-of-time particles. For comparison, of the figure 6.5 shows the distribution of Δt for an almost pure 100 GeV pion beam. A negligible number of out-of-time events are expected in this case. To reject high-energy halo muons only events with $45 < \Delta t < 80$ ns in all TileCal cells with a signal larger than 75 MeV are kept (*cut#3*).

In order to reject remaining high-energy halo muons we used the property of high energy muons to penetrate deeper in the material than pions. In fact low energy pions are not expected to deposit energy in the last longitudinal sample of TileCal, called Tilecal3. On the other hand muons will produce a signal there. Figure 6.6 shows the energy deposited in TileCal3 for a pure 20 GeV muon sample and for a 7 GeV pion sample contaminated by halo muons.

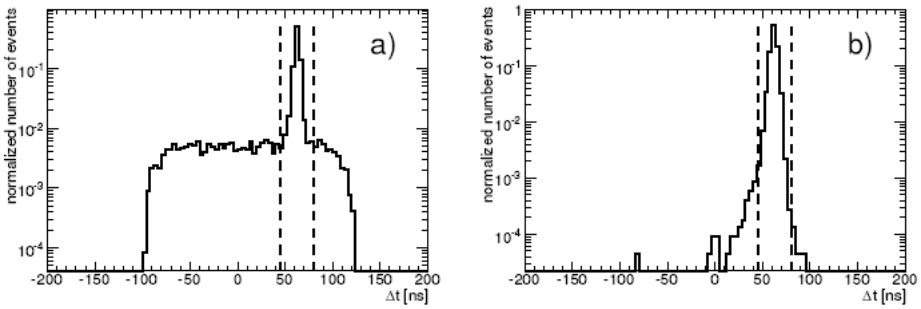


Figure 6.5: Distributions of $\Delta t = t_{pulse} - t_{trigger}$ for TileCal cells with a signal larger than 75 MeV a) for a 9 GeV pion beam, b) for a 100 GeV pion beam where no out-of-time particles are expected. The region selected in the analysis is shown.

The peak around zero corresponds to the pedestal and is due to VLE pions that do not reach TileCal3. The peak around 500 MeV corresponds to the typical energy deposit from high-energy muons. Requiring a small energy deposition in TileCal3 reduces the contamination from high-energy muons. The selection $E_{Tilecal3}$ <160 MeV, materialized by the vertical line in figure 6.6, been applied to select low-energy pions and reject muons (*cut#4*).

This cut could introduce a bias in the pion reconstructed energy, by removing pions interacting late in the calorimeter. A Monte-Carlo simulation was realized to quantify this effect. This study shows that 10% of pions are rejected and the mean reconstructed energy decrease of 5%. This cut was applied also on the simulated calorimeters response to low energy pions, to be compared with real data.

Cut #5&6: Electron rejection.

Electrons were rejected making use of the signal (C) measured in the Cerenkov counter and the number of HT hits (nTR hits) produced in TRT. The Cerenkov pressure was set such that the pions and muons were below threshold and electrons above. Electrons are expected to produce 2.5 to 15 TRT HT hits per track in average, while pions and muons will produce from 0 to 5 hits per track. Figure 6.7 shows the three-dimensional distribution of the Cerenkov signal C versus nTR hits in the case of a 9 GeV beam. Two regions can be identified quite easily, one populated by electrons (high C and nTR hits values) and the other by pions and muons (small C and nTR hits values). The following cuts on the ADC counts (*cut#6*) and on nTR (*cut#5*) are applied to differentiate electrons from pions:

- pions (muons): C<600 ADC counts and n_TRhits<3 and
- electrons: C>700 ADC counts and n_TRhits>5.

The number of events passing the selection criteria are reported in table 6.1 (for an impact point on the calorimeter corresponding to η=0.35 and ϕ=0)

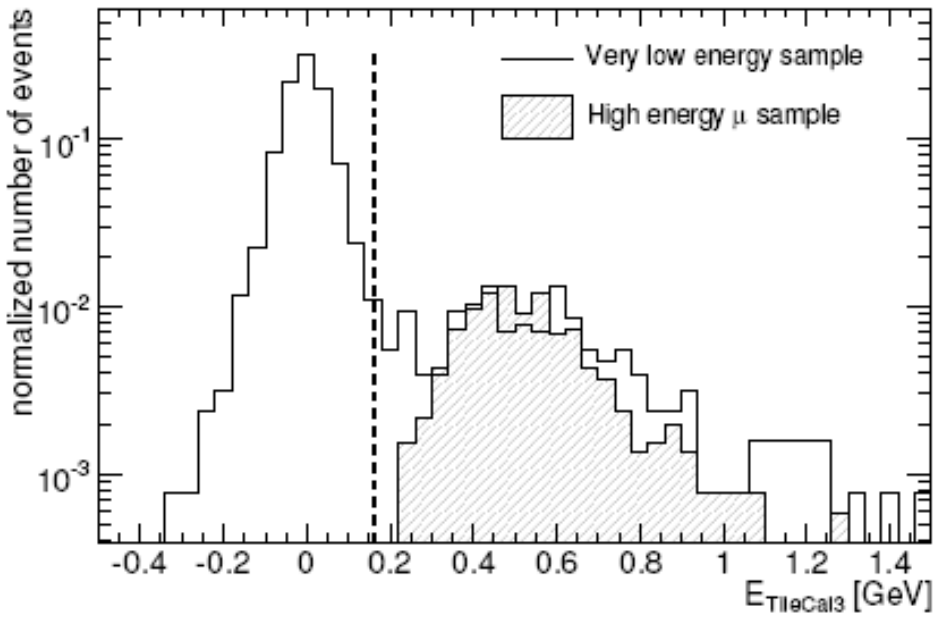


Figure 6.6: Distribution of the energy deposited in the 3rd sample of TileCal, ETileCal3. The empty distribution corresponds to a 7 GeV η_{beam}=0.2 pion beam with high-energy muon contamination. The hatched distribution corresponds to a 20 GeV muon beam at η_{beam}=0. Events with ETileCal3 <160 MeV were selected in the analysis.

and nominal beam energies of 3, 5, 7 and 9 GeV). All other runs show similar cut efficiencies, demonstrating a satisfactory stability of the beam conditions and of the detector operations during the data taking. The number of events in the pion samples (Nπ) is about 100 at 3 GeV and increases up to about 2000 at 9 GeV.

6.3 Pion sample contamination study

In this section the method applied to evaluate the pion sample contamination, in particular the electron and the muon contamination, will be discussed in detail.

6.3.1 Electron contamination

After all the cuts a residual quantity of electrons in the sample is expected. In particular for small energy value, the fraction of electron expected in the sample is important. To estimate the residual electron contamination in the pion samples two samples of particles were considered:

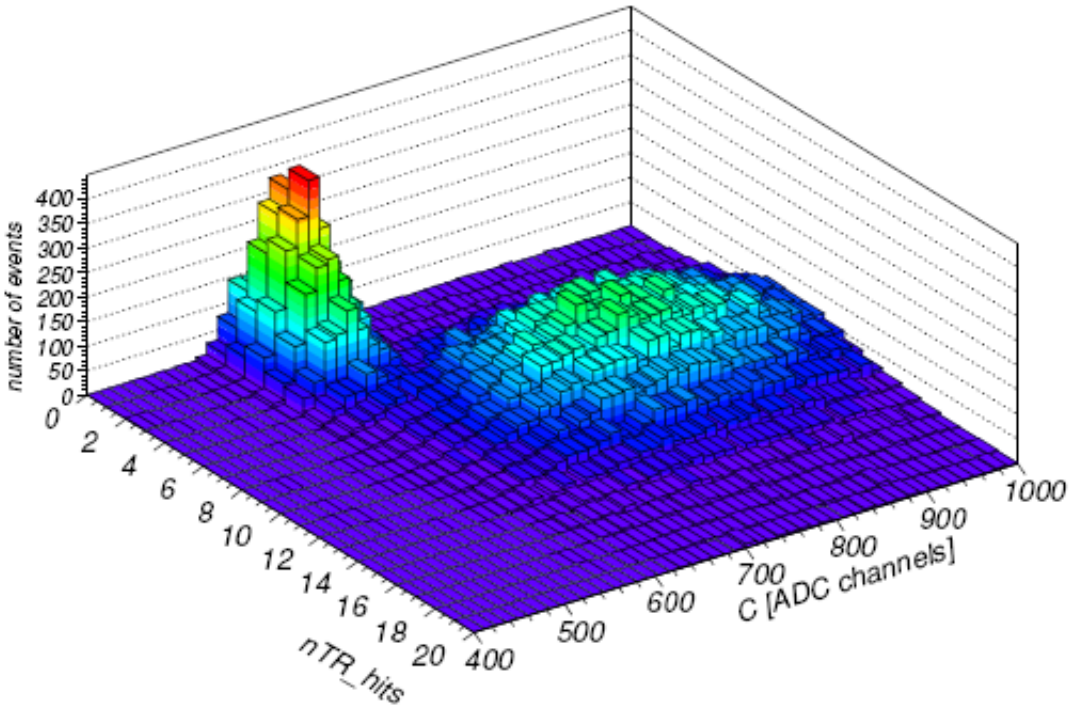


Figure 6.7: Plot of the signal measured in the Cerenkov counter (C) and the number of hits per track produced by transition radiation reconstructed in the TRT (nTR hits).

E_{nom} [GeV]	3	5	7	9
Beam trigger events	93961	94771	94158	94446
cut 1: only one track with more than 30 hits in TRT	61608	61833	61073	63053
cut 2: a hit in at least one of the two projections of each BC	17710	30966	38063	45636
cut 3: no out-of-time cells in TileCal	16823	27352	33639	40374
cut 4: $E_{TileCal3}$ <160 MeV	16214	26109	32441	39123
cut 5: nTR_hits<3	955	1217	2230	3104
cut 6: C<600 ADC channels	141	395	1218	1803

Table 6.1: Events passing different cuts for a beam at η=0.35, ϕ=0 and energies between 3 and 9 GeV.

1. The first sample where only the cuts 1 to 5 are applied (cut 6 on the Cerenkov counter is not applied). This sample corresponds to pions with significant electron contamination.

2. The second sample were the cuts 1 to 4 are applied together with the condition nTR_hits>8. This sample corresponds to a pure electron sample (pions do not give such a high number of HT hits per track).

Figure 6.8 shows the distributions of the signal C in the Cerenkov counter for the two samples 1 and 2. The two distributions are normalized in the region C>800 ADC where only electrons give a signal. The shapes are in good agreement in this region. The electron contamination corresponds to the normalized number of events of Sample 2 lying in the region C<600 ADC. The fractional electron contamination, fe, can be obtained using the formula :

$$f_e = \frac{N_{sample1}(C > 800ADC)}{N_{sample2}(C > 800ADC)} \times \frac{N_{sample2}(C < 600ADC)}{N_{sample1}(C < 600ADC)} \qquad (6.1)$$

where $N_{sample1}$ and $N_{sample2}$ are the number of events for each sample below or above the threshold in C as defined in the brackets. The values of f_e obtained for different nominal beam energies and different values in pseudorapidities are reported in Table 6.2. The uncertainties in f_e are given doing the quadratic sum of the statistical and the systematic errors. The systematic uncertainty was studied by varying the cuts used in equation 6.1 to normalize sample 1 and 2 (from C=700 to 900 ADC), and varying the TRT cut used to select Sample 2 (nTRT hits from 7 to 9). The systematic uncertainty is defined as half of the maximum difference between the values of f_e.

6.3.2 Contamination due to pion decay

The muons coming from the high energy line are not the only affecting the pureness of our pion sample. In fact there are also muons coming from the decay of low energy pions, but it is important to notice that the amount is negligible for energy larger than 3 GeV.

They are originated in the process $\pi^{\pm} \rightarrow \mu^{\pm} + \nu$ at any location before the calorimeters along the beam line.

We distinguish between two categories of low-energy muons:

1. muons coming from pion decays prior to the momentum selection. These muons have an energy equal to the beam energy E_{beam},

2. muons from pion decay after the momentum selection. These muons are produced with an energy uniformly distributed between $E_{max} = E_{beam}$ and $E_{mim} = 0.6E_{beam}$[1].

[1]The energy distribution of the muons reaching the calorimeters is not uniform and depends on the trigger acceptance (size of trigger scintillation counters).

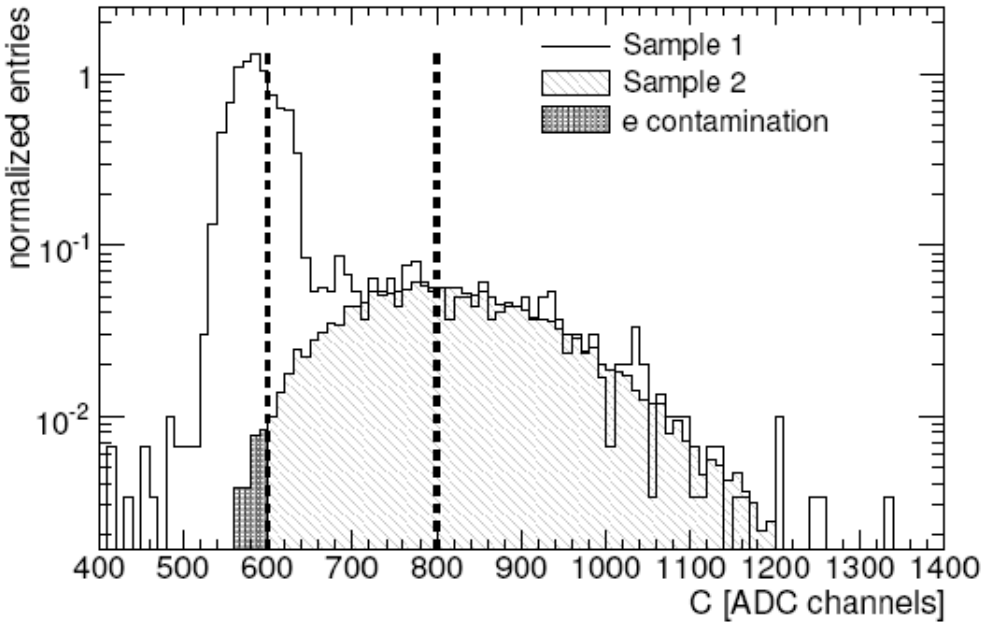


Figure 6.8: Distributions of the Cerenkov signal C for sample 1 (pions and electrons) and sample 2 (only electrons) in the case of a 9 GeV beam. The Cerenkov cuts C=600 ADC (pion selection cut) and C=800 ADC (electron selection cut) are indicated by the dashed lines. The dark region corresponds to the extrapolated electron contamination in the pion sample.

The residual muon contamination in the pion sample was estimated by computing the fraction of muons (of category 1 and 2) which trigger the DAQ system and then compute how many of them pass all the analysis selection cuts.

The fraction of muons which trigger the DAQ was estimated in two different ways:

1. For muons of category 1, it was determined using the results of the analysis of the 2003 test beam period at 3, 5 and 9 GeV [42]. The beam geometry and composition were similar to the one discussed here, while the experimental layout was a rather simplified version of the one used for this analysis.

2. For muons of category 2, a Monte Carlo study was realized simulating the transport and the decay of the particles along the beam line..

The results of these two estimates are shown in figure6.9. The points in the plots represent category 1 muons while the line represents category 2 muons. They show good agreement at 5 and 9 GeV but not at 3 GeV. For each beam energy the muon contamination was taken as the average of the two estimates

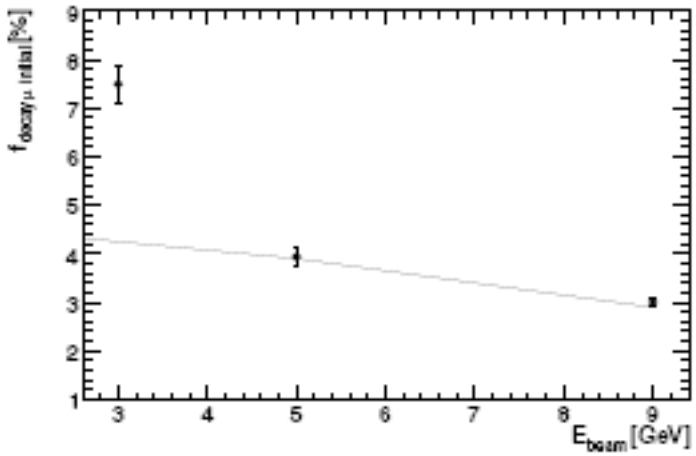


Figure 6.9: Fraction of the decay muons in the pion sample at the front of the calorimeter as a function of the beam momentum. The fraction $f_{decay\mu initial}$ is defined as the number of muons triggering the DAQ divided by the number of pions. The full points show the result of the data-based analysis (method 1 in the text) and the solid curve represents the results obtained by the simulation (method 2 in the text).

and the uncertainty was taken to be half of the difference between the two estimates. A Monte Carlo simulation was used to compute what fraction of muons passes all of the analysis cuts ($f_{decay\mu}$). The fraction is negligible (lower than 1%) for all energies above 3 GeV. Table 6.2 shows the average fraction of contaminating muons. The quantity $f_{decay\mu}$ increases with the pseudo-rapidity as the depth of the calorimeters increases and is negligible (lower than 1%) for $\eta_{beam} < 0.35$.

6.3.3 Contamination by halo muon.

Halo muons coming from the secondary beam line are not stopped in the beam dump and they have a wide energy spectrum; the maximum value can reach the value of the secondary beam energy. They are rejected by the *cut #3* and *cut #4* as shown in Table 6.1. The efficiency of these cuts has been measured using reference samples of 20 GeV muons, taken in the same test beam campaign. As shown in figure 6.6, no high-energy muons are expected to deposit less than 160 MeV in the last TileCal layer (at η=0). The upper limit on the fraction of halo muons that enters in the pion sample is 1% at 3 GeV and 0.2% at 9 GeV (at 95% confidence level).

Electron contamination						
$E_{Nom.}$	η=0.20	η=0.25	η=0.35	η=0.45	η=0.55	η=0.65
3 GeV	9±1	10±2	8±1	8±2	11±2	8±1
4 GeV	3.6±0.4	-	8±1	4.1±0.4	4.3±0.5	3.4±0.4
5 GeV	2.2±0.2	-	2.4±0.2	2.1±0.1	2.3±0.2	-
6 GeV	1.05±0.09	1.2±0.1	0.95±0.09	1.1±0.1	1.08±0.09	1.2±0.1
7 GeV	0.71± 0.06	-	0.63±0.06	0.8±0.1	0.65±0.06	0.64±0.06
8 GeV	0.65±0.05	0.53±0.04	0.68±0.06	0.69±0.06	0.56±0.05	-
9 GeV	-	0.38±0.03	0.45±0.04	0.49±0.06	0.36±0.03	0.38±0.04
Low-energy muons contamination						
$E_{Nom.}$	η=0.20	η=0.25	η=0.35	η=0.45	η=0.55	η=0.65
3 GeV	-	-	1.8±0.5	2.1±0.6	3.0±0.8	3.4±0.9

Table 6.2: Estimated electron contamination and muon contamination in %.

6.4 Pion reconstruction and their response in the calorimeters

In this section we discuss how the reconstructed energy is computed and the response of the calorimeters to charged pions.

6.4.1 Calorimeters energy scale

The cell energy in LAr was reconstructed by the Optimal Filtering coefficients Method[43]. The LAr electromagnetic energy scale was determined comparing the measured and simulated energy response of 180 GeV electrons. The uncertainty on that scale, due mainly to uncertainty in the knowledge of the beam momentum [45], is 0.7%.

In TileCal, the Fit Filter Method, see section 3.4.2, was used to determine the cell energy. The electromagnetic scale of the reconstructed cell energy was obtained using electron beams incident at the center of each cell with an angle of 20°, as explained in section 3.5.4. The estimated error on the energy scale is 0.5%.

The shower energy in the calorimeter was obtained as:

$$E_{raw} = E_{raw}(LAr) + E_{raw}(Tilecal) \tag{6.2}$$

The quantities E_{raw}(LAr) and E_{raw}(TileCal) are respectively the sum of the energy deposited in the front, middle and back samples of LAr, and the sum of the energy deposited in the first and second sample of TileCal. Because the energy deposited in the LAr pre-shower is very small and the noise to signal ratio is large, the pre-shower was not considered in the calculation of E_{raw}. The energy measured in each of the two calorimeters is defined as the sum of the energy deposited in all calorimeter cells energy having a pseudo-rapidity coordinate $\eta_{beam} - 0.15 < \eta < \eta_{beam} + 0.15$ and ± 0.2 in ϕ ($\phi_{beam} = 0$).

No corrections for dead material, containment and non compensation effects were applied. In order to improve the energy resolution, only cells with an energy E_{cell} larger than twice the standard deviation (see equation 6.3) of the electronic noise were considered to calculate Eraw.

$$|E_{cell}| < 2\sigma_{noise} \tag{6.3}$$

6.4.2 Electronic noise and pedestal uncertainty

The electronic noise distributions vary from cell to cell, with large variations between different longitudinal layers. For each run, noise has been determined for each cell of the calorimeter using pedestal events, obtained from random triggers injected between beam bursts. Typical values of the standard deviations are:

- 12 MeV (1st layer of LAr),
- 28 MeV (2nd layer of LAr),
- 22 MeV (3rd layer of LAr),
- 30 MeV (1st layer of TileCal),
- 30 MeV (2nd layer of TileCal),
- 25 MeV (3rd layer of TileCal).

The typical number of cells considered in the computation of the energy in the calorimeters is of the order of 40. The total expected standard deviation of the electronic noise is 160 MeV. This value is negligible with respect to the energies reconstructed in the calorimeter and has a negligible effect on the pion energy resolution.

Another quantity to study with care is the pedestal of the calorimeter cells. In fact because of the small energy delivered and the large number of cells taken into account in the equation 6.2, any small variation from zero in the pedestal signal could affect significantly the energy reconstructed value. In the case of LAr, special runs were taken during the data taking. For each cell and electronic gain setting, pedestals were recorded for each of the 7 time windows used to sample the cell pulse. The mean pedestal in a cell was obtained as the average of the seven measurements. Corrections were also applied to take into account the drift due to changes of the temperature of the electronics front-end boards during the data-taking. The typical size of these corrections on the reconstructed energies was about 10 MeV [43].

In the case of TileCal the method applied to reconstruct the cell energy uses an event-by-event baseline subtraction and therefore corrects for any pedestal shifts. The residual effect of a pedestal shift, called E_{res}, on the reconstructed energy was estimated for each run using the following relation:

$$< E_{res} >=< E_{ped} > \frac{< n_{cell} >}{N_{cell}} \tag{6.4}$$

where $< E_{ped} >$ is the residual pedestal value in the reconstruction volume, and N_{cell} is the total number of the cells in this region. The quantity $< n_{cell} >$ is the average number of cells that satisfy the noise cut condition given by equation 6.3. The absolute value of the pedestal shift was found to be smaller than 2 MeV. This effect is negligible in comparison to the typical reconstructed pion energies.

6.4.3 Measurement of the beam energy

The precise measurement of the energy response ratio $R_{E\pi} = E_\pi/E_{beam}$ requires a good knowledge of the beam energy. The VLE beam momentum can be computed using the equation:

$$p^{VLE}(GeV) = \frac{299.79}{\Theta(mrad)} \int Bdl[Tm] \tag{6.5}$$

where the quantity $\int Bdl$ is the measured magnetic field integral of the bending magnet B4 and Θ is the deflection angle. The angle Θ is the average deflection angle computed for each event using the coordinate measurements of the beam impact point on the beam chambers BC-2, BC-1 and BC0. [36].

Systematic uncertainties on p^{VLE} are due to an incomplete knowledge of the beam line geometry and of the magnetic field integral. The response of the LAr calorimeter to electrons for each beam energy has been used to compute a correction factor S. The beam energy becomes:

$$E_{beam} = S \times p^{VLE} \tag{6.6}$$

In the equation 6.6 the pion mass was neglected. The correction factor S was found to be 0.972±0.008 for all of the nominal beam energies. Table 6.3 shows the measured values of Ebeam. The errors are due to the statistical uncertainty on p^{VLE} and the systematic uncertainty on S. The intrinsic beam energy dispersion is equal to 3.5%. [44] It is negligible compared to the resolution of the calorimeters to pions and therefore neglected.

6.4.4 Pion reconstructed energy

The pion response has been measured for pion samples of various energies and pseudo-rapidity values. Figure 6.10 shows the energy deposit E_{raw} in the ATLAS calorimeter system for a pion beam impinging on the calorimeter at η=0.35 for the four pion energies 3, 5, 7 and 9 GeV. The points represent the experimental data.

The pion response $E_\pi$and the resolution σ_π of the calorimeter measurement are defined from the following function:

Nominal beam energy [GeV]	E_{beam} [GeV]
3	$3.09 \pm 0.02 \pm 0.03$
4	$4.06 \pm 0.01 \pm 0.03$
5	$5.03 \pm 0.02 \pm 0.04$
6	$6.07 \pm 0.02 \pm 0.05$
7	$6.95 \pm 0.01 \pm 0.06$
8	$8.20 \pm 0.01 \pm 0.07$
9	$9.27 \pm 0.01 \pm 0.08$

Table 6.3: Measured values of the beam energies. The first error is due to the statistical uncertainty of the determination of pV LE. The second error is the systematic uncertainty on S.

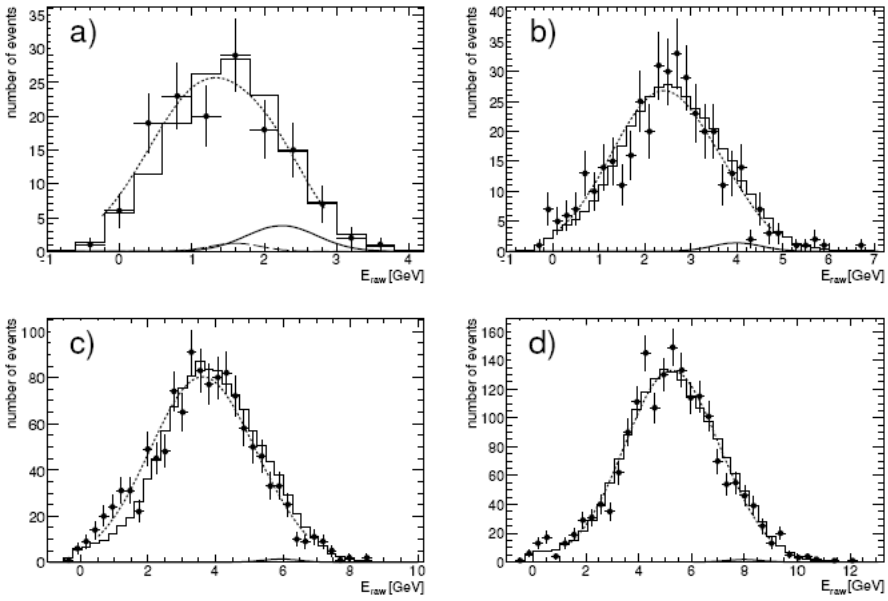


Figure 6.10: Distribution of the reconstructed energy E_{raw} obtained for 3 GeV (a), 5 GeV (b), 7 GeV(c) and 9 GeV(d) at beam=0.35. The full points represent the experimental data. The dashed curves correspond to the fit of equation 6.7 to the data. The solid curve represents the expected contribution of the electron contamination. At 3 GeV, the long-dashed curve shows the expected contribution from the decay muons. The histograms correspond to the prediction of the Monte Carlo simulation.

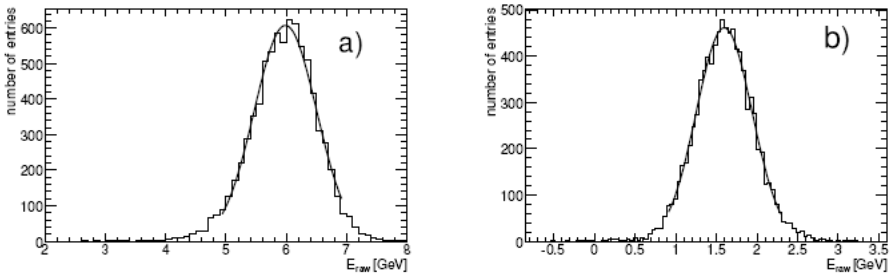


Figure 6.11: a) : E_{raw} distribution for a sample of 7 GeV electron at beam η=0.35. The curve corresponds to a Gaussian fit performed to determine E_e and σ_e. b) : Monte Carlo distribution for a sample of 1.8 GeV muons produced in the decays of beam pions at η=0.35.

$$f(E_{raw}) = N\left[\frac{1-f_e-f_{\mu decay}}{\sigma_\pi\sqrt{2\pi}}e^{\frac{(E_\pi-E_{raw})^2}{2\sigma_\pi^2}} + \frac{f_e}{\sigma_e\sqrt{2\pi}}e^{\frac{(E_e-E_{raw})^2}{2\sigma_e^2}} + \frac{f_\mu}{\sigma_\mu\sqrt{2\pi}}e^{\frac{(E_\mu-E_{raw})^2}{2\sigma_\mu^2}}\right] \tag{6.7}$$

Where $f(E_{raw})$ is the function that reproduce the calorimeter response to particle sample and E_{raw} is the shower energy in the calorimeter defined in equation 6.2. Equation 6.7 has three free parameters, $E_\pi$that is the energy of the pion in the sample, $\sigma_\pi$and the normalization factor N, determined by fitting to the data. The quantity f_e is the measured fraction of electrons in the pion samples, the numerical values are reported in table 6.2. The parameters E_e and σ_e are determined independently and they correspond to the mean and sigma values obtained by fitting a Gaussian to the distribution of E_{raw} for pure electron samples. Such electron samples were obtained applying the selection cuts 1 to 4 (see Table 6.1) requiring C>800 ADC channels and nTR hits>8. Figure 6.11a) shows an example of the E_{raw} distribution obtained in the case of a 7 GeV electron sample at beam η=0.35. The Gaussian fit is performed in a region $\pm 2\sigma$ around the mean value.

The estimated fraction f_μ decay of low-energy muons in the pion sample is significant only for the 3 GeV pion sample at beam η =0.35. The contribution of the low-energy muons is modeled as a Gaussian function with mean value Eμ and σμ width . Eμ and σμ are obtained from the simulated response to a sample of 1.8 GeV[2]. An example of the energy distribution for 1.8 GeV decay muons is given on figure 6.11b). The Gaussian fit is performed in a region $\pm 2\sigma$ around the mean value.

The distributions of E_{raw} are fitted by the function 6.7 in a region $\pm 2\sigma$ around the mean value. The Maximum Likelihood method was used in the fits because of the small statistics of the pion samples. Figure 6.10 shows the typical

[2]1.8 GeV is the most probable energy released by decay muons that do not reach the third sample of TileCal.

distribution of the total reconstructed energy E_{raw} obtained for pion samples of 3, 5, 7 and 9 GeV (at beam η=0.35). The fit function 6.7 is superimposed on the data distributions of figure 6.10. The results of the fit procedure for E_π and σ_π are reported in Table 6.4.

Three sources of systematic uncertainty were considered :

1. uncertainty on the electron (f_e) and decay muon ($f_{\mu decay}$) contamination,
2. uncertainty on the LAr and TileCal energy scales,
3. non-uniformity in η and ϕ of the LAr and TileCal energy response.

The systematic error due to the uncertainty of the electron contamination f_e is estimated by replacing f_e with values $\pm 1\sigma$ from the central value, and repeating the fit of equation 6.7 to the data. ΔE_π and $\Delta\sigma_\pi$ are defined as half of the maximum difference of the fit results. The systematic effect on the reconstructed pion energy E_π is about 1% at 3 GeV, 0.7% at 4 GeV, and smaller at larger energies. The systematic uncertainty on $\sigma_\pi$is 1% at 3 GeV and 4 GeV, and smaller for energies larger than 4 GeV.

The same procedure was applied to compute the systematic errors due to the uncertainty on the decay muon contamination. The relative systematic errors on E_μ and σ_μ are 0.3% and 0.5% respectively.

The uncertainty on the LAr energy scale, due mainly to uncertainty in the knowledge of the beam momentum, is 0.7% [44].The estimated error on the TileCal energy scale is 0.5% [45].

The systematic error due to the non-uniformity of the LAr and TileCal response was studied using electrons and pions beams. The numerical values obtained are 0.4% in the case of LAr [43] and 2% in the case of TileCal [45].

The statistical and systematic errors on E_π and σ_π have been reported in Table 6.4. The first error on E_π corresponds to the statistical uncertainty combined in quadrature with the systematic errors. The second error is due to the uncertainty of the energy scales. In this case the error values of the different data points are correlated. The LAr contribution dominates: it is equal to 7 MeV at 3 GeV and increases up to 25 MeV at 9 GeV. The third error comes from the uncertainty on the calorimeter uniformity response. The TileCal contribution dominates: it is equal to 7 MeV at 3 GeV and increases up to 45 MeV at 9 GeV. In the case of σ_π only the statistical uncertainty, which is much larger than all of the systematic effects, has been reported.

6.4.5 Measurement of the energy response ratio and of the fractional resolution

The measurement of the energy response ratio $R_{E_\pi}=E_\pi/E_{beam}$, and of the fractional resolutions $R_{\sigma_\pi} = \sigma_\pi/E_\pi$ are reported in tables 6.5 and 6.6 respectively. The values of $R_{E_\pi}$are 40% at 3 GeV and 56% at 9 GeV. The first error in the energy response ratio, ΔR_{E_π}, is equal to the quadratic sum of the error on E_π and the error on p^{VLE}. It varies between 8% at 3 GeV and 1% at 9

E_{nom} $[GeV]$	η_{beam}	E_π $[GeV]$	ΔE_π (1) $[GeV]$	ΔE_π (2) $[GeV]$	ΔE_π (3) $[GeV]$	σ_π $[GeV]$
3	0.20	1.38	0.07	0.008	0.007	0.65 ± 0.07
3	0.25	1.2	0.1	0.007	0.007	0.8 ± 0.1
3	0.35	1.25	0.09	0.007	0.007	0.83 ± 0.09
3	0.45	1.3	0.1	0.007	0.006	0.8 ± 0.1
3	0.55	1.0	0.1	0.006	0.005	0.8 ± 0.1
3	0.65	1.11	0.08	0.006	0.005	0.63 ± 0.07
4	0.20	1.83	0.09	0.009	0.01	1.10 ± 0.09
4	0.35	1.7	0.1	0.010	0.009	0.8 ± 0.1
4	0.45	1.78	0.08	0.009	0.01	1.05 ± 0.08
4	0.55	1.84	0.09	0.009	0.01	1.2 ± 0.1
4	0.65	1.70	0.07	0.010	0.008	1.03 ± 0.08
5	0.20	2.34	0.06	0.01	0.02	1.09 ± 0.06
5	0.35	2.42	0.07	0.01	0.02	1.12 ± 0.06
5	0.45	2.45	0.05	0.01	0.02	1.14 ± 0.04
5	0.55	2.28	0.07	0.01	0.01	1.16 ± 0.07
6	0.20	3.02	0.06	0.01	0.02	1.34 ± 0.06
6	0.25	3.15	0.06	0.02	0.02	1.35 ± 0.06
6	0.35	2.96	0.05	0.02	0.02	1.27 ± 0.05
6	0.45	2.95	0.05	0.02	0.02	1.28 ± 0.05
6	0.55	2.96	0.06	0.02	0.02	1.45 ± 0.06
6	0.65	2.83	0.05	0.02	0.02	1.28 ± 0.05
7	0.20	3.78	0.05	0.02	0.03	1.54 ± 0.05
7	0.35	3.64	0.05	0.02	0.03	1.56 ± 0.05
7	0.45	3.62	0.07	0.02	0.03	1.46 ± 0.07
7	0.55	3.67	0.05	0.02	0.03	1.41 ± 0.04
7	0.65	3.59	0.05	0.02	0.02	1.50 ± 0.05
8	0.20	4.26	0.05	0.02	0.03	1.68 ± 0.05
8	0.25	4.49	0.05	0.02	0.04	1.67 ± 0.05
8	0.35	4.40	0.05	0.02	0.03	1.68 ± 0.05
8	0.45	4.43	0.05	0.02	0.03	1.57 ± 0.04
8	0.55	4.36	0.05	0.02	0.03	1.71 ± 0.05
9	0.25	5.30	0.06	0.02	0.05	1.91 ± 0.06
9	0.35	5.26	0.05	0.02	0.04	1.79 ± 0.04
9	0.45	5.23	0.07	0.03	0.04	1.88 ± 0.07
9	0.55	5.06	0.05	0.03	0.04	1.88 ± 0.05
9	0.65	4.91	0.07	0.03	0.03	2.00 ± 0.06

Table 6.4: Measured energy response E_π and the resolution σ_π. The first error on E_π corresponds to the quadratic combination of the statistical error and the error due to the uncertainty on the contamination of electrons and muons (1). The second error on E_π is the systematic uncertainty on the energy scale (2) definition in LAr and TileCal (see text) and the third one corresponds to the non-uniformity of the energy scale in η and ϕ. The errors on σ_π are dominated by the statistical ones.

GeV. The second error, ΔR_{E_π}, affects in the same way all the measurements of E_π/E_{beam}. It was obtained combining the uncertainties due to the calorimeter scale factors and S, where S is the correction factor used in equation 6.6 to calculate E_{beam}. The beam energy correction factor terms dominate. The third error, ΔR_{E_π}, is due to the non-homogeneity of the calorimeters response. Below 6 GeV the LAr and TileCal contributions are comparable. Above 6 GeV, TileCal contribution dominates. The values of R_{σ_π} are 56% at 3 GeV and 34% at 9 GeV. The contribution of the electronic noise to the resolution is 15% at 3 GeV and decreases to 4% at 9 GeV. The largest uncertainty in the resolution is the statistical error.

The quantities R_{E_π} are shown in figure 6.12 (open circles) as a function of η_{beam} for different beam energies. They are also shown in figure 6.13 as a function of E_{beam} for different beam values. In the two figures the errors include statistical and systematic effects combined in quadrature. Figure 6.14 shows the fractional resolutions R_{σ_π}as a function of $1/\sqrt{E_{beam}}$ (open circles) for different beam values.

6.4.6 Montecarlo comparison

The experimental results were compared to the predictions of the Monte Carlo (MC) simulation program Geant 4[3] at the electromagnetic energy scale. For the MC the LAr and TileCal scales were obtained using the results from electron simulations (see section 6.4.1). The QGSP-Bertini hadronic showering package was used in the simulation. This package is presently being used in the simulation of the response of the ATLAS detector to p-p events at 14 TeV.

In the simulation the detector material and geometry were fully described [46, 47]. The mean and spread of the incoming pion beam momentum correspond to what was measured. The spatial and angular distributions of the beam were also tuned to reproduce the experimental ones. The measured electronic noise in the different calorimeter cells and the effects of photo statistics (70 phe/GeV) are included in the Monte Carlo simulation. A total of 10^{54} events were simulated for each experimental point (η and energy).

The distribution of the variable E_{raw} obtained with simulated data is shown in figure 6.10 for beam energies 3, 5, 7 and 9 GeV, and η_{beam}=0.35. The simulated data reproduce well the experimental data at all the energies analyzed. The agreement is good also at 3 GeV where the contamination coming from pions and electrons is more important

The distributions obtained with the Monte Carlo simulation were fitted with a Gaussian response function to determine E_π and σ_π. Results are reported in tables 6.5 and 6.6. Figures 6.12, 6.13 and 5.19 show the Monte Carlo results (full points) together with data (open points).

[3]The version 9.1 was used.

[4]To reproduce the experimental situation, contamination from electrons and decay muons (in the case of the 3 GeV beam) has been added to the simulated pion sample. This contamination corresponds to what is reported in Table 6.2.

E_{nom} [GeV	η_{beam}	R_{E_π}	ΔR_{E_π} (1)	ΔR_{E_π} (2)	ΔR_{E_π} (3)	$(R_{E_\pi})_{MC}$
3	0.20	0.45	0.02	0.002	0.002	0.432 ± 0.001
3	0.25	0.40	0.03	0.002	0.002	0.456 ± 0.001
3	0.35	0.41	0.03	0.002	0.002	0.447 ± 0.001
3	0.45	0.42	0.04	0.002	0.002	0.454 ± 0.001
3	0.55	0.33	0.04	0.002	0.002	0.445 ± 0.001
3	0.65	0.36	0.02	0.002	0.002	0.443 ± 0.001
4	0.20	0.45	0.02	0.003	0.003	0.466 ± 0.001
4	0.35	0.43	0.03	0.002	0.002	0.491 ± 0.001
4	0.45	0.44	0.02	0.002	0.003	0.489 ± 0.001
4	0.55	0.45	0.02	0.003	0.003	0.479 ± 0.002
4	0.65	0.42	0.02	0.002	0.002	0.474 ± 0.001
5	0.20	0.47	0.01	0.003	0.003	0.494 ± 0.001
5	0.35	0.48	0.01	0.003	0.003	0.517 ± 0.001
5	0.45	0.487	0.009	0.003	0.003	0.516 ± 0.001
5	0.55	0.45	0.01	0.003	0.003	0.510 ± 0.001
6	0.20	0.498	0.009	0.003	0.004	0.512 ± 0.001
6	0.25	0.52	0.01	0.003	0.004	0.542 ± 0.001
6	0.35	0.487	0.008	0.003	0.003	0.540 ± 0.001
6	0.45	0.485	0.008	0.003	0.003	0.540 ± 0.001
6	0.55	0.49	0.01	0.003	0.003	0.533 ± 0.001
6	0.65	0.465	0.009	0.003	0.003	0.529 ± 0.001
7	0.20	0.543	0.008	0.003	0.005	0.526 ± 0.001
7	0.35	0.523	0.008	0.003	0.004	0.557 ± 0.001
7	0.45	0.52	0.01	0.003	0.003	0.557 ± 0.001
7	0.55	0.527	0.007	0.003	0.004	0.549 ± 0.001
7	0.65	0.517	0.007	0.003	0.003	0.544 ± 0.001
8	0.20	0.520	0.007	0.003	0.004	0.542 ± 0.001
8	0.25	0.548	0.006	0.003	0.005	0.578 ± 0.001
8	0.35	0.537	0.007	0.003	0.004	0.573 ± 0.001
8	0.45	0.541	0.006	0.003	0.004	0.573 ± 0.001
8	0.55	0.532	0.007	0.003	0.004	0.563 ± 0.001
9	0.25	0.572	0.006	0.004	0.005	0.586 ± 0.001
9	0.35	0.568	0.005	0.003	0.005	0.583 ± 0.001
9	0.45	0.564	0.008	0.003	0.004	0.581 ± 0.001
9	0.55	0.546	0.006	0.003	0.004	0.574 ± 0.001
9	0.65	0.529	0.007	0.003	0.003	0.570 ± 0.001

Table 6.5: Energy response ratio measurements for pions of different energy and η_{beam}. See section 6.4.4 for details about the error determination. In the table the results obtained using a Monte Carlo (MC) simulation are also reported (see section 6.4.5).

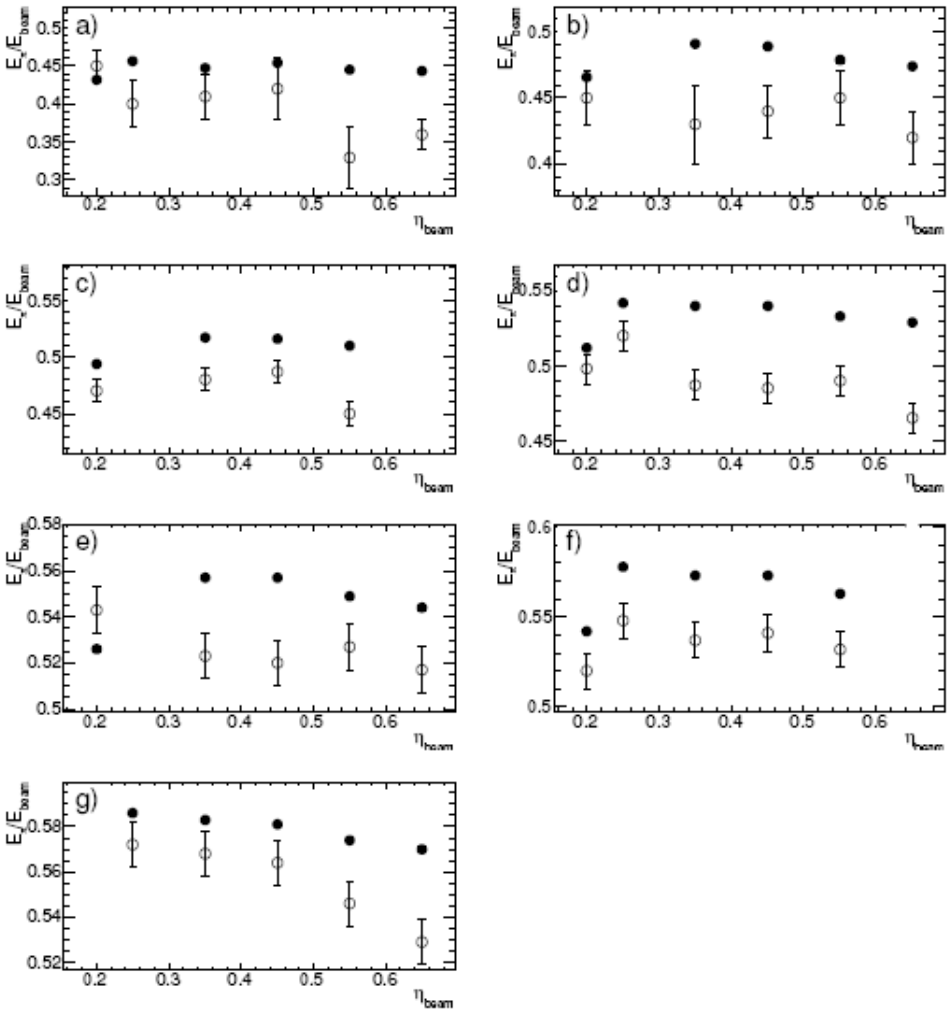


Figure 6.12: Energy response ratios measured (open points) and predicted by Monte Carlo simulation (full points) as a function of η_{beam} for different beam energy values: a) 3 GeV, b) 4 GeV, c) 5 GeV, d) 6 GeV, e) 7 GeV, f) 8 GeV and g) 9 GeV. The error includes statistical and systematic effects combined in quadrature.

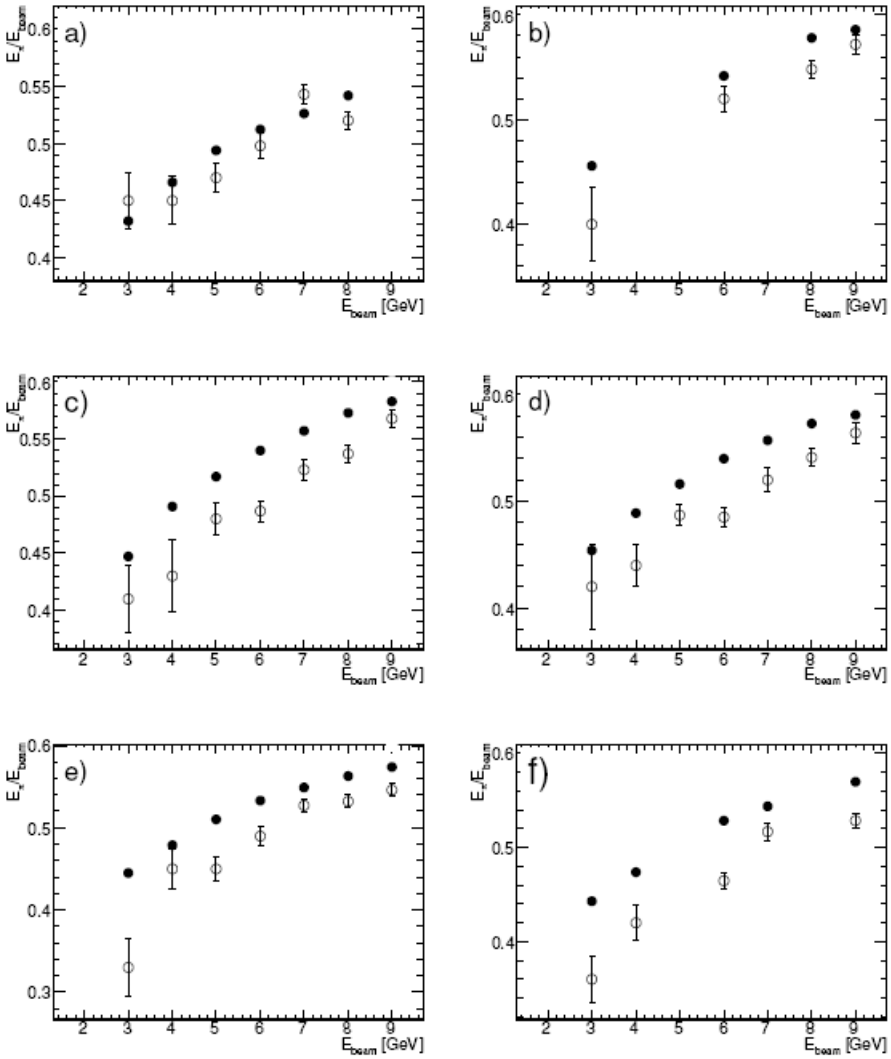


Figure 6.13: Energy response ratio measured (open points) and predicted by Monte Carlo simulation (full points) as a function of E_{beam} for different η_{beam} values: a) 0.20, b) 0.25, c) 0.35, d) 0.45, e) 0.55, and f) 0.65. The error includes statistical and systematic effects combined in quadrature.

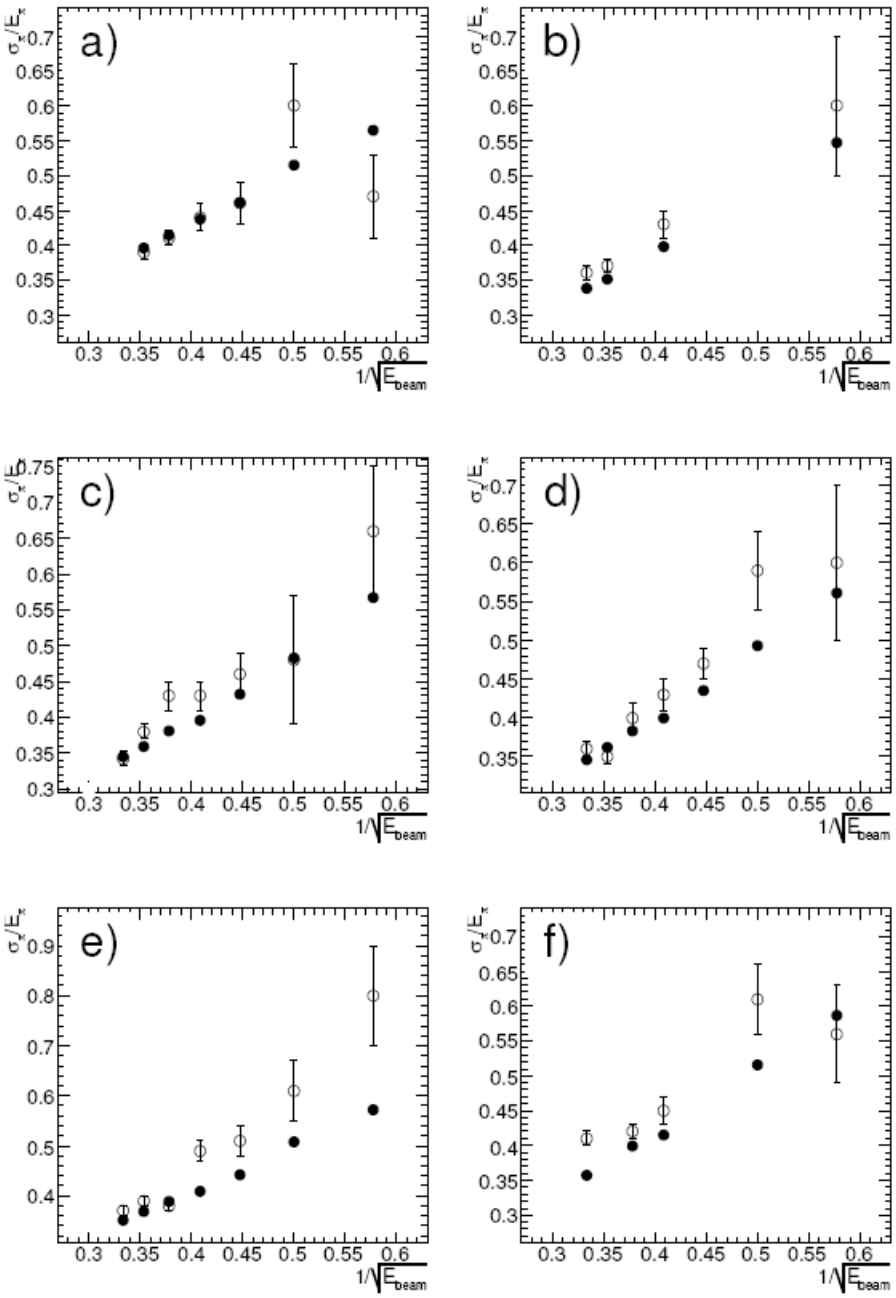


Figure 6.14: Fractional resolutions measured (open circles) and predicted by the Monte Carlo simulation (full points) as a function of $1/\sqrt{E_{beam}}$ for different values of beam : a) 0.20, b) 0.25, c) 0.35, d) 0.45, e) 0.55, and f) 0.65. The errors include statistical and systematic effects.

E_{nom} [GeV]	η_{beam}	R_{σ_π}	$(R_{\sigma_\pi})_{MC}$
3	0.20	0.470 ± 0.060	0.565 ± 0.003
3	0.25	0.600 ± 0.100	0.547 ± 0.003
3	0.35	0.660 ± 0.090	0.567 ± 0.003
3	0.45	0.600 ± 0.100	0.561 ± 0.003
3	0.55	0.800 ± 0.100	0.572 ± 0.003
3	0.65	0.560 ± 0.070	0.587 ± 0.003
4	0.20	0.600 ± 0.060	0.515 ± 0.003
4	0.35	0.480 ± 0.090	0.483 ± 0.002
4	0.45	0.590 ± 0.050	0.493 ± 0.002
4	0.55	0.610 ± 0.060	0.508 ± 0.004
4	0.65	0.610 ± 0.050	0.516 ± 0.003
5	0.20	0.460 ± 0.030	0.461 ± 0.002
5	0.35	0.460 ± 0.030	0.432 ± 0.002
5	0.45	0.470 ± 0.020	0.435 ± 0.002
5	0.55	0.510 ± 0.030	0.442 ± 0.002
6	0.20	0.440 ± 0.020	0.437 ± 0.002
6	0.25	0.430 ± 0.020	0.398 ± 0.002
6	0.35	0.430 ± 0.020	0.396 ± 0.002
6	0.45	0.430 ± 0.020	0.400 ± 0.002
6	0.55	0.490 ± 0.020	0.409 ± 0.002
6	0.65	0.450 ± 0.020	0.415 ± 0.002
7	0.20	0.410 ± 0.010	0.414 ± 0.002
7	0.35	0.430 ± 0.020	0.381 ± 0.002
7	0.45	0.400 ± 0.020	0.383 ± 0.002
7	0.55	0.380 ± 0.010	0.389 ± 0.002
7	0.65	0.420 ± 0.010	0.399 ± 0.002
8	0.20	0.390 ± 0.010	0.396 ± 0.002
8	0.25	0.370 ± 0.010	0.351 ± 0.002
8	0.35	0.380 ± 0.010	0.359 ± 0.002
8	0.45	0.350 ± 0.010	0.362 ± 0.002
8	0.55	0.390 ± 0.010	0.369 ± 0.002
9	0.25	0.360 ± 0.010	0.338 ± 0.002
9	0.35	0.342 ± 0.009	0.345 ± 0.002
9	0.45	0.360 ± 0.010	0.346 ± 0.001
9	0.55	0.370 ± 0.010	0.351 ± 0.002
9	0.65	0.410 ± 0.010	0.357 ± 0.001

Table 6.6: Fractional energy resolution measurements for pions of different energy and η_{beam}. The errors are dominated by the statistical ones. The results obtained using a Monte Carlo (MC) simulation are also reported (see section 6.4.5).

The mean energy response of the simulated data is higher than that obtained with the experimental data and the distributions are narrower. The comparison between the data and the simulation can be quantified using the quantities:

- $\left(\frac{R_{E_\pi MC}}{R_{E_\pi}}\right) - 1$,
- $\left(\frac{R_{\sigma_\pi MC}}{R_{\sigma_\pi}}\right) - 1$

The results are reported in Table 6.7. Statistical and systematic uncertainties were combined in quadrature.

Conclusions The characterization of the response of the ATLAS calorimeters to low-energy particles (below 10 GeV) is an important issue because low energy particles carry a large fraction of the total energy of jets. Many strategies to establish the jet energy scale in ATLAS rely on the Monte Carlo simulation of the electromagnetic and hadronic calorimeters. Test beam data are very important to constrain, test and validate the simulation models. A large amount of low-energy data was taken during the 2004 combined test beam.

$(R_{E_\pi})_{MC}/R_{E_\pi} - 1$ [%]						
E_{nom} [GeV]	η=0.20	η=0.25	η=0.35	η=0.45	η=0.55	η=0.65
3	-4 ± 5	14 ± 10	10 ± 8	9 ± 10	36 ± 15	23 ± 8
4	4 ± 5	-	15 ± 9	11 ± 5	6 ± 5	14 ± 5
5	6 ± 3	-	8 ± 3	6 ± 2	13 ± 4	-
6	3 ± 2	4 ± 2	11 ± 2	11 ± 2	9 ± 2	14 ± 2
7	-3 ± 2	-	7 ± 2	7 ± 2	4 ± 2	5 ± 2
8	4 ± 2	5 ± 2	7 ± 2	6 ± 2	6 ± 2	-
9	-	2 ± 2	3 ± 1	3 ± 2	5 ± 1	8 ± 2
$(R_{\sigma_\pi})_{MC}/R_{\sigma_\pi} - 1$ [%]						
E_{nom} [GeV]	η=0.20	η=0.25	η=0.35	η=0.45	η=0.55	η=0.65
3	20 ± 14	-13 ± 14	-14 ± 11	-6 ± 17	-26 ± 14	5 ± 14
4	-15 ± 8	-	0 ± 18	-16 ± 7	-17 ± 8	-16 ± 7
5	-1 ± 6	-	-6 ± 6	-7 ± 4	-13 ± 6	-
6	-2 ± 4	-7 ± 5	-8 ± 4	-8 ± 4	-16 ± 4	-8 ± 4
7	1 ± 4	-	-12 ± 3	-5 ± 5	1 ± 3	-5 ± 4
8	1 ± 3	-6 ± 3	-6 ± 3	2 ± 3	-6 ± 3	-
9	-	-6 ± 3	1 ± 3	-4 ± 4	-5 ± 3	-13 ± 3

Table 6.7: Relative difference of response (top) and resolution (bottom) between data and simulated events, for different values of the beam energy and pseudo-rapidity. The errors were obtained combining in quadrature the statistical and the systematic uncertainties as discussed in the text.

Pion and electron samples with energies between 3 and 9 GeV and an incident angle corresponding to pseudo-rapidity between 0.2 and 0.65 were recorded. In this chapter, a detailed analysis of the response of the electromagnetic and hadronic central calorimeters to low-energy pions has been presented. Clean pion samples have been obtained after removing various sources of contamination (electrons and muons). The calorimeter response (reconstructed energy and energy resolution) was computed, taking into account the remaining contamination. All energies were reconstructed at the electromagnetic scale and without any correction for dead material and non-compensation of the calorimeters. Considering the statistical uncertainties and some sources of systematic errors (miscalibration of the beam energy, uncertainty on the contamination), the ratio between the reconstructed pion energy and the beam energy has been determined with a precision varying from 1% at 9 GeV to 8% at 3 GeV. The error on the fractional resolution varies from 14% at 3 GeV to about 3% at 9 GeV.

The measurements were compared to simulated results obtained using Geant. The simulation predicts a higher response and a lower energy resolution than the measured ones. The relative ratio of the energy responses, data over simulation, depends on the beam energy and on η_{beam}, and ranges from +0.4% at 9 GeV to +15% at 3 GeV. The relative ratio of the two corresponding resolutions depends also on η_{beam} and E_{beam}; it ranges from -6% at 9 GeV to -15% at 3 GeV. The agreement seems to improve at larger values of E_{nom} and to decrease

with increasing η_{beam} values.

Conclusion

The work presented in this thesis involved two main axis:

1. the calibration of the TileCal phomultipliers with a LASER system,
2. the study of the combined response of the ATLAS calorimeters to pions at 2004 combined test beam.

The TileCal photomultipliers calibration is an important task to achieve in order to monitor the stability and the linearity of the gain. The first step in this work has been the commissioning of the LASER box once installed. This step was necessary to be sure that the components used for LASER system intercalibration didn't introduce systematics in the calibration procedure. The commissioning has demonstrated that the LASER box parameter are under control and that all the tools installed for the system intercalibration are working properly. The second step concerned the set up of procedure to measure the stability and the linearity of the gain. The gain stability of the TileCal PMTs is established after some modification in the LASER system in order to correct some problems in the light transmission. It is measured with a precision of 1%. The work on gain linearity is ongoing and right now we can perform the linearity studies on a great part of Tilecal PMTs dynamic, and we pointed out some modification to apply at the system in order to increase and simplify the measures on that subject. At present we are able to measure the linearity with a precision that varies between 0.08%, at lower energy value, and 3% at high energy value. The measure is realized on the half of the TileCal (100 MeV-400 GeV). Some system weaknesses that affects the precision on the linearity measurements at high energy values have been pointed out and we are working to fix these problems.

The characterization of the response of the ATLAS calorimeters to high and low energy particles is an important issue to establish the jet energy scale. Many strategies to establish that scale in ATLAS rely on the Monte Carlo simulation of the electromagnetic and hadronic calorimeters. Test beam data are very important to constrain, test and validate the simulation models. A large amount of low-energy data was taken during the 2004 combined test beam.

The combined energy reconstruction was realized doing the sum of cell responses calibrated at the electromagnetic scale for LAr and TileCal calorime-

ters. Such a reconstruction allows to compare the data with the simulation. No correction for dead material and non-compensation of the calorimeters have been applied.

The fractional energy response to high energy pions (20-250 GeV) was measured considering the statistical and the systematics errors with a precision of 1% dominated by the uncertainty on beam energy and non uniformity effects in the calorimeters. The fractional energy resolution has been measured with an error of 2% or lower. These measures can be used as reference for the comparison with the simulation. The difference with simulation is about 2% on the fractional reconstructed energy. This difference can be explained by the fact that the longitudinal profile of the shower is systematically longer in the simulation than in the data, but an analysis of the shower development is necessary. For the points at 50 and 100 GeV an additional systematical error coming from the values of proton contamination has been considered. This error equal to 1% at 50 GeV and 0.4% at 100 GeV and is considered in the errors on table 5.7. The simulation can be used now for the study of the calorimeters behavior in the case of jets.

Pion and electron samples with energies between 3 and 9 GeV and an incident angle corresponding to pseudo-rapidity between 0.2 and 0.65 were recorded. A detailed analysis of the response of the electromagnetic and hadronic central calorimeters to low-energy pions has been presented. Clean pion samples have been obtained after removing various sources of contamination (electrons and muons). The calorimeter response (reconstructed energy and energy resolution) was computed, taking into account the remaining contamination. Considering the statistical uncertainties and some sources of systematic errors (miscalibration of the beam energy, uncertainty on the contamination), the ratio between the reconstructed pion energy and the beam energy has been determined with a precision varying from 1% at 9 GeV to 8% at 3 GeV. The error on the fractional resolution varies from 14% at 3 GeV to about 3% at 9 GeV. The measurements were compared to simulated results obtained using Geant. The simulation predicts a higher response and a lower energy resolution than the measured ones. The relative ratio of the energy responses, data over simulation, depends on the beam energy and on beam, and ranges from +0.4% at 9 GeV to +15% at 3 GeV. The relative ratio of the two corresponding resolutions depends also on η_{beam} and E_{beam}; it ranges from -6% at 9 GeV to -15% at 3 GeV. The agreement seems to improve at larger values of E_{nom} and to decrease with increasing η_{beam} values.

Conclusion en français

La validation des différentes composantes du système de calibration interne a été présentée. La stabilité temporelle de toutes les composantes a été testées pour vérifier que leur comportement soit conforme aux valeurs insérées dans le cahier des charges. La stabilité temporelle a été mesurée avec une précision de 0.5% sur 15 jours. Ce résultat est en accord avec la valeur attendue.

Les résultats produits à l'issue de l'analyse ont démontré que le système est très performant mais présente toutefois quelques faiblesses potentielles. Une stratégie pour éliminer ces problèmes a été mise en place de sorte que l'on dispose d'un système opérationnel pour le démarrage de l'accélérateur. Nous sommes capables maintenant de mesurer la stabilité avec une précision de 0.2%. Cette mesure est en accord avec la valeur attendue.

L'analyse des tests de linéarité des PM a mise en évidence des problèmes dans le système de calibration interne du laser. Il y a eu des progrès dans la compréhension de ce problème et la finalisation de cette partie de la calibration est prévue pour les prochains mois.

L'étude de la réponse des calorimètres aux pions des haute et basse énergie a été présentée.

Dans cette analyse, la réponse de l'ensemble calorimètre électromagnétique et calorimètre hadronique à des pions d'énergie connue a été étudiée. Les informations issues de cette analyse sont très utiles pour l'étude et la simulation des gerbes hadroniques. L'objectif est d'obtenir une simulation de la réponse des calorimètres d'ATLAS qui reproduise le mieux possible les résultats obtenus en faisceau test. La simulation pourra ensuite être extrapolée au cas des jets.

Un ensemble des coupures permettant la sélection d'un échantillon de pions aussi pur que possible, en particulier les électrons et les muons présents dans l'échantillon a été établi. Pour cet échantillon, nous avons mesuré différentes grandeurs sensibles aux phénomènes physiques mis en jeu dans la calorimétrie: énergie moyenne, résolution, linéarité de la réponse en énergie. L'analyse a démontré que le comportement du calorimètre hadronique est celui attendu pour un calorimètre non compensé (e/h>1). La précision sur l'énergie reconstruite est de 2% à 20 GeV et 1% à 250 GeV. La précision sur la résolution est 2%.

La comparaison entre simulation et données a démontré une différence de 2% pour l'énergie reconstruite et une différence de l'ordre de 10% pour la résolution.

La même analyse a été faite pour les pions de basse énergie. Aprés avoir

éliminé différentes sources de contamination (électrons et muons) et avoir pris en compte les incertitudes statistiques et systématiques, nous avons mesuré l'énergie reconstruite avec une précision comprise entre 1% (9 GeV) et 8% (3 GeV) et la résolution avec une précision comprise entre 3% (9 GeV) et 14% (3 GeV). Ces résultats on étés comparés avec la simulation. Pour l'énergie reconstruite, on observe une différence de 0.4% à 9 GeV et 15% à 3 GeV. Pour la résolution, la différence est de -6% à 9 GeV et -15% à 3 GeV.

GEANT 4 a été utilisé pour la simulation du détecteur et du matériel présent sur le faisceau test. Pour simuler les gerbes hadroniques nous avons utilisé la liste de physique QGSP Bertini.

Les résultats obtenus démontrent qu'il est possible d' utiliser ces mesures comme référence pour l'ajustement de la simulation.

Appendix A

If we write the measured energy as $E_m = lE + n$ the error on $E_m$comes from E that is the energy of the beam, l that is a linearity factor and n that is noise term.

The expression for the error that we obtain is:

$$\Delta E_m = E \cdot \Delta l \oplus l \cdot \Delta E \oplus \Delta n$$

If we affirm that at the first order $E_m \approx E$ we can write the relative error as:

$$\frac{\Delta E_m}{E_m} = \Delta n l \oplus l \cdot \frac{\Delta E}{E} \oplus \frac{\Delta n}{E}$$

The energy deposited in a calorimeter is proportional to the number N of particles that pass trough the active material, is for that reason that we can write $E \approx E_m \approx N$. The error on N is $\Delta N = \sqrt{N} = \sqrt{E}$.

The former equation is know:

$$\frac{\Delta E_m}{E_m} = l \cdot \frac{\sqrt{E}}{E} \oplus \frac{\Delta n}{E} \oplus \Delta l$$

If we replace l with a, we put $b = \frac{\Delta n}{E}$, $c = \Delta l$ and then we multiply and divide the first term with $\sqrt{E}$we obtain:

$$\frac{\Delta E_m}{E_m} = \frac{a}{\sqrt{E}} \oplus b \oplus \frac{c}{E}$$

That, if we neglect the third term, is the expression of the parametrization 5.12. The first term takes into accout the energy fluctuation and the second one one is a constant term that takes into account the non-linearity.

Bibliography

[1] F.Halzen, A.D. Martin; *Quarks and letpons: an introductory course in modern particle physics.* Wiley 1984.

[2] C.Quigg; *Gauge theories of the Strong, Weak anf Electromagnetic interaction.* The Benjamin/Cummings Publishing Company, London, 1983.

[3] W.M. Yao et al.; *Journal o physics.* G 33, 1, 2006, http://pdg.web.cern.ch/pdg/pdg.html.

[4] P. Higgs; *Phys. Lett.* 12:132, 1964

[5] F. Englert, R. Brout; *Phys. Rev. Lett.* 13:321-23, 1964

[6] ATLAS Coll; *Atlas Detector and Physics Performance: Technical Design Report, Volume I and II.* Report CERN/LHCC/99-14 and 15 (1999)

[7] H.L. Lai et al.; *Improved parton distribution from global analysis of recent deep inelastic scattering and inclusive jet data.* Phys. Rev. D 55 (1997) 1280

[8] *The LHC Conceptual Design Report-The Yellow Book.* CERN/AC/95-05(LHC)

[9] ATLAS Coll.; *ATLAS Detector and Physics Performance:Technical Design Report, Volume I e Volume II.* Report CERN/LHCC/99-14 e 15 (1999).

[10] ATLAS Coll.; *Magnet System Technical Design Report.* Report CERN/LHCC/97-18.

[11] ATLAS Coll.; *Inner Detector Technical Design Report.* Report CERN/LHCC/97-17.

[12] ATLAS Coll.; *Calorimeter Performance Technical Design Report.* Report CERN/LHCC/96-40.

[13] ATLAS Coll.; *Tile Calorimeter Technical Design Report.* Report CERN-LHCC/96-42.

[14] ATLAS Coll.; *Liquid Argon Calorimeter Technical Design Report.* Report CERN-LHCC/96-41.

[15] ATLAS Coll.; *The ATLAS Muon Spectrometer Technical Design Report.* Report CERN-LHCC/97-22.

[16] M. Bosman, S.Bravo, M.Cavalli-Sforza, E.Graugès; *Measurement of the optical properties of the EB Modules Tiles,* ATL-TILECAL-98-157, CERN

[17] P.Grenier, L.P.Says; *Analysis of the 1997 Test Beam Laser Data of the Tilecal extended barrel modules,* ATL-TILECAL-98-159, CERN

[18] Y.A.Kulchitsky, P.V.Tsiareshka, V.B.Vinogradov; *Electron Energy Resolution of the ATLAS TILECAL Modules with Flat Filter method,* ATL-TILECAL-PUB-2005-004, CERN

[19] Y.A.Kulchitsky, P.V.Tsiareshka, V.B.Vinogradov; *Energy Calibration of the TILECAL Modules with the Flat Filter Modules,* ATL-TILECAL-PUB-2005-005, CERN

[20] E.Fullana et al.; *Optimal Filtering in the ATLAS Hadronic Tile Calorimeter,* ATL-TILECAL-2005-001, CERN

[21] R.Teuscher; *ATLAS Tilecal Electronics Calibration.* ATLAS Calibration Workshop, Tatra, Slovakia (2004)

[22] K. Aitamar et al.; *"opticalal fibre connectors for the LASER calibration system".* ATL-TILECAL- 96-093

[23] *https: // twiki. cern. ch/ twiki/ bin/ viewfile/ Atlas/ TileMinBias? rev= 1; filename= SHAFT_ User_ ManualV3. pdf*

[24] Z. Ajaltouni et al.; *"The Tilecal LASER monitoring".* ATL-TILECAL-94-093

[25] M. Anfreville et al. ; *"Laser monitoring system for the CMS lead tungstate crystal calorimeter".* CMS NOTE-2007/028

[26] A.I. Malakov et al. ; *"The laser-based calibration system of delta spectrometer".* Nucl.Instr. and Meth. A566 (2006), 413-421

[27] A. Bamberger et al.; *"Calibration of the ZEUS calorimeter ".* Nucl.Instr. and Meth. A277 (1989), 46-55

[28] *http: // www. newport. com*

[29] *http: // www. hamamatsu. com/*, photodiode reference is S2744-09

[30] *http: // www. lumatec. de/*

[31] B. Di Girolamo, M. Gallas, T. Koffas; *"ATLAS Barrel Combined Run in 2004 Test Beam Setup and its evolution,* ATC-TT-IN-001, CERN

[32] Dainty C (Ed); *Laser Speckle and Related Phenomena*, 1984, Sprinter Verlag,

[33] M. Crouau, G. Montarou, D. Rey; *Technical characteristics of the prototype of the TILECAL photomultipliers test-bench*, ATL-TIL-98-148

[34] The h8 muon community; "*Proposed measurement program for H8 2004 muon system test*". ATL-COM-MUON 2004-006, CERN

[35] T.Sjostrand, S. Mrenna and P. Skands, JHEP 05 (2006) 026.

[36] I.Efthymiopoulos and A.Fabich; *"The very low 1-9 GeV/c tertiary beam extension of the H8 beam line of CERN SPS*". CERN-AB-2005-036.

[37] L.Gatignon; *"XCET: Threshold Cerenkov counters"*. http://ab-div-atbea.web.cern.ch/ab-div-atb-ea/documentation/eqpmts/xcet.html

[38] J.Spanggaard, CERN SL=Note 98-023-BI.

[39] B.Di Girolamo, A.Dotti, V.Giangiobbe, P.Johansson, L.Pribyl, M.Volpi; *"Beamline instrumentation in the 2004 combined ATLAS testbeam"*. ATL-TECHPUB- 2005-001.

[40] ATLAS/Inner detector Collaboration; *"Inner detector Technical Design Report*". Volume I CERN/LHCC 97-16, Volume II CERN/LHCC 97-17.

[41] T.H.Kittelmann, E.B.Klinkby; *"A Study of TRT Noise in 2004 Test Beam Data*". ATL-INDET-PUB-2008-010.

[42] E.Bergeas, S.Hellman, K.Jon-And; *"Very Low Energy Muons in ATLAS TileCal*", ATL-TILECAL-PUB-2005-001.

[43] M.Aleksa et al.; *ATLAS Combined Testbeam : "Computation and Validation of the Electronic Calibration Constants for the Electromagnetic Calorimeter"*. ATL-LARG-PUB-2006-003.

[44] M.Aharrouche et al.; *"Performance of the Liquid Argon Electromagnetic ATLAS Calorimeter measured at 2004 ATLAS Combined Testbeam*". in preparation.

[45] TileCal system of the ATLAS Collaboration; *"Testbeam Studies of Production Modules of the ATLAS Tile Calorimeter"*. submitted to Nucl. Instr. and Meth. for publication.

[46] S.Agostinelli et al., Methods in Physics Research A 506 (2003) 250-303; J. Allison et al. IEE Transactions on Nuclear Science 53 No. 1 (2006) 270-278.

[47] D.Costanzo;" *ATLAS detector simulation:status and outlook*". ATL-SOFTPUB- 2005-004.